

Copyright  
by  
Curtis Patrick Leon Lansdell  
2002

The Dissertation Committee for Curtis Patrick Leon Lansdell  
certifies that this is the approved version of the following dissertation:

**Charged Xi Production in 130 GeV Au+Au Collisions  
at the Relativistic Heavy Ion Collider**

Committee:

---

Gerald W. Hoffmann, Supervisor

---

Takeshi Udagawa

---

Peter J. Riley

---

Robert L. Ray

---

William T. Guy, Jr.

**Charged Xi Production in 130 GeV Au+Au Collisions  
at the Relativistic Heavy Ion Collider**

by

**Curtis Patrick Leon Lansdell, B.S.**

**DISSERTATION**

Presented to the Faculty of the Graduate School of  
The University of Texas at Austin  
in Partial Fulfillment  
of the Requirements  
for the Degree of

**DOCTOR OF PHILOSOPHY**

THE UNIVERSITY OF TEXAS AT AUSTIN

December 2002

To my mother for her immeasurable love and support that allowed me to see  
my studies through to the end.

## Acknowledgments

This research would not have been possible without all the STAR collaborators and fellow students. I'd like to thank the UT RHIP group, especially Jerry Hoffmann and Lanny Ray for their patience and help in completing this research. I'd also like to thank the other students of our group, Bum Choi and Aya Ishihara, for making my stay at Brookhaven enjoyable. You can never play too much tennis! Within the STAR Strangeness Working Group, thanks go to Peter Jones and Helen Caines for their insight and leadership. Thanks also go to the strangness group's students and post-docs that helped me survive on a daily basis (in alphabetical order), Lee Barnby, Gene Van Buren, Javier Castillo, Boris Hippolyte, Matt Lamont, Hui Long, and Eugene Yamamoto. I'd like to extend my gratitude to Lee for graciously putting up with me as a roommate for two years, and to Gene and his wife, Marie, for teaching me so much about volleyball!

# Charged Xi Production in 130 GeV Au+Au Collisions at the Relativistic Heavy Ion Collider

Publication No. \_\_\_\_\_

Curtis Patrick Leon Lansdell, Ph.D.  
The University of Texas at Austin, 2002

Supervisor: Gerald W. Hoffmann

Presented here are the results of analysis of data for  $Au+Au$  at 130 GeV per nucleon pair. The data were taken by the STAR detector at RHIC. Production properties of  $\Xi^-$  and its anti-particle are investigated through the measurement of ratios and yields, which are compared to previous SPS results as well as various model predictions. An anti-particle to particle ratio of  $0.85 \pm 0.03(stat.) \pm 0.05(sys.)$  is found for the 10% most central events. An exponential fit to the transverse mass spectra results in mid-rapidity yields and inverse slope parameters of  $dN/dy = 1.98 \pm 0.08(stat.)$  and  $T = 358 \pm 7(stat.)$  for the particle, and  $dN/dy = 1.73 \pm 0.07(stat.)$  and  $T = 357 \pm 7(stat.)$  for the anti-particle. Systematic errors for the fit results are estimated to be  $\sim 20\%$ . The ratio, yields, and inverse slope parameters are observed to be greater than SPS measurements from  $Pb + Pb$  collisions at 17.3 GeV per nucleon

pair, indicating smaller net baryon content at mid-rapidity and hotter initial temperatures from the collisions at RHIC.

# Table of Contents

|  |            |
|--|------------|
| <b>Acknowledgments</b>                                     | <b>v</b>   |
| <b>Abstract</b>  | <b>vi</b>  |
| <b>List of Tables</b>                                      | <b>xi</b>  |
| <b>List of Figures</b>                                     | <b>xii</b> |
| <b>Chapter 1. Introduction</b>                             | <b>1</b>   |
| <b>Chapter 2. Physics</b>                                  | <b>5</b>   |
| 2.1 Deconfinement . . . . .                                | 5          |
| 2.1.1 Asymptotic Freedom . . . . .                         | 6          |
| 2.2 Chiral Symmetry Restoration . . . . .                  | 8          |
| 2.3 Critical Parameters . . . . .                          | 9          |
| 2.4 Space-Time Evolution . . . . .                         | 10         |
| 2.5 Strangeness Production . . . . .                       | 11         |
| 2.6 The $\Xi^-$ Particle . . . . .                         | 14         |
| 2.6.1 $\Xi^-$ Production in Heavy Ion Collisions . . . . . | 15         |
| <b>Chapter 3. Experimental Setup</b>                       | <b>18</b>  |
| 3.1 The Relativistic Heavy Ion Collider . . . . .          | 18         |
| 3.1.1 Year 2000 Run . . . . .                              | 22         |
| 3.2 The RHIC Experiments . . . . .                         | 24         |
| 3.3 Solenoidal Tracker at RHIC . . . . .                   | 25         |
| 3.4 Time Projection Chamber . . . . .                      | 27         |
| 3.4.1 Field Cages . . . . .                                | 28         |
| 3.4.2 Multi-Wire Proportional Chambers . . . . .           | 31         |
| 3.4.3 Drift Gas . . . . .                                  | 35         |



|                   |   |           |
|-------------------|---|-----------|
| 3.4.4             | Drift Field . . . . .                   | 37        |
| 3.4.5             | TPC Readout . . . . .                   | 39        |
| 3.5               | Event Triggering . . . . .              | 40        |
| 3.5.1             | Trigger Detectors . . . . .             | 40        |
| 3.5.2             | Trigger Levels . . . . .                | 43        |
| <b>Chapter 4.</b> | <b>Reconstruction</b>                   | <b>45</b> |
| 4.1               | Corrections . . . . .                   | 46        |
| 4.2               | Year 2000 Triggers . . . . .            | 47        |
| 4.3               | Event Selection . . . . .               | 47        |
| 4.4               | $\Xi$ Search . . . . .                  | 49        |
| <b>Chapter 5.</b> | <b>Analysis</b>                         | <b>55</b> |
| 5.1               | $\Xi$ Identification . . . . .          | 56        |
| 5.2               | Raw Particle Yields . . . . .           | 64        |
| 5.2.1             | Peak Fitting . . . . .                  | 64        |
| 5.2.2             | Background Fitting . . . . .            | 67        |
| 5.2.3             | Bin Counting . . . . .                  | 69        |
| 5.3               | Embedding Process . . . . .             | 70        |
| 5.4               | Correction Factors . . . . .            | 72        |
| 5.4.1             | Acceptance . . . . .                    | 72        |
| 5.4.2             | Reconstruction Efficiency . . . . .     | 73        |
| 5.4.3             | Total Correction . . . . .              | 76        |
| 5.5               | Simulation Quality Check . . . . .      | 79        |
| 5.5.1             | Distribution Comparisons . . . . .      | 81        |
| 5.5.2             | Lifetime Check . . . . .                | 82        |
| <b>Chapter 6.</b> | <b>Results and Discussion</b>           | <b>90</b> |
| 6.1               | Experimental Results . . . . .          | 90        |
| 6.1.1             | $\Xi^+$ to $\Xi^-$ Ratio . . . . .      | 90        |
| 6.1.2             | Transverse Mass Distributions . . . . . | 95        |
| 6.2               | Discussion . . . . .                    | 98        |
| 6.2.1             | $\Xi^+$ to $\Xi^-$ Ratio . . . . .      | 98        |

|                    |   |            |
|--------------------|---|------------|
| 6.2.2              | Corrected Spectra . . . . .   | 101        |
| 6.2.3              | Centrality Dependence of $\Xi^-$ and $\bar{\Xi}^+$ Production . . . . | 106        |
| 6.2.4              | Collective Behavior . . . . .   | 107        |
| <b>Chapter 7.</b>  | <b>Conclusion</b>   | <b>111</b> |
|                    | <b>Appendix</b>   | <b>115</b> |
| <b>Appendix 1.</b> | <b>Observables and Spectra</b>  | <b>116</b> |
|                    | <b>Bibliography</b>   | <b>118</b> |
|                    | <b>Vita</b>   | <b>124</b> |

# List of Tables

|     |  |     |
|-----|--|-----|
| 1.1 | Quark properties . . . . .                                     | 1   |
| 2.1 | Properties of the $\Xi^-$ baryon . . . . .                     | 14  |
| 3.1 | RHIC parameters and specifications . . . . .                   | 19  |
| 3.2 | IFC, OFC, gas vessel radiation lengths . . . . .               | 32  |
| 3.3 | Year 2000 MWPC operating parameters . . . . .                  | 35  |
| 4.1 | Centrality bins analyzed . . . . .                             | 50  |
| 4.2 | Basic reconstruction cuts . . . . .                            | 52  |
| 4.3 | Filter cuts . . . . .  | 53  |
| 5.1 | Final analysis cuts . . . . .                                  | 60  |
| 5.2 | Requirements for $\Xi^-$ Acceptance . . . . .                  | 73  |
| 5.3 | Requirements for Association . . . . .                         | 76  |
| 5.4 | Calculated $\Xi^- + \bar{\Xi}^+$ lifetimes . . . . .           | 89  |
| 6.1 | Uncorrected signal . . . . .                                   | 91  |
| 6.2 | Transverse mass fit results . . . . .                          | 96  |
| 6.3 | Predicted and measured non-identical particle ratios . . . . . | 105 |

# List of Figures

|      |  |    |
|------|--|----|
| 1.1  | QCD phase diagram . . . . .                                | 4  |
| 2.1  | Space-time evolution of the collision . . . . .            | 10 |
| 2.2  | Strangeness enhancement at WA97, NA57 . . . . .            | 13 |
| 3.1  | Arc dipole magnet cross-section . . . . .                  | 20 |
| 3.2  | BNL accelerator facilities . . . . .                       | 21 |
| 3.3  | First $\sqrt{s_{NN}} = 60$ GeV event, end view . . . . .   | 22 |
| 3.4  | First $\sqrt{s_{NN}} = 130$ GeV event, side view . . . . . | 23 |
| 3.5  | STAR detector . . . . .                                    | 26 |
| 3.6  | TPC cut-away view . . . . .                                | 27 |
| 3.7  | Inner Field Cage and inner sector dimensions . . . . .     | 28 |
| 3.8  | Outer Field Cage and outer sector dimensions . . . . .     | 29 |
| 3.9  | Outer Field Cage dimensions . . . . .                      | 30 |
| 3.10 | Inner Field Cage dimensions . . . . .                      | 30 |
| 3.11 | Gas Containment Vessel . . . . .                           | 31 |
| 3.12 | Multi-Wire Proportional Chamber . . . . .                  | 33 |
| 3.13 | TPC sector . . . . .                                       | 35 |
| 3.14 | Argon-Methane drift curves . . . . .                       | 38 |
| 3.15 | Trigger Detectors . . . . .                                | 41 |
| 3.16 | Trigger Plots . . . . .                                    | 42 |
| 4.1  | Primary vertex $z$ distribution . . . . .                  | 48 |
| 4.2  | Centrality class definitions . . . . .                     | 49 |
| 4.3  | Schematic representation of a $\Xi^-$ decay . . . . .      | 51 |
| 5.1  | $\Xi^- + \Xi^+$ invariant mass . . . . .                   | 56 |
| 5.2  | Variable versus variable I . . . . .                       | 58 |

|      |   |     |
|------|---|-----|
| 5.3  | Variable versus variable II . . . . .   | 59  |
| 5.4  | Phase-space coverage for $\Xi^-$ . . . . .  | 61  |
| 5.5  | $dE/dx$ versus momentum . . . . .   | 63  |
| 5.6  | Signal extraction via Breit-Wigner distribution . . . . .                           | 65  |
| 5.7  | Signal extraction via Gaussian distribution . . . . .                               | 66  |
| 5.8  | Signal extraction via double-Gaussian distribution . . . . .                        | 67  |
| 5.9  | Signal extraction via background fitting . . . . .                                  | 68  |
| 5.10 | Signal extraction via bin counting . . . . .  | 69  |
| 5.11 | Acceptance correction as a function of $(y, p_\perp)$ . . . . .                     | 74  |
| 5.12 | Acceptance correction as a function of $p_\perp$ . . . . .                          | 75  |
| 5.13 | $\Xi^-$ and $\Xi^+$ reconstruction efficiencies as functions of $p_\perp$ . . . . . | 77  |
| 5.14 | Total efficiencies for $\Xi^-$ and $\Xi^+$ . . . . .                                | 78  |
| 5.15 | Total $m_\perp$ efficiencies for $\Xi^-$ and $\Xi^+$ . . . . .                      | 80  |
| 5.16 | Distribution comparisons between simulated and real data I . . . . .                | 83  |
| 5.17 | Distribution comparisons between simulated and real data II . . . . .               | 84  |
| 5.18 | Distribution comparisons between simulated and real data III . . . . .              | 85  |
| 5.19 | Distribution comparisons between simulated and real data IV . . . . .               | 86  |
| 5.20 | Distribution comparisons between simulated and real data V . . . . .                | 87  |
| 5.21 | Raw yield and total efficiency as functions of $c\tau$ and $p_\perp$ . . . . .      | 87  |
| 5.22 | Corrected $\Xi^- + \Xi^+$ yield . . . . .   | 89  |
| 6.1  | $\Xi^+$ absorption rate . . . . .   | 91  |
| 6.2  | $\Xi^+/\Xi^-$ versus centrality . . . . .   | 92  |
| 6.3  | $\Xi^+/\Xi^-$ versus rapidity . . . . .   | 93  |
| 6.4  | $\Xi^+/\Xi^-$ versus $p_\perp$ . . . . .  | 94  |
| 6.5  | Fits to the $m_\perp$ distributions . . . . .                                       | 95  |
| 6.6  | $\bar{B}/B$ ratios at mid-rapidity . . . . .  | 99  |
| 6.7  | Non-identical particle ratios . . . . .   | 102 |
| 6.8  | Predicted and measured non-identical particle ratios . . . . .                      | 105 |
| 6.9  | $dN/dy$ vs. $dN_{h^-}/d\eta$ . . . . .  | 107 |
| 6.10 | $T$ vs. $dN_{h^-}/d\eta$ . . . . .  | 109 |

6.11 Inverse slope parameters as a function of mass . . . . . 110

# Chapter 1

## Introduction

The theory of Quantum Chromodynamics (QCD) describes interactions between particles never directly seen in nature, quarks and gluons, referred to collectively as partons. Partons, in addition to leptons, are well established as the building blocks of matter. Three generations of quarks have been observed, up ( $u$ ) and down ( $d$ ), strange ( $s$ ) and charm ( $c$ ), and bottom ( $b$ ) and top ( $t$ ). These and their corresponding anti-quarks ( $\bar{u}, \bar{d}, \bar{s}, \bar{c}, \bar{b}, \bar{t}$ ) constitute all known hadronic matter. Table 1.1 lists known characteristics of the quarks [49].

| Name    | Symbol | Mass (MeV)                | Charge ( $e$ ) | Quantum Number       |
|---------|--------|---------------------------|----------------|----------------------|
| up      | $u$    | $1.5 \rightarrow 5$       | $+\frac{2}{3}$ | $I_3 = +\frac{1}{2}$ |
| down    | $d$    | $3 \rightarrow 9$         | $-\frac{1}{3}$ | $I_3 = -\frac{1}{2}$ |
| strange | $s$    | $75 \rightarrow 170$      | $-\frac{1}{3}$ | Strangeness = $-1$   |
| charm   | $c$    | $1,150 \rightarrow 1,350$ | $+\frac{2}{3}$ | Charm = $+1$         |
| bottom  | $b$    | $4,000 \rightarrow 4,400$ | $-\frac{1}{3}$ | Bottom = $-1$        |
| top     | $t$    | $174,300 \pm 5,100$       | $+\frac{2}{3}$ | Top = $+1$           |

Table 1.1: Properties of the 6 known quarks.

Quarks are never seen as individual particles. Instead, they are strongly bound within hadrons which are further classified into baryons ( $qqq$ ) and mesons ( $q\bar{q}$ ). The most common examples of baryons are protons ( $uud$ ) and

neutrons ( $udd$ ), also referred to as nucleons, which form all of the visible stable matter in the universe.

The Pauli Exclusion Principle states that no two fermions may exist in the same quantum state. For this reason, quarks are given the quantum "number" classification of color, not listed in Table 1.1. The need for this classification is seen when examining such particles as  $\Delta^{++}$  ( $uuu$ ),  $\Delta^{-}$  ( $ddd$ ), and  $\Omega^{-}$  ( $sss$ ). Each of these particles has a spin of  $\frac{3\hbar}{2}$ , which means the constituent quarks must have parallel spin. By introducing color charge, the Pauli Exclusion Principle is not violated.

The color charges are referred to as red ( $r$ ), green ( $g$ ), and blue ( $b$ ). Since individual quarks remain unseen in nature, it is thought that color itself is confined, meaning hadrons are observed as colorless objects. In the case of mesons ( $q\bar{q}$ ), the anti-quark must carry the anti-color charge of the quark,  $\bar{r}$ ,  $\bar{g}$ , or  $\bar{b}$ , to remain a color-neutral combination.

Unlike Quantum Electrodynamics (QED) where the interactions are carried out via exchange of electric charge-neutral photons ( $\gamma$ ), the force carriers of QCD are not neutral objects; they carry color charge. The gauge bosons of QCD are the gluons ( $g$ ), so interactions between color-charged quarks are done via exchange of color-charged gluons. To facilitate the possible color interactions, there are 8 physical gluons carrying a color and an anti-color. Since the gluons carry color charges, they can in fact self-interact. This self-interaction is thought to be the reason for parton confinement within hadrons.



QCD is a non-Abelian gauge theory which exhibits asymptotic freedom [61]: the strong coupling constant  $\alpha_s$  diminishes at small distances or large momentum transfers. Lattice QCD calculations state that at vacuum temperatures of  $\sim 150$  MeV, hadrons dissociate and fuse such that a macroscopic space-time region is formed, composed of quarks and gluons that cannot be associated with any given hadron. This region of space-time is referred to as a quark-gluon plasma (QGP). A QGP is theorized to have existed about a microsecond after the Big Bang, when the energy density and temperature of the universe was still sufficiently high to produce a this parton soup [69]. Soon after this period, the universe expanded and cooled enough such that the coupling between quarks and gluons favored the formation of color-neutral bound states, i.e, the universe transitioned into hadronic matter. In the modern universe, examples of naturally formed QGPs might be the cores of dense neutron stars [61]. Figure 1.1 offers a pictorial representation of the QCD phases.

Relativistic heavy ion collisions are the key to probing high energy QCD phenomena in the laboratory. Previous experiments both at the Alternating Gradient Synchrotron (AGS) at Brookhaven National Laboratory (BNL) and the CERN SPS have been unable to offer definitive proof of a QCD phase transition. The Relativistic Heavy Ion Collider (RHIC), also located at BNL, produces center of mass energies that are 10 times greater than previous heavy ion experiments. These energetic collisions are studied by several RHIC experiments, including the Solenoidal Tracker at RHIC (STAR) collaboration, and

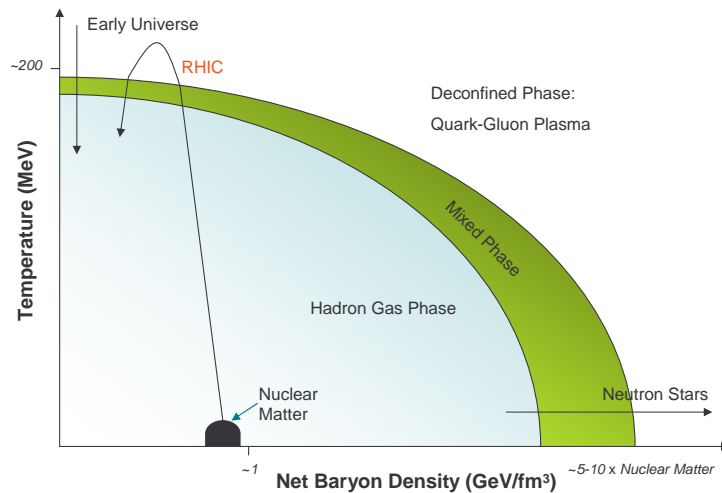


Figure 1.1: QCD phase diagram. RHIC collides heavy ions at high energies, recreating conditions similar to that which existed in the early universe.

may allow us to observe the predicted QCD phase transition. RHIC provides the ability to systematically measure the properties of strongly interacting matter by utilizing various ion species at different energies. This tool allows us to get one step closer to understanding the universe, both at its infant stages and at its current age.

The following discussion deals with experimentally identifying and then analyzing the  $\Xi^-$  and its anti-particle from data taken during the year 2000 physics run at BNL. Previous to this, some basic information concerning the QCD phase transition and how it applies to strange particle measurables is reviewed.

# Chapter 2

## Physics

The QCD phase transition is expected to lead to various effects in relation to the final state particles produced from a high energy heavy ion collision. The problem with quantitatively identifying this transition arises from the inability to observe directly the actual participants, quarks and gluons. Instead, various indirect measurements must suffice which, when taken together, may provide evidence of the deconfined phase. Of particular interest here is the prediction that the production of strange and anti-strange quarks will be enriched due to the deconfined phase over that of hadronic systems [45]. This asymptotically high temperature QCD phase describes a quasi-free state of partons, which can be modelled as a plasma of weakly interacting quarks and gluons.

### 2.1 Deconfinement

Nuclear matter at normal conditions exhibits confinement of the constituent partons. The potential between two quarks is

$$V(r) = -\frac{4\alpha_s}{3r} + kr \tag{2.1}$$

where  $\alpha_s$  is the strong coupling constant,  $k$  is a constant ( $\sim 1$  GeV/fm), and  $r$  is the separation between two quarks [61]. The potential between quarks is subject to the density of the force-carrying gluons shared among them. With increasing distance, the quarks exhibit increasing pull towards each other; the intermediary gluons form a color flux tube such that potential increases linearly with distance while the energy density  $k$  remains constant. The stored energy  $kr$  eventually reaches a point where it is energetically favorable to create a  $q\bar{q}$  pair, hence this linear term is associated with confinement at large  $r$ . Decreasing the distance between the quarks gives rise to a Coulomb-like  $1/r$  potential which comes from single gluon exchange, analogous to the second-order process of Coulomb scattering between two electrons, Rutherford scattering.

Equation 2.1 implies two color-charged quarks cannot be separated. However, by pushing the quarks closer to each other, it should be possible to achieve deconfinement if  $\alpha_s$  tends to 0 faster than  $r$ .

### 2.1.1 Asymptotic Freedom

An electron constantly emits and reabsorbs virtual photons which can produce virtual  $e^+e^-$  pairs. This cloud of virtual electrons and positrons produces a shielding effect called vacuum polarization in quantum electrodynamics (QED). The QED coupling constant can be approximated by [61]

$$\alpha(q^2) = \frac{\alpha_{em}}{1 - \frac{\alpha_{em}}{3\pi} \ln\left(\frac{q^2}{m_e^2}\right)} \quad (2.2)$$

where  $q$  is the momentum transfer being examined,  $m_e$  is the electron mass, and

$$\alpha_{em} = \frac{e^2}{4\pi\epsilon_0\hbar c} \quad (2.3)$$

is the fine structure constant,  $e$  being the charge of the electron. As  $q$  decreases, or the typical distance  $r \simeq 1/q$  increases, the effective coupling  $\alpha$  gets smaller. In other words, the bare charge is shielded to some extent. Conversely, the shielding effect becomes small at extremely short distances, or very high  $q$ , and one can obtain the potential due to the bare charge. The form of  $\alpha$  in Equation 2.2 is that of a running coupling constant which depends on the masses or momentum transfers involved in any particular case.

QCD quark interactions can also be represented by a running coupling constant,  $\alpha_s(q^2)$ . Similar to the QED case,  $q\bar{q}$  pairs produce a shielding effect on the value of a test quark. However, gluons also possess color charges and can produce gluon loops which leads to an anti-shielding effect. The effective coupling can be approximated by [61]

$$\alpha_s(q^2) = \frac{\alpha_s(q_0^2)}{1 + B\alpha_s(q_0^2) \ln(q^2/q_0^2)} = \frac{1}{B \ln(q^2/\Lambda^2)} \quad (2.4)$$

where  $B = (33 - 2n_f)/12\pi$ ,  $\Lambda = q_0^2 \exp[-1/(B\alpha_s(q_0^2))]$ ,  $q_0$  is some typical momentum transfer,  $q$  is again the momentum transfer at which the coupling constant is sampled, and  $n_f$  is the number of quark flavors. As long as  $n_f \leq 16$ ,  $\alpha_s(q^2)$  will decrease as  $q^2$  increases. Thus, at asymptotically large  $q^2$ , or very small distances,  $\alpha_s(q^2) \rightarrow 0$ . In this regime, the quarks act as if free which is referred to as asymptotic freedom.

## 2.2 Chiral Symmetry Restoration

Chiral symmetry relates to the helicity of quarks. Quarks that have their spin vectors aligned parallel or anti-parallel to their momentum vectors are said to be right or left handed, respectively. The helicity of particles is conserved exactly in an interaction with massless particles and so chiral symmetry is preserved. However, quarks in hadronic interactions have non-zero masses and so spontaneously break chiral symmetry. In other words, it is possible to transform to a frame of reference where the momentum and spin vectors are aligned opposite from that of a different frame. This means that chiral symmetry is broken since a quark can appear to be left or right handed, depending on the frame of reference.

At temperatures below the QCD phase transition to a QGP,  $\alpha_s$  is greater than zero and so interactions between quarks effectively increase their masses to values greater than the bare masses listed in Table 1.1. A quark's constituent mass is approximated from the hadron it makes up, as this mass includes the zero-point energy of the quark in the confining potential [71]. As nucleons have masses of about 1 GeV, the constituent  $u$  and  $d$  quarks are assigned masses of approximately 300 MeV. Similarly,  $s$  quarks are assigned a mass of approximately 500 MeV. Chiral symmetry is broken in this situation.

At high temperatures where  $\alpha_s$  tends to zero, the quarks obtain their bare, or current, masses. These current masses are still non-zero, implying chiral symmetry is not completely restored. However, a partial restoration of chiral symmetry is expected. In terms of relativistic heavy ion collisions,

this conclusion leads to the possibility of an increase in the production of heavier quarks. Strange quarks, being the lightest of these heavier quarks, will be produced in great amounts compared to normal hadronic channels as the temperature of the system approaches the mass of the  $s\bar{s}$  pair.

### 2.3 Critical Parameters

Estimates of the necessary energy density and temperature needed to produce a phase transition have been carried out using non-perturbative QCD simulations on a discrete Euclidean space-time lattice [53, 71]. Lattice QCD [70] calculations are done by placing quarks at discrete lattice points and connecting them with gluons in the form of a square. The number of lattice points used in a calculation is limited by the computing power available. In order to relate lattice spacing to physical scales, it is necessary to work with different lattice spacings until a scaling behavior occurs. In other words, the relationship between the coupling constant and the scale of the spatial spacing agrees with perturbative QCD calculations. Only when scaling behavior is seen can the relationship between lattice spacing and physical scales be made such that physical quantities from lattice QCD calculations can be extracted.

Recent calculations on the lattice estimate the critical temperature for the QCD phase transition to be  $T_c \simeq 175$  MeV [53]. Also, an energy density  $\epsilon_c \simeq 0.7$  GeV/fm<sup>3</sup> was found, though with an error of about 50% due to the uncertainty on the calculated  $T_c$ .

## 2.4 Space-Time Evolution

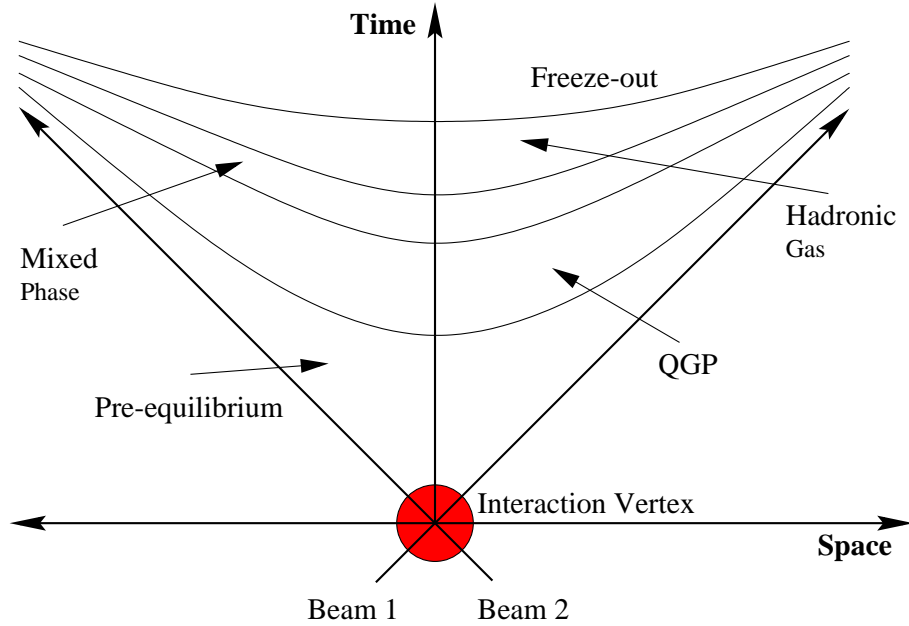


Figure 2.1: Space- time evolution of the collision between two beams in the center of mass frame, assuming the formation of a QGP.

Assuming the production of a quark-gluon plasma from the collision of two heavy ions, Figure 2.1 depicts the space-time evolution of a heavy ion collision in the center of mass frame. The initial collision creates new particles and is referred to as the pre-equilibrium stage, where partons represent the relevant degrees of freedom in the fireball. The system of partons becomes denser as more are created, eventually reaching a point where, due to the high temperature and energy density in the fireball, they only weakly interact with each other. When this occurs and the fireball equilibrates, the state of matter is known as a quark-gluon plasma. The QGP expands and cools down until a



point is reached where the partons hadronize. The cooling of the system continues until the hadrons no longer have inelastic interactions, meaning that particles are no longer created or destroyed. This stage is referred to as chemical freeze-out and is characterized by the temperature  $T_{ch}$ . Further cooling and expansion leads to the end of elastic collisions so that each particle's momentum is fixed. This final stage is referred to as thermal freeze-out and is characterized by the temperature  $T_{th}$ . If the expansion of the fireball is rapid enough, then it is expected that  $T_{ch}$  and  $T_{th}$  are similar.

## 2.5 Strangeness Production

Rafelski proposed the production of strange ( $s$ ) and anti-strange ( $\bar{s}$ ) quarks as a probe to study the QCD phase transition two decades ago [64]. Strange particles are of particular interest in hadronic collisions because they carry a quantum number, strangeness, not present in the participant nucleons.

In the absence of a QGP, strangeness production occurs via hadronic channels and involve relatively high energy thresholds, as in the examples below.

$$\pi + N \rightarrow \Lambda + K \quad E_{threshold} \simeq 530 \text{ MeV} \quad (2.5)$$

$$K + \pi \rightarrow \bar{\Lambda} + N \quad E_{threshold} \simeq 1420 \text{ MeV} \quad (2.6)$$

The transition to a QGP state opens new avenues of strangeness production through gluonic degrees of freedom which contribute approximately 80% to the total strangeness produced [55]. Partial restoration of chiral symmetry is

also expected to aid in the production of strangeness due to the lower energy threshold for  $s\bar{s}$  pair production (see §2.2). This leads to the prediction of significant strangeness enhancement if a phase transition to a QGP occurs.

$$q + \bar{q} \rightarrow s + \bar{s} \quad E_{threshold} \simeq 2m_s \simeq 300 \text{ MeV} \quad (2.7)$$

$$g + g \rightarrow s + \bar{s} \quad (2.8)$$

This enhancement in the production of strange hadrons should be most noticeable when examining multi-strange particles such as the  $\Xi^-$  and  $\Omega^-$ , which are rarely produced in hadronic interactions due to high reaction threshold energies. Koch, Müller, and Rafelski [55] have done quantitative theoretical calculations which support the conclusion of strangeness enhancement in a QGP as compared to production in a hadron gas.

Large increases in strange to non-strange particle yields have been reported in central light ( $Si, S$ ) [1, 15, 17, 19] and heavy ( $Au, Pb$ ) [14, 16, 18, 26, 37, 59] ion collisions using the BNL AGS and CERN SPS accelerators when compared to  $p + p$  collisions. The BNL RHIC collider has also released similar results recently [8]. However, the complexity of hadronic interactions in  $A + A$  collisions does not easily allow a true understanding of strangeness enhancement mechanisms. This difficulty of interpretation suggests the use of simpler  $p + A$  collisions to provide another basis for understanding.

The production rate of strange particles can be directly connected to the scattering dynamics of the incoming proton when examining the simpler final state of  $p + A$  collisions. The BNL E910 experiment using the AGS recently

produced results from  $p + Au$  collisions at a beam energy of 17.5 GeV/c [43]. The experiment studied strangeness enhancement as a function of centrality. They showed that at AGS energies, strange particle yields grew faster in  $p + A$  collisions than compared to a simple number of participants ( $N_{part}$ ) scaling of  $p + p$  data. At the SPS, measurements of strange baryons in  $Pb + Pb$  collisions by the WA97 and NA57 collaborations also show an enhancement when compared to  $p + Be$  and  $p + Pb$  [25]. This is shown in Figure 2.2.

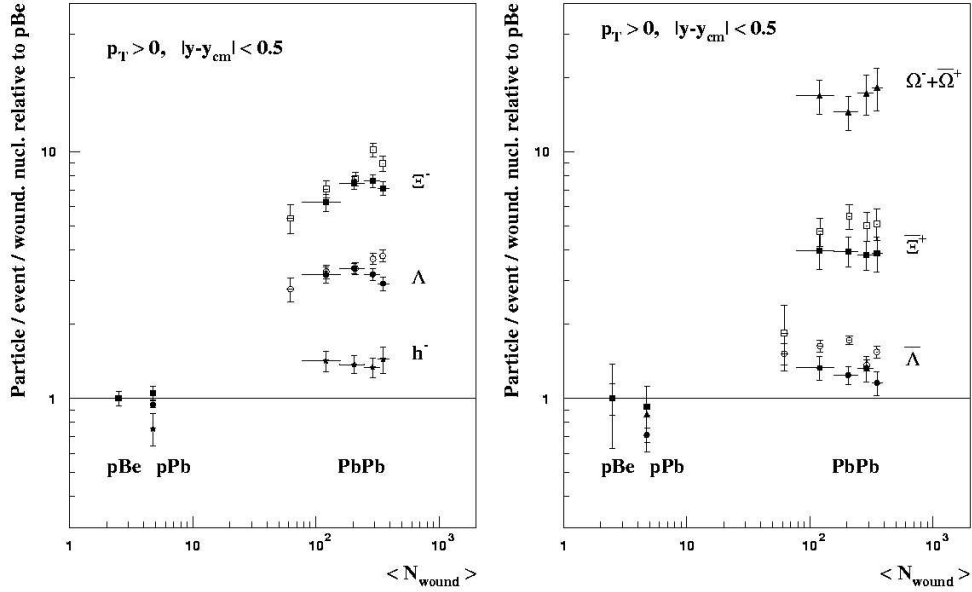


Figure 2.2: Strangeness enhancement in  $Pb + Pb$  collisions compared to  $p + Be$  and  $p + Pb$  seen at WA97 (closed symbols) and NA57 (open symbols) as a function of the number of participant, or wounded, nucleons [20]. Taken from [25].

The implications of this scaling violation when analyzing  $A + A$  collisions are important. Any study of enhancement in  $A + A$  collisions requires consideration of the multiple scattering of each participant nucleon, since the

dynamics of strangeness production may be quite sensitive to these additional scatters. Measurements of the centrality dependence of strangeness production are thus necessary to resolve this problem. A detailed study of both  $p+p$  and  $p+A$  collisions at RHIC will be useful in identifying a new state of matter from high energy  $A+A$  collisions.

## 2.6 The $\Xi^-$ Particle

The  $\Xi^-$  baryon (also known as a cascade particle due to its two-stage decay process) has two of its valence quarks being strange quarks ( $ssd$ ). The dominant decay mode has all of its final state particles with non-zero electric charge, allowing for easier identification in detectors. It is expected that the more strange valence quarks a hadron carries, the greater its sensitivity to conditions that enhance strangeness. As a baryonic measure of strangeness, the  $\Xi^-$  particle is then only surpassed by the  $\Omega^-$  which has all three valence quarks being strange ( $sss$ ). The major properties of the  $\Xi^-$  are listed in Table 2.1.

| $\Xi^-$ Baryon           |                            |
|--------------------------|----------------------------|
| Mass                     | 1321.31 MeV/c <sup>2</sup> |
| Lifetime ( $c\tau$ )     | 4.91 cm                    |
| Branching Ratios         |                            |
| $\Lambda\pi$             | 99.9%                      |
| $\Sigma^-\gamma$         | 0.01%                      |
| $\Lambda e^-\bar{\nu}_e$ | 0.06%                      |

Table 2.1: Some properties of the  $\Xi^-$  baryon. The dominant decay mode occurs nearly 100% of the time. Taken from [49].

The formation of the anti-particle,  $\Xi^+$  ( $\bar{s}\bar{s}\bar{d}$ ), is in a sense purer than the  $\Xi^-$ . The  $\Xi^+$  provides a better measure of quarks produced from the fireball since strange anti-baryons are not abundantly produced in secondary interactions compared to strange baryons due to a higher production energy threshold. Thus, any enhancement in their production rates should be explainable by some new process, such as the production of a QGP, where  $s\bar{s}$  pairs are copiously generated.

### 2.6.1 $\Xi^-$ Production in Heavy Ion Collisions

Several mechanisms are available in heavy ion collisions which lead to the production of  $\Xi^-$  particles. In a high energy heavy ion collision, pions are produced in great numbers compared to other hadrons. Without the production of a QGP and its greater degrees of freedom in  $s\bar{s}$  pair production, the path to multi-strange baryon formation is taken through several binary collisions between hadrons, such as

$$\pi + N \rightarrow K + \Lambda, \pi + \Lambda \rightarrow K + \Xi, \pi + \Xi \rightarrow K + \Omega \quad (2.9)$$

in the case of  $q\bar{q} \rightarrow s\bar{s}$  reactions and

$$\bar{K} + N \rightarrow \Lambda + \pi, \bar{K} + \Lambda \rightarrow \Xi + \pi, \bar{K} + \Xi \rightarrow \Omega + \pi \quad (2.10)$$

in the case of strange quark exchange reactions.

Including the possibility of deconfined quark and gluon matter allows for more  $s\bar{s}$  pairs to form, bringing the abundance of  $\Xi^-$  particles up signifi-

cantly. A transition from a hadronic gas phase to a QGP should bring with it noticeable dynamical changes, such as in single particle spectra.

Such changes should manifest themselves in extracted freeze-out parameters from the invariant differential cross section. Consider

$$E \frac{d^3\sigma}{dp^3} = \text{const.} \frac{1}{2\pi p_\perp} \frac{d^2N}{dp_\perp dy} \quad (2.11)$$

where the terms have been rewritten using the common observables of rapidity and transverse momentum. A particle species' multiplicity distribution can be written as

$$\frac{1}{2\pi m_\perp} \frac{d^2N}{dm_\perp dy} = \frac{dN/dy}{2\pi T(m_0 + T)} e^{-(m_\perp - m_0)/T} \quad (2.12)$$

where  $dN/dy$  is the rapidity distribution,  $m_\perp$  is the transverse mass,  $m_0$  is the rest mass, and  $T$  is the effective temperature which is usually referred to as the inverse slope parameter (see Appendix 1 for more details). Equation 2.12 is advantageous because with just one fit function, both the yield and the inverse slope parameter can be extracted. This form of the particle multiplicity also allows for direct comparison to previous experimental results, since it is used often in the literature.

The inverse slope parameter is commonly referred to as the temperature; however, it is generally accepted that this parameter actually is the freeze-out temperature of the particle species in conjunction with transverse flow. A transverse velocity boost is given to the particles exiting the expanding fireball, so that the effective temperature, or inverse slope parameter, may

be written in an empirical manner [30] as

$$T_{eff} = T_{fo} + m\langle\beta\rangle^2, \quad (2.13)$$

where  $T_{fo}$  and  $\langle\beta\rangle$  are the freeze-out temperature and the average collective flow velocity, respectively.

# Chapter 3

## Experimental Setup

### 3.1 The Relativistic Heavy Ion Collider

Practical investigation of QCD phenomena is done using high energy collisions of matter in particle accelerators and colliders. The Relativistic Heavy Ion Collider (RHIC) located at Brookhaven National Laboratory is designed to accelerate heavy ions to nearly the speed of light in two concentric collider rings. Running at an approximate luminosity of  $10^{26} \text{ cm}^{-2}\text{s}^{-1}$  using  $Au$  ions, RHIC can provide beam energies ranging from 30 GeV/u to 100 GeV/u. This corresponds to  $\sqrt{s_{NN}}$  energies ranging from 60 GeV to 200 GeV. Until the Large Hadron Collider (LHC) at CERN is complete, RHIC remains the highest energy collider in existence, taking  $Au$  ions to 99.995% the speed of light. RHIC is also designed to accelerate polarized and unpolarized proton beams to a maximum energy of 250 GeV/u. Besides supplying important baseline information with respect to A+A collisions, p+p collisions will provide data on the proton spin problem where it has been shown that the valence quarks of protons do not provide the total spin observed [27]. Table 3.1 lists some parameters and specifications of RHIC.

RHIC is composed of two concentric superconducting synchrotrons with



| RHIC Parameters and Specifications                      |                         |                         |
|---|-------------------------|-------------------------|
| No. Intersection Regions                                |                         | 6                       |
| No. Bunches/ring  |                         | 60                      |
| Bunch Spacing (ns)                                      |                         | 213                     |
| Collision Angle   |                         | 0                       |
| Free Space at Crossing Point (m)                        |                         | $\pm 9$                 |
|   | <i>Au</i>               | <i>p</i>                |
| No. Particles/bunch                                     | $10^9$                  | $10^{11}$               |
| Top Energy (GeV/u)                                      | 100                     | 250                     |
| Luminosity, average ( $\text{cm}^{-2}\text{sec}^{-1}$ ) | $\sim 2 \times 10^{26}$ | $\sim 1 \times 10^{31}$ |
| Lifetime (h)  | $\sim 10$               | $> 10$                  |

Table 3.1: RHIC parameters and specifications taken from [62].

2.4 mi diameters. The RHIC rings use superconducting magnets to guide the ion beams to six collisions points. The magnet system is mainly composed of 288 arc dipoles, 108 insertion dipoles, 276 arc quadrupoles, and 216 insertion quadrupoles. In addition to these magnets, there are also 72 trim quadrupoles, 288 sextupoles, and 492 corrector magnets at each quadrupole. The arc dipoles have a physical length of 9.728 m (9.45 m effective), are bent with a 4.85 cm sagitta and have a coil aperture of 8 cm (see Figure 3.1). These dimensions were chosen to accommodate the requirements due to intrabeam scattering. The beams in the arcs are designed to be 90 cm apart. The magnets are cooled to a temperature  $< 4.6$  K by circulating super-critical helium provided by 24.8 kW refrigerators. The cold bore can obtain pressures of  $< 10^{-11}$  mbar in an absence of leaks into it. To avoid beam loss and radiation background, the warm beam tube sections of the insertion regions must maintain a vacuum pressure of  $\sim 7 \times 10^{-10}$  mbar.

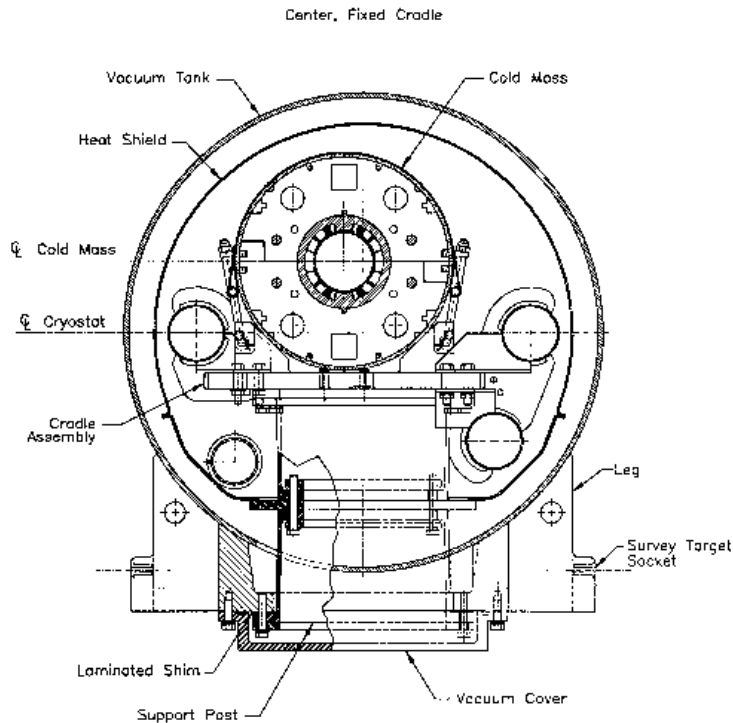


Figure 3.1: Cross-section of a typical arc dipole magnet.

RHIC does not exist on its own. It makes use of pre-existing equipment at BNL, including Tandem Van de Graaff accelerators, the Booster Synchrotron, and the Alternating Gradient Synchrotron (AGS). Figure 3.2 shows the layout of the complex. The path of the *Au* atoms begins in the Pulsed Sputter Ion Source in the Tandem Van de Graaff facility with a charge of  $-1$ . These atoms are accelerated and passed through two thin *Au* foils which strip the *Au* atoms of some electrons, leaving them with a net charge of  $+32$ . The Booster Synchrotron takes the  $1 \text{ MeV/u}$  *Au* beam and accelerates it to  $95 \text{ MeV/u}$  and further strips the ions to a net charge of  $+77$ . The beam is then fed into the AGS where it is bunched and accelerated to  $10.8 \text{ GeV/u}$ .

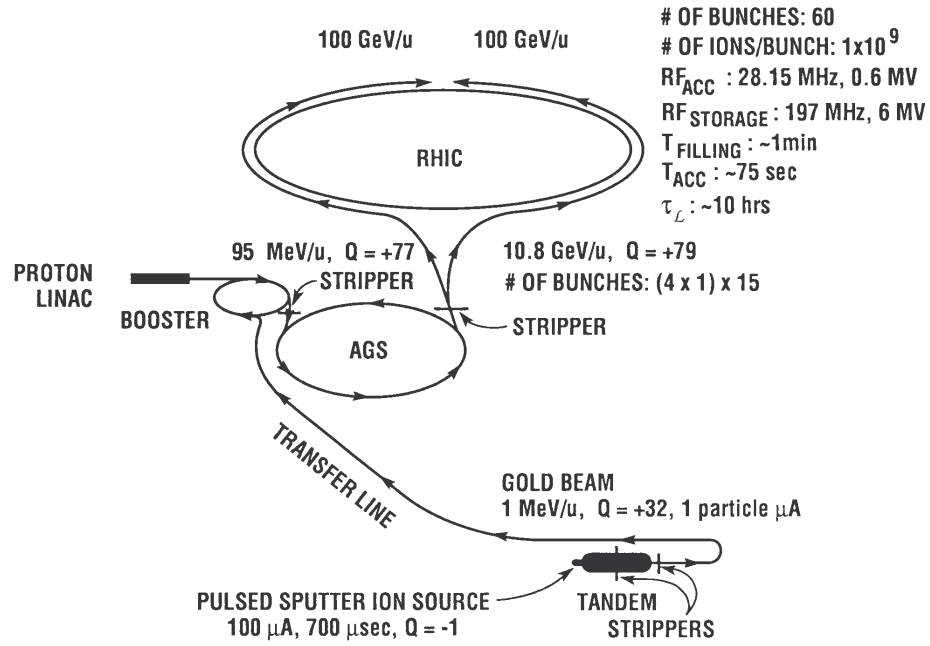


Figure 3.2: BNL accelerator facilities. Ions begin at the Pulsed Sputter Ion Source while protons begin at the Proton LINAC.

The bunched beam is extracted to the AGS to RHIC (AtR) line via a fast extraction beam (FEB) system. The FEB system is capable of performing single bunch multiple extraction of both a heavy ion beam or a high intensity proton beam at a rate of 30 Hz [66]. Multiple AGS bunches are injected into a single RHIC bunch and put into a waiting radio frequency ( $rf$ ) bucket through the AtR. The  $Au$  atoms are stripped of their last two electrons and are injected into RHIC with a charge of +79. RHIC is designed to handle up to 60 bunches where each bunch contains approximately  $10^9$   $Au$  ions. Once in RHIC, the  $Au$  bunches are accelerated to the final collision energy and stored for data taking.

### 3.1.1 Year 2000 Run

In June 2000, the STAR experiment recorded the first beam-beam collision at the injection energy  $\sqrt{s_{\text{NN}}} = 20$  GeV. Soon after, RHIC collided *Au* beams at an energy of  $\sqrt{s_{\text{NN}}} = 60$  GeV (Figure 3.3), proving RHIC operational for accelerating and colliding heavy ions. For the physics program, RHIC provided a final collision energy of  $\sqrt{s_{\text{NN}}} = 130$  GeV (Figure 3.4), which the data presented in this work are taken from.

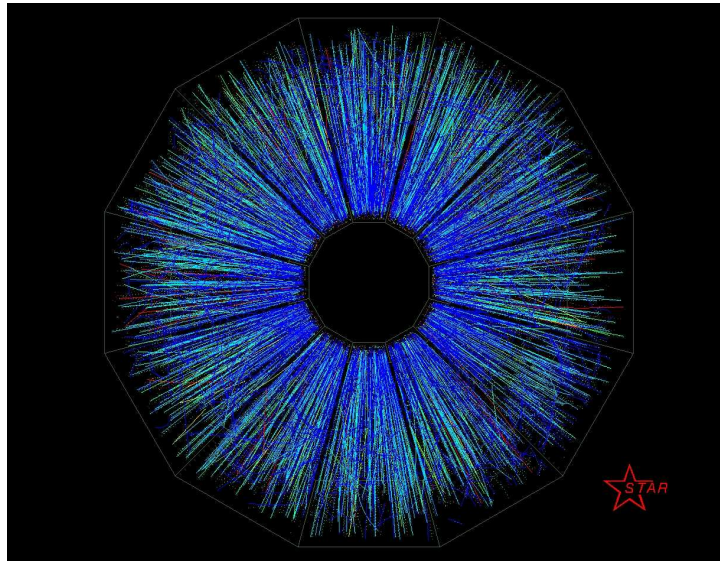


Figure 3.3: First  $\sqrt{s_{\text{NN}}} = 60$  GeV event, end view.

Several limitations existed for the first physics run. Firstly, the beam luminosity was approximately 10% of the design specification. Also, the *rf* system was not operational either, allowing bunches circulating in the RHIC rings to be spread over a relatively large region of space. This produced a large distribution in the primary vertex position along the beam axis. The design

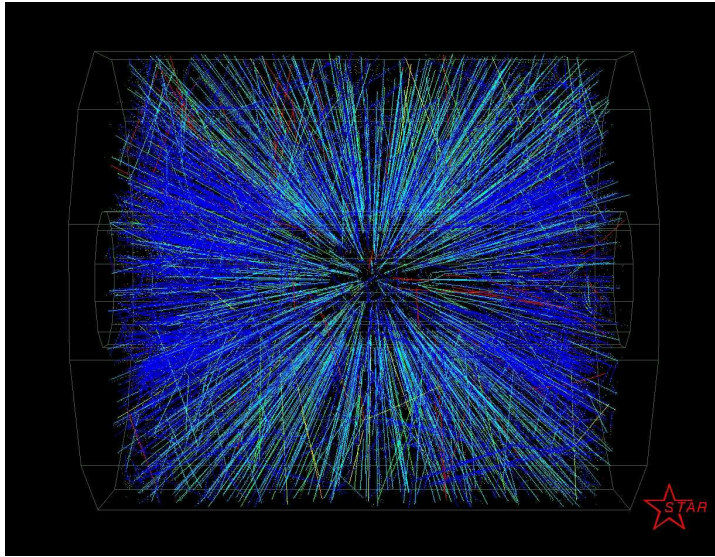


Figure 3.4: First  $\sqrt{s_{NN}} = 130$  GeV event, side view.

calls for 18 cm diamond lengths. Instead, STAR observed collision vertices with a Gaussian sigma of 70 to 100 cm for the  $z$  position. Naturally, the acceptance of the STAR detector is dependent on the position of the collision vertex and hence this large diamond was of some concern. The beam pipe section centered at each interaction point is made of beryllium ( $Be$ ) due to having an order of magnitude smaller radiation length than aluminum or steel, which are more commonly used materials. This means less multiple scattering and fewer produced particles due to the beam pipe near the interaction regions. However, due to the large diamond and the fact that the  $Be$  section only has a length of 150 cm, a significant fraction of events produced particles that traversed the non-beryllium sections where the radiation length is greater.

Large background rates were measured by STAR from beam interac-

tions with gas molecules in the beam pipe. Recall that there is an order of magnitude difference in vacuum pressure between the cold and warm bore sections. The warm bore section is a straight piece of the beam pipe that exists near each interaction point of RHIC. This is not an actively cooled section and is prone to more beam-gas events than the cold bore section.

Even with these limitations, a large number of useable events were collected for analysis.

## 3.2 The RHIC Experiments

Currently, four of the six interaction points have experiments built around them. The two largest detectors, STAR (Solenoidal Tracker at RHIC) and PHENIX (Pioneering High Energy Nuclear Interaction Experiment), are located at the 6 and 8 o'clock positions, respectively. The smaller experiments, BRAHMS (Broad Range Hadron Magnetic Spectrometers) and PHOBOS, are located at the 2 and 10 o'clock positions, respectively.

The BRAHMS experiment is designed to measure  $\pi^\pm$ ,  $p^\pm$ , and  $K^\pm$  in the region  $0 < |y| < 4$  and  $0.2 < p_T < 3$  GeV/c. Having two detector arms, one at forward rapidity and one near mid-rapidity, BRAHMS is able to provide information on baryon-poor and baryon-rich regions of particle production.

The PHOBOS experiment centers around a search for fluctuations in the number of produced particles and their angular distributions as a way of identifying a phase transition from normal nuclear matter to a QGP state.

The detector is able to study 1% of the produced particles in detail while also offering a global picture of the collision event. PHOBOS measures quantities such as the temperature, size, and density of the collision fireball.

The PHENIX experiment specializes in examining leptons and photons coming from the collision fireball. Besides the quest to help identify the existence of QGPs, PHENIX also hopes to aid in uncovering the reasons behind the proton's spin structure, since the three valence quarks are known to not carry all of the spin [28]. There are over 400 physicists working with this detector.

The STAR experiment also has roughly 400 collaborators involved in it. STAR is designed to give information on many observables, both inclusively and on an event by event basis. Due to the significantly increased particle production at RHIC as compared to previous colliders and also the hard parton-parton scattering in heavy ion collisions, STAR is able to measure observables that help determine single-event variables such as entropy, baryochemical and strangeness chemical potentials, temperature, fluctuations, and particle and energy flow. High transverse momentum  $p_T$  processes are also examined via high  $p_T$  jets, mini-jets, and single particles.

### **3.3 Solenoidal Tracker at RHIC**

The design of the STAR experiment allows for the measurement of various types of particles within a large acceptance, extending a full  $2\pi$  in azimuth and with  $|\eta| < 2$ . STAR is expected to undergo upgrades of current

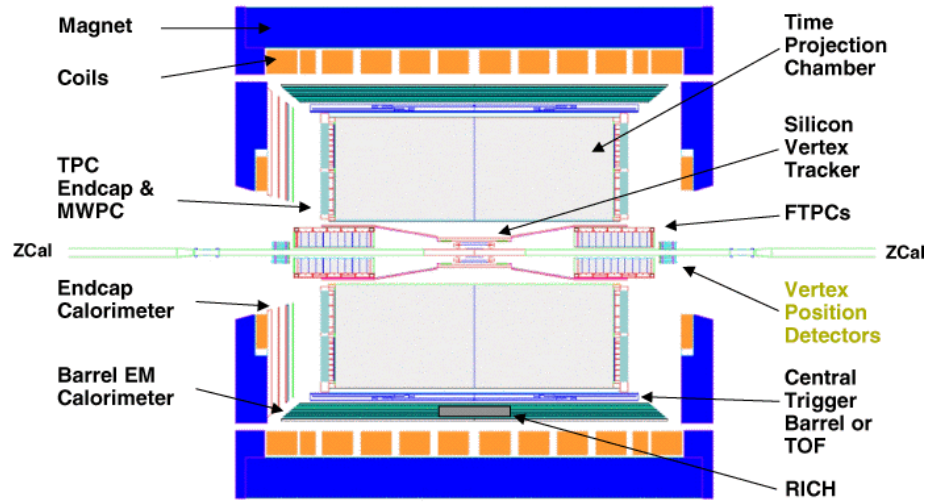


Figure 3.5: Schematic of the STAR detector. For the year 2000 running period the FTPCs, VPDs, TOF, EMCs, and SVT were not installed.

and installation of new detectors within the next several years. The complete STAR system is depicted in Figure 3.5. The STAR detector in its first physics run configuration was composed of a cylindrical Time Projection Chamber (TPC), a Central Trigger Barrel (CTB), a Ring-Imaging Cherenkov Counter (RICH), and two Zero-Degree Calorimeters (ZDCs). A solenoidal magnet surrounds the detectors and provides a nearly homogenous magnetic field along the length of STAR. For the first running period, the magnetic field was run at quarter of its maximum power, resulting in a 0.25 T field as opposed to the full 0.5 T possible.

The Silicon Vertex Tracker (SVT) and Forward TPCs (FTPCs) were not installed at the time of the first physics run, hence the main TPC was the only available tracking detector.



### 3.4 Time Projection Chamber

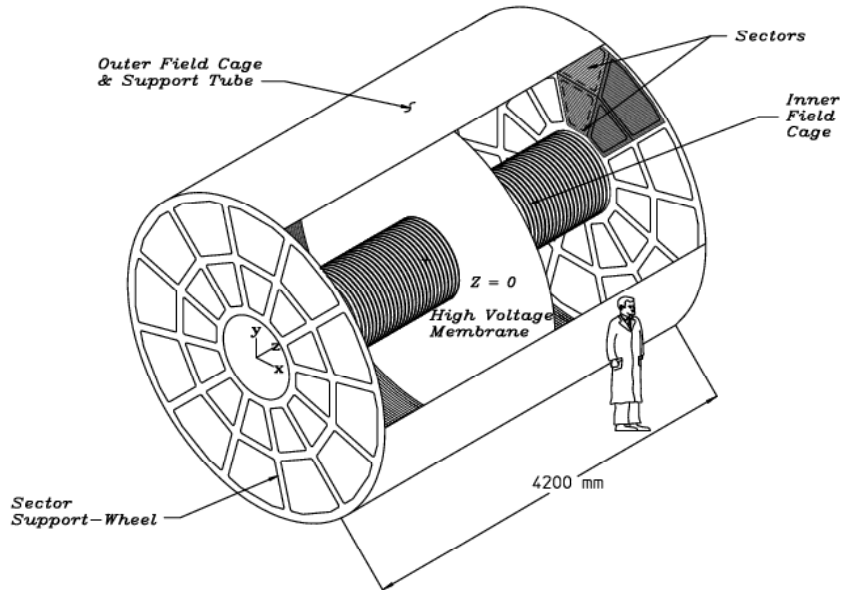


Figure 3.6: TPC cut-away view. Each half of the TPC is essentially a separate detector since there are readout electronics on each end.

The TPC [2] (Figure 3.6) is a cylindrical detector with an active volume filled with P10 (90%  $Ar$ , 10%  $CH_4$ ) gas within inner and outer field cages and a Multi-Wire Proportional Chamber (MWPC) [36] on each end for readout. The inner and outer field cages in conjunction with the central membrane supply a steady electric field of 148 V/cm in which the ionization electrons drift to the pad planes on each end of the TPC. The central membrane is a thin cathode held at  $-31$  kV and is located in the middle of the TPC. The pad planes are held at ground potential so as to create the longitudinal electric field. The

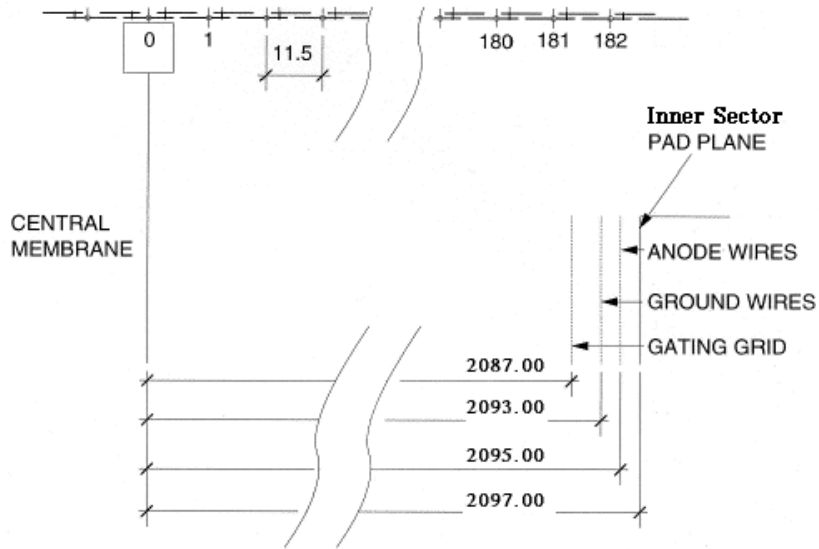


Figure 3.7: Inner Field Cage and inner sector dimensions, in millimeters.

inner and outer field cages both use a series of gradient rings which are biased by a chain of resistors. There are 182 rings and 183 resistors in each chain, the last two resistors having variable resistance. The total distance from the CM to either the inner or outer sectors is slightly more than 2 m. Figures 3.7 and 3.8 detail the longitudinal dimensions for the inner and outer field cages.

### 3.4.1 Field Cages

The field cages are composed of metal-coated Kapton separated by a honeycomb of Nomex. The outer field cage is coated with a  $35 \mu\text{m}$  layer of *Cu* and etched into stripes. After rolling the material into a tube, the stripes become 10 mm wide rings separated by a distance of 11.5 mm, as measured

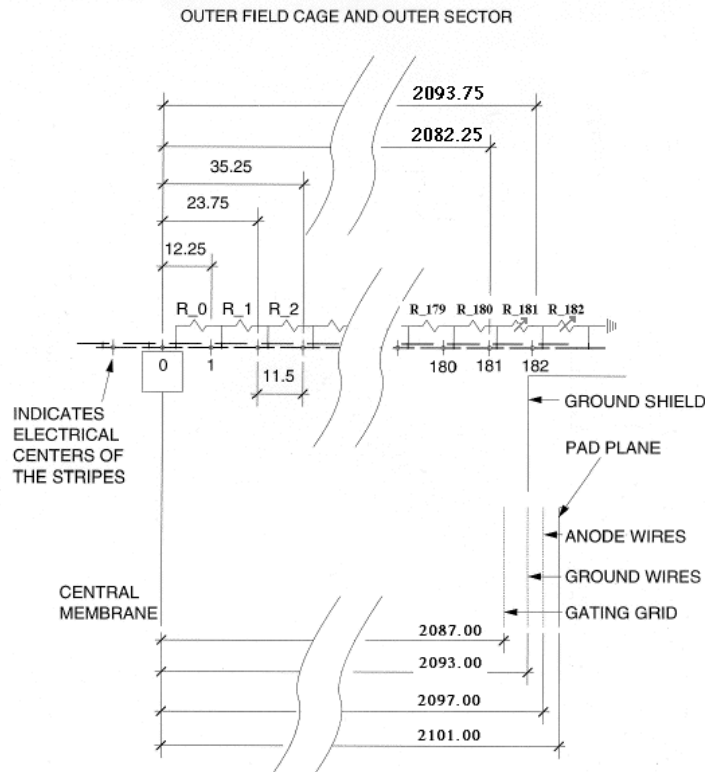


Figure 3.8: Outer Field Cage and outer sector dimensions, in millimeters.

from the center of each ring (Figure 3.9). The inner field cage is similar to the outer field cage except that the Kapton is coated with a  $9 \mu\text{m}$  layer of *Al* (Figure 3.10).

The two sides of the tube are connected by metal pins. The stripes on one side are centered over the gaps between stripes on the other side. This permits the metal layers to act as part of the mechanical structure of the tube, increasing the strength. This configuration also places metal opposite to the

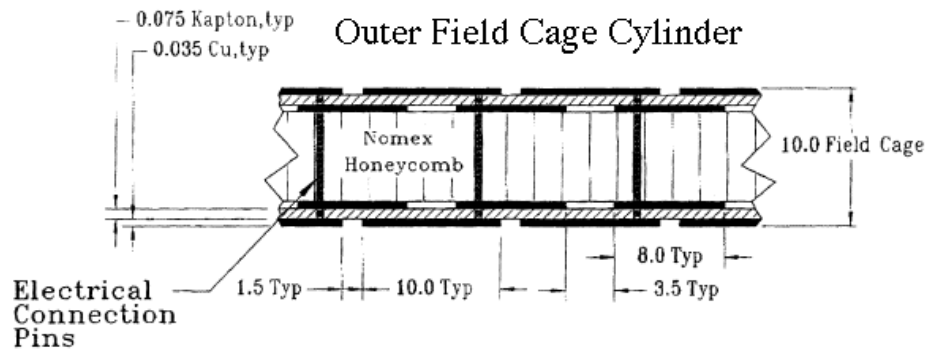


Figure 3.9: Outer Field Cage dimensions, in millimeters.

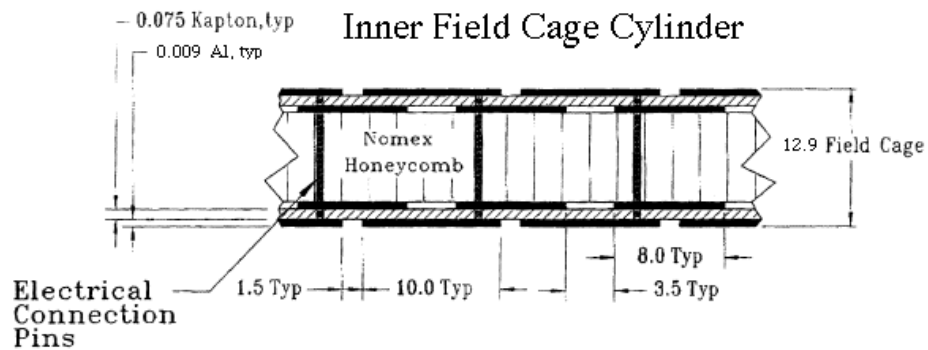


Figure 3.10: Inner Field Cage dimensions, in millimeters.

gaps in the rings facing the TPC volume. Image charges that develop on the opposite side of the gaps are expected to reduce the field distortions that might be caused by charge build up on the exposed Kapton in the gaps facing the TPC.

The outer field cage is held within an *Al* gas containment vessel. The vessel is 5.7 cm away from the outer field cage and the intervening volume is filled with  $N_2$  (Figure 3.11). *Al* brackets are glued to the outer circumference of the gas vessel to support the CTB trays and also to temperature stabilize

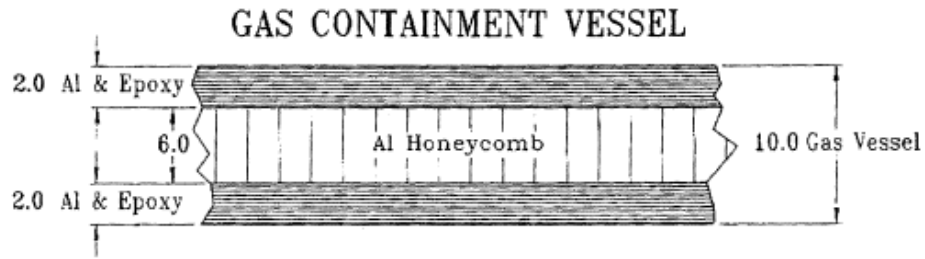


Figure 3.11: The Outer Field Cage is nested inside an *Al* gas containment vessel.

the TPC.

The materials used to construct the field cages were chosen based on several factors, including their permeability to passing particles. Excluding the TPC drift gas, the outer and inner field cages have radiation lengths of 1.26% and 0.62%, respectively. Table 3.2 details the IFC, OFC, and gas vessel radiation lengths.

### 3.4.2 Multi-Wire Proportional Chambers

On each end of the TPC is a Multi-Wire Proportional Chamber (MWPC). The MWPCs are composed of three wire planes and a pad plane connected to the front-end readout electronics (Figure 3.12). The gating grid, the ground grid, and the anode grid make up the three wire planes. The ground and gating grids help define the drift field in the TPC while the anode wires are biased to a high voltage to provide the right conditions to produce an avalanche of electrons from track ionization. Near the end of the TPC drift volume, the ionization electrons are accelerated towards the grid of anode wires. These accelerating electrons in turn ionize more gas molecules producing more electrons

| Material and Radiation Lengths |               |             |                                |                               |                             |                |
|--------------------------------|---------------|-------------|--------------------------------|-------------------------------|-----------------------------|----------------|
| Structure                      | Material      | $L$<br>(cm) | $\rho$<br>(g/cm <sup>3</sup> ) | $X_0$<br>(g/cm <sup>2</sup> ) | $x$<br>(g/cm <sup>2</sup> ) | $x/X_0$<br>(%) |
| Insulating Gas                 | $N_2$         | 30.00       | 0.001                          | 37.99                         | 0.038                       | 0.10           |
| IFC                            | $Al$          | 0.004       | 2.700                          | 24.01                         | 0.010                       | 0.04           |
| IFC                            | Kapton        | 0.015       | 1.420                          | 40.30                         | 0.022                       | 0.05           |
| IFC                            | Nomex         | 1.27        | 0.064                          | 40                            | 0.081                       | 0.20           |
| IFC                            | Adhesive*     | 0.08        | 1.20                           | 40                            | 0.091                       | 0.23           |
| <b>IFC Total<br/>(w/gas)</b>   |               |             |                                |                               |                             | <b>0.62</b>    |
| OFC                            | $Cu$          | 0.013       | 8.96                           | 12.86                         | 0.116                       | 0.91           |
| OFC                            | Kapton        | 0.015       | 1.420                          | 40.30                         | 0.022                       | 0.05           |
| OFC                            | Nomex         | 0.953       | 0.064                          | 40                            | 0.061                       | 0.15           |
| OFC                            | Adhesive*     | 0.05        | 1.20                           | 40                            | 0.060                       | 0.15           |
| <b>OFC Total</b>               |               |             |                                |                               |                             | <b>1.26</b>    |
| <b>TPC Gas</b>                 | P10           | 150.00      | 0.00156                        | 20.04                         | 0.234                       | <b>1.17</b>    |
| Insulating Gas                 | $N_2$         | 5.70        | 0.001                          | 37.99                         | 0.007                       | 0.02           |
| Gas Vessel                     | $Al$          | 0.40        | 2.590                          | 24.01                         | 1.036                       | 4.31           |
| Gas Vessel                     | Honeycomb     | 0.60        | 0.037                          | 24.01                         | 0.022                       | 0.09           |
| Gas Vessel                     | $Al$ Brackets | 0.635       | 2.590                          | 24.01                         | 1.645                       | 6.85           |
| Gas Vessel                     | Adhesive*     | 0.157       | 1.20                           | 40                            | 0.189                       | 0.47           |
| <b>Gas Vessel<br/>Total</b>    |               |             |                                |                               |                             | <b>11.74</b>   |

Table 3.2: Material and radiation lengths for the IFC, OFC, and gas containment vessel from [67]. \*Adhesive numbers are estimates. A material's radial thickness and density are represented by  $L$  and  $\rho$ .  $X_0$  is the radiation length and  $x/X_0$  is the thickness of the material in radiation lengths. To get the total radiation length budget between the vertex and some part of the detector, the beam pipe, SVT, and CTB trays might also be considered.

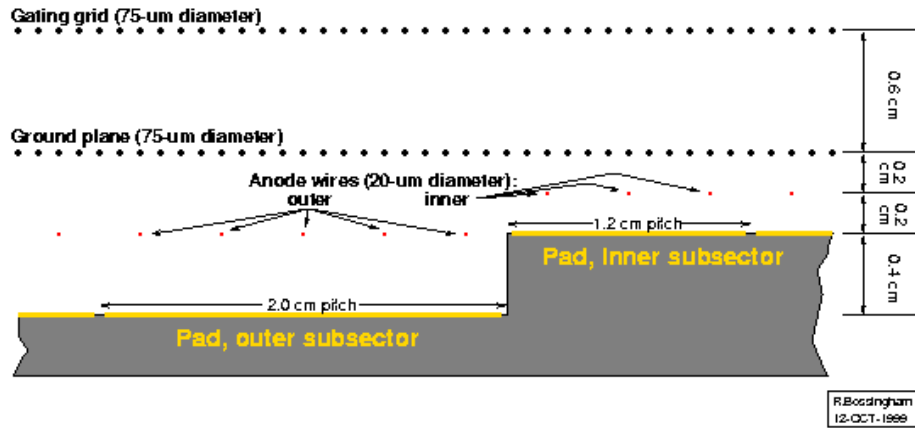


Figure 3.12: The Multi-Wire Proportional Chambers are composed of three wire planes and a pad plane connected to readout electronics.

in an avalanche effect.

Besides defining the drift field in the TPC, the gating and ground grids also perform other tasks.

The gating grid separates the drift volume from the amplification region. The grid controls the passage of ionization electrons coming into the amplification region. It also ensures that ions produced from electron avalanches do not drift from the amplification region into the drift volume, as this would cause a distortion in the drift field and lead to reduced position resolution. To keep wire aging effects at a minimum, STAR uses the gating grid to selectively read out certain events. This results in fewer electron avalanches and hence a longer lifetime for the MWPC.

The ground grid resides between the anode grid and the gating grid. This grid helps shield the pad plane and anode grid from noise effects due to

voltage switching of the gating grid. When the gating grid switches between open and closed states, a large instantaneous current is produced on the wires which is a source of noise in the MWPC. The ground grid also helps to define the anode wire avalanche cells.

Each end of the TPC has its readout plane broken into 12 sectors with each one further divided into inner and outer subsector (Figure 3.13). A sector is composed of are 13 inner subsector and 32 outer subsector cathode pad rows. Individual cathode pads measure  $2.85 \text{ mm} \times 11.5 \text{ mm}$  and  $6.2 \text{ mm} \times 19.5 \text{ mm}$  for inner and outer types, respectively. The size of the pads is limited by the space required for the TPC electronics on each end. The inner pads were chosen to provide good two-track resolution in the high track density region near the interaction vertex, whereas the outer pads fully cover the area beneath the anode wires to provide good  $dE/dx$  measurements for particle identification in the lower track density region. The  $1750 \times 24$  (inner) plus  $3942 \times 24$  (outer) pads per sector provide  $xy$  coordinate information for a cluster of ionization electrons, called a hit. Each pad also provides up to 512 time bins for a hit which, when converted to a distance measure via the drift velocity, gives  $z$ -position information in the TPC. This results in over 70 million pixels of possible information. Essentially, the STAR TPC can be thought of as a 70 megapixel 3D digital camera.

Table 3.3 shows some MWPC operating parameters from the first physics run.



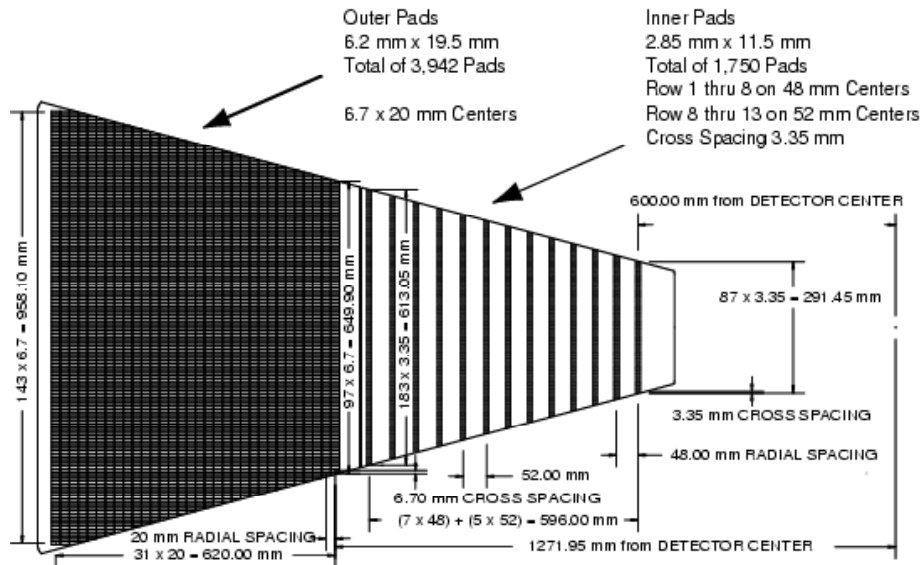


Figure 3.13: A TPC sector is made up of an inner and outer part.

| Anode Wire Voltages            |          |
|--------------------------------|----------|
| Inner Sector (V)               | 1170     |
| Outer Sector (V)               | 1390     |
| Gating Grid Wire Voltages      |          |
| Reference (V)                  | -127     |
| Wire Bias w.r.t. Reference (V) | $\pm 75$ |

Table 3.3: MWPC voltage settings for the year 2000 physics run [65].

### 3.4.3 Drift Gas

The drift gas is chosen based on several requirements including working at atmospheric pressure and exhibiting small transverse and longitudinal diffusion allowing for good two-track separation. Also, the gas must allow an electron drift velocity  $v_d > 2.0 \text{ cm}/\mu\text{s}$  at an electric field  $E < 300 \text{ V/cm}$ .

Secondary electrons from a primary track may drift in the TPC as much

as 2 m before reaching the anode plane. The gas must have a sufficiently small attenuation for these drifting electrons to get decent output signals. Oxygen and water act to attenuate the electron signals so the gas needs to be kept relatively pure. Oxygen concentrations of less than a few hundred parts per million allow this to be the case. In order to obtain this condition, the gas chosen must be easy to recirculate and clean. Noble and organic gases such as helium, methane, ethane, and isobutane are good candidates due to the ease of cleaning them with simple technologies.

Two gas mixtures were considered for use in the STAR detector: argon (90%)-methane (10%) (P10) and helium (50%)-ethane (50%). The noble gas component has a very low affinity for free electrons while the organic gas component quenches the propagation of UV photons throughout the TPC volume. The organic gas property is necessary to alleviate the destructive feedback effect where UV photons emitted from an avalanche could produce more photoelectrons via the photoelectric effect and hence more avalanches.

Based on tests done by STAR collaborators as well as previous work with TPCs in several AGS and SPS experiments (NA36, E810, NA35, EOS, ALEPH), P10 was chosen as the drift gas [44]. P10 is also less hazardous compared to the helium-ethane mixture as P10 does not require as high of an electric field to obtain an acceptable drift velocity. Furthermore, the diffusion of helium may damage other detector systems in STAR. The STAR TPC will continue to use P10 into the foreseeable future.

### 3.4.4 Drift Field

The applied electric and magnetic fields run parallel to the axis of the TPC. A charged particle passes through the active volume of the TPC, ionizing gas atoms along its path and creating a trail of electrons. The magnetic field causes charged particles to follow helical trajectories as they drift in the electric field. Oppositely charged particles curve in opposite directions and have transverse momenta calculated using Equation 3.1

$$p_{\perp} = 0.3qBR \quad (3.1)$$

where  $p_{\perp}$  is the transverse momentum,  $q$  is the charge,  $B$  is the magnetic field, and  $R$  is the radius of curvature for the particle.

The drift velocity of the ionization electrons is a function of the applied field as well as the composition of the gas. For accurate track measurements, a drift field corresponding to the peak of a drift curve as show in Figure 3.14 is optimal. Besides a maximized drift velocity, this chosen field ensures the drift velocity is least sensitive to minor changes in the gas pressure or temperature caused by the local environment. The STAR TPC monitors the drift velocity via ionization electrons from laser tracks and makes automated changes through a feedback loop. The origin of these tracks are well-known in space and time, so it is easy to calculate the drift velocity and apply corrections to the external field in order to compensate for any time-dependent variations in the gas properties.

The operating point for the drift velocity is actually slightly off-peak.

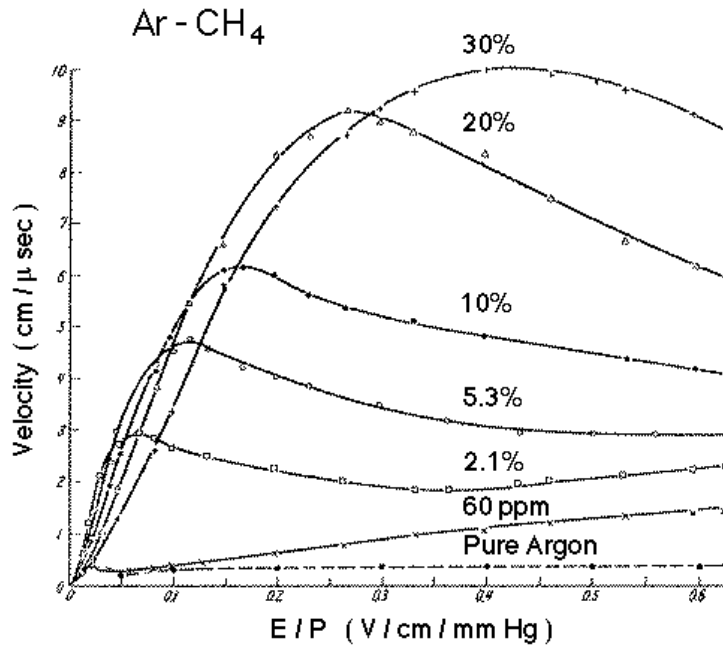


Figure 3.14: Drift curves for different  $Ar-CH_4$  mixtures. The STAR TPC uses a drift field of 148 V/cm.

This avoids measuring double-valued solutions when the drift velocity drops and also provides a slope to the observed changes in parameters. The drift velocity profile for P10 is given by the 10% curve in Figure 3.14. The curve shows that any reduced field greater than 0.16 V/cm/mm-Hg satisfies these conditions. In terms of standard temperature and pressure, the drift field should be slightly greater than 120 V/cm, which is why the TPC is operated at 148 V/cm.

### 3.4.5 TPC Readout

The readout of the TPC is performed by front end electronics (FEE) cards. There are 181 FEE cards per sector. A FEE card is basically composed of two types of chips. The first chip incorporates a pre-amplifier and shaper while the second chip contains a Switched Capacitor Array (SCA) and an Analog-to-Digital Converter (ADC). The SCA is made up of 512 capacitors that integrate the charge from each of the 512 time bins. The ADC then digitizes the signal from each capacitor by assigning it a value between 0 and 255 [54].

The digitized signals are sent to one of the 6 readout boards per sector. The TPC pixel occupancy is at most about 10% in an event, so there exists a large number of pixels that only contain noise. A pedestal run is taken previous to a physics run in order to remove the background caused by noise in the detector. A pedestal run is simply a record of the TPC noise when no collisions are being recorded. Each readout board uses a custom chip to move the data from the ADC to a buffer while subtracting the pedestal values. This process is called zero suppression and can reduce the data volume by up to a factor of 10. The readout boards also determine the location of charge clusters, but this information went unused during the year 2000 run. Instead, cluster finding was performed by the offline reconstruction chain (see §4).

The data from the each readout board are transferred in turn via communication with a global broker chip. The data are stored on buffer disks before being sent sequentially down a gigabit fiber link to permanent tape

media for offline access.

### 3.5 Event Triggering

Due to the limited data collection rate ( $\sim 11$  Hz) of the STAR detector and the thousands of beam crossings that occur each second, a set of trigger conditions exist to selectively record events of interest. The data presented in this analysis was collected using two particular conditions, minimum-bias and central triggers. The minimum-bias trigger required coincidence between both ZDCs while the central trigger additionally required a CTB threshold to be met. The central trigger was chosen to allow events that were in approximately the top 15% of the measured cross section for  $Au + Au$  collisions. The minimum-bias trigger allowed for a centrality scan of observables while the central trigger picked out events that were more likely to have produced QGPs.

#### 3.5.1 Trigger Detectors

For data taken during the summer of 2000, three trigger detectors were available (see Figure 3.15): the Multi-Wire Proportional Chambers (MWPCs), the Central Trigger Barrel (CTB), and the two Zero-Degree Calorimeters (ZDCs) common to all of the RHIC experiments. As mentioned above, only the CTB and the ZDCs were utilized for the first physics run period.

The MWPCs act as a charged particle multiplicity detectors for the pseudo-rapidity range  $1 < |\eta| < 2$ . Charged particles pass through the TPC

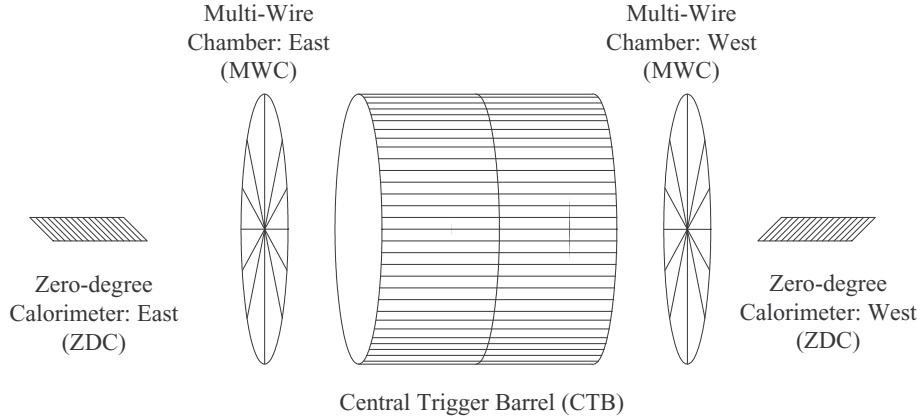


Figure 3.15: Year 2000 trigger detectors allowed for selection of interesting events. The MWPCs were not used during the physics run.

end-caps and therefore create signals on the anode wires. By themselves, the MWPCs leave a blank spot in the central pseudo-rapidity coverage.

The CTB fills in the gap with a coverage of  $|\eta| < 1$ . The CTB wraps around the TPC and so provides full azimuthal coverage. The length of the CTB corresponds to the TPC length of 4 m and allows for particle multiplicity measurements in the pseudo-rapidity range  $|\eta| < 1$ . The CTB consists of 240 scintillator slats arranged around the TPC. Each slat is viewed by 1 photomultiplier tube (PMT).

The ZDCs are small transverse hadronic calorimeters located  $\pm 18$  m from the nominal interaction vertex (0,0,0). They measure neutral energy within a 2 mrad cone about the beam direction. ZDCs provide a measure of centrality because of the strong correlation between it and the number

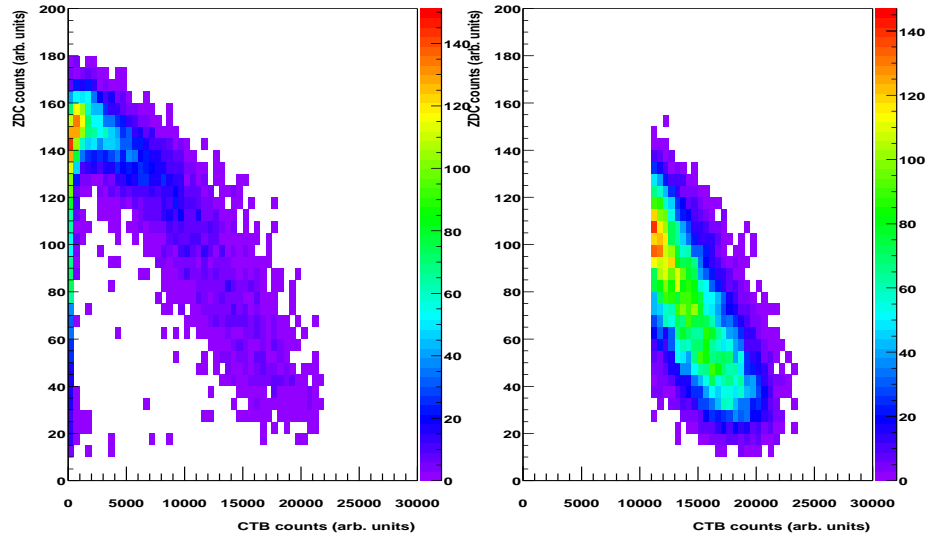


Figure 3.16: ZDC versus CTB signals for minimum-bias (left) and central triggers (right).

of spectator neutrons. Also, coincidence signals between the ZDCs act as luminosity monitors for RHIC. ZDCs, being common to all RHIC experiments, are then normalizing detectors for RHIC data.

Figure 3.16 shows how the CTB and ZDCs can be used to trigger on certain types of events. Higher CTB multiplicities correspond to lower ZDC signal, i.e., fewer spectator neutrons are measured. In the low CTB multiplicity region, the beam fragments are more stable. This means that neutron dissociation is less prominent and so a lower ZDC signal. The right-hand plot in Figure 3.16 shows the cut required for the year 2000 central trigger.



### 3.5.2 Trigger Levels

With the multitude of events arriving within a short period of time in the STAR detector, it is necessary to have what are essentially veto triggers to limit the amount of data kept. The veto trigger logic also acts to remove background events such as beam+gas interactions or beam+beam interactions that are far removed from the center of the detector.

The Level 0 trigger makes decisions based on information from the CTB and ZDCs for every bunch crossing (i.e., every 107 ns). The algorithms of this trigger generate  $\delta\eta \sim 0.8$  and  $\delta\phi \sim 1.0$  phase-space patches which are suitable for selecting events producing jets. Each detector channel is digitized for the individual RHIC crossings and fed into a Data Storage and Manipulation (DSM) board. The DSM analyzes and combines the input with other signals in a multi-layer pipeline that forms a fast decision tree [34]. The raw data from each detector are analyzed to determine if the requested interaction type occurred in the bunch crossing. Level 0 issues a trigger within  $1.5 \mu\text{s}$  of the interaction. If no signals of interest are seen, Level 0 can issue calibration triggers or it can simply wait for the next crossing.

The Level 1 analysis is performed during the TPC drift time of  $\sim 40 \mu\text{s}$ . The data input for this analysis are the output from the first layer of the DSM tree, known as the Course Pixel Array (CPA). The CPA is an  $8 \times 4, \eta - \phi$  digital sum from the CTB and MWPC detectors. The decision to accept an event for further processing at this level is based on the measured location of the primary vertex. This allows for rejection of events with interaction vertices

far removed from the center of the STAR detector. A time budget of  $\sim 100 \mu\text{s}$  exists for this level.

If the event has not been aborted by Level 0 or Level 1 analyses, then it is passed to Level 2. This analysis level uses the full trigger data set plus the digitized raw data from each detector as stored on the DSM boards, i.e., the Fine Pixel Array. Level 2 decisions have a window of  $\sim 5 \text{ ms}$  in which to be processed. Level 2 triggers were not fully used in year 2000 data collection due to a lack of processing power, and was not used to veto any events.

The final trigger logic, Level 3, collects data from the tracking detectors, reconstructs tracks, and makes decisions based on that information. Tracking allows for event selection on a finer scale than the previous trigger stages because it uses single particle information rather than global characteristics of the event. During the year 2000 run, Level 3 was used as a primary vertex  $z$ -position trigger for central events, selecting those events with  $|z| \leq 75 \text{ cm}$  [11].

# Chapter 4

## Reconstruction

The pixel information stored from the tracking detectors require distillation into the easily usable form of track information. Before tracks can be properly reconstructed though, a particle's hit positions need to be found. The hit positions are recorded during the software reconstruction chain by finding charge clusters in pad and drift time coordinates and converting them into position coordinates, in the case of the TPC. With the hits determined in this manner, pattern recognition software identifies tracks associated with said hits, and in doing so allows for the identification of the primary beam+beam interaction vertex for the event. The tracks revealed by this method belong to one of two classifications, primary or secondary. Primary tracks are those that originate from the primary vertex while secondary tracks are those that appear from secondary vertices. Consider the decay  $\Xi^- \rightarrow \Lambda\pi^-$  followed by the daughter  $\Lambda$  decay  $\Lambda \rightarrow p\pi^-$ . The decay products in each step create secondary tracks as they do not originate from the primary vertex. Before tracks can be tagged as primary or secondary though, they are all simply called global tracks. These tracks are then refit with the addition of the primary interaction point. The global tracks after the refit are flagged as primary tracks if they pass within 3 cm of the primary vertex. The global tracks which fail the

primary track selection criterion are used to reconstruct neutral strange particles ( $K_S^0, \Lambda, \bar{\Lambda}$ ) which are in turn used to reconstruct multi-strange particles ( $\Xi^-, \bar{\Xi}^+, \Omega^-, \bar{\Omega}^+$ ).

## 4.1 Corrections

As a charged particle traverses the TPC, it leaves behind an ionization trail of electrons. Ideally, these clumps of electrons drift and diffuse under the influence of parallel electric ( $\vec{E}$ ) and magnetic ( $\vec{B}$ ) fields. In practice though, it is seen that slight misalignments of the TPC and the magnet plus non-uniformity of the magnetic field results in slightly non-parallel  $\vec{E}$  and  $\vec{B}$  fields. As a consequence, the measured hit position may be shifted from the true position by as much as 1 mm. This shift is corrected for within the event reconstruction software chain. Other detector construction effects that are corrected for include non-uniformity of  $\vec{E}$  at the anode wires, a twist in the central membrane, and a small misalignment between inner and outer sectors.

While corrections can be applied for construction inaccuracies, there still exist resolution effects which limit the ability to identify particle properties correctly. The successful reconstruction of  $\Xi^-$  particles is affected by track momentum resolution and vertex position resolution. The position of the decay vertex needs to be accurate since many variables used to identify good  $\Xi^-$  candidates utilize the distance of closest approach of a track to the vertex. The invariant mass peak widths of §5.2 are much wider than the line width of the  $\Xi^-$  due a combination of these two finite resolutions.

## 4.2 Year 2000 Triggers

The data used in this analysis was taken with two different trigger conditions, one for minimum-bias events and one for central events. The minimum-bias trigger required coincidence in the two ZDC signals whereas the central trigger had the additional requirement of meeting a particular energy threshold in the CTB. Events selected by the minimum-bias trigger accounted for approximately 95% of the total geometric cross-section of the collision. The central trigger corresponded to approximately the top 15% of the measured  $Au + Au$  cross section. STAR recorded approximately 761,000 minimum-bias and 884,000 central events in the year 2000 physics run.

## 4.3 Event Selection

Knowing the primary vertex position accurately is important when distinguishing between tracks originating from the primary vertex and those from weak decays or other interactions. The year 2000  $Au + Au$  interactions were not well tuned and so resulted in the reconstruction of primary vertices over the full 4 m range in  $z$  for STAR, as seen in Figure 4.1. Events reconstructed far from the TPC's central membrane (defined as  $z = 0$ ) have lopsided pseudorapidity distributions, introducing biases in the analysis. To ensure the least amount of asymmetric events are included, a cut on the primary vertex  $z$  position is applied so that good events have  $|z| < 75$  cm.

To enable the investigation of  $\Xi^-$  production as a function of event centrality, some event centrality classes must be defined. This is done by

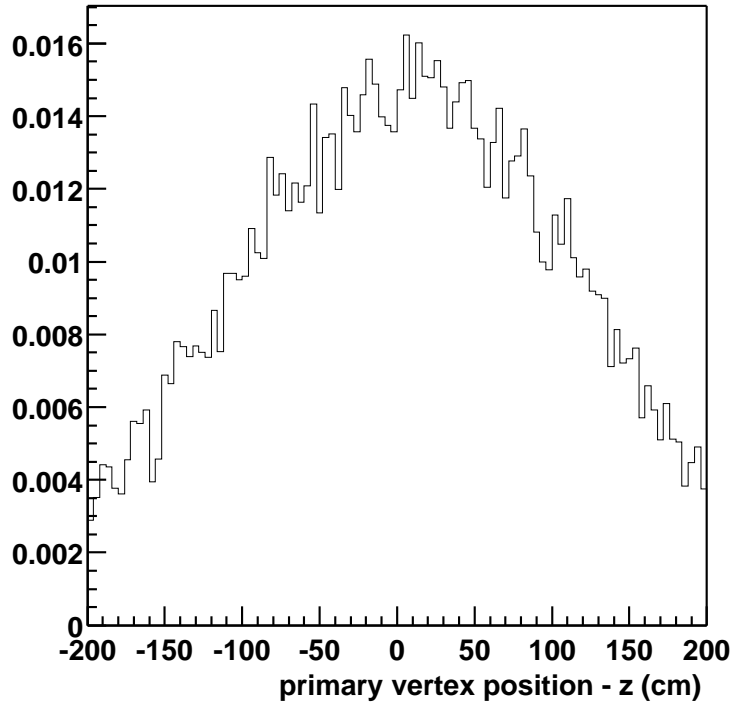


Figure 4.1: Primary vertex  $z$  distribution ranges over the full STAR TPC 4 m length.

examining the negatively charged TPC tracks with a pseudo-rapidity  $|\eta| < 0.5$  and transverse momentum  $p_{\perp} > 100$  MeV/ $c$ . The multiplicity distribution of such particles is seen in Figure 4.2. The raw multiplicity is converted into a corrected number of negative hadrons  $h^{-}$  which is then used to determine the corresponding fraction of the total hadronic cross section  $\sigma_h$  [3]. Negative hadrons are commonly used as a reference as all negative particles are produced only from the collision. Table 4.1 lists the three centrality classes used in this analysis. Bin I represents the 10% most central portion of the total hadronic cross-section. For this analysis, Bin I events are chosen from the central trigger

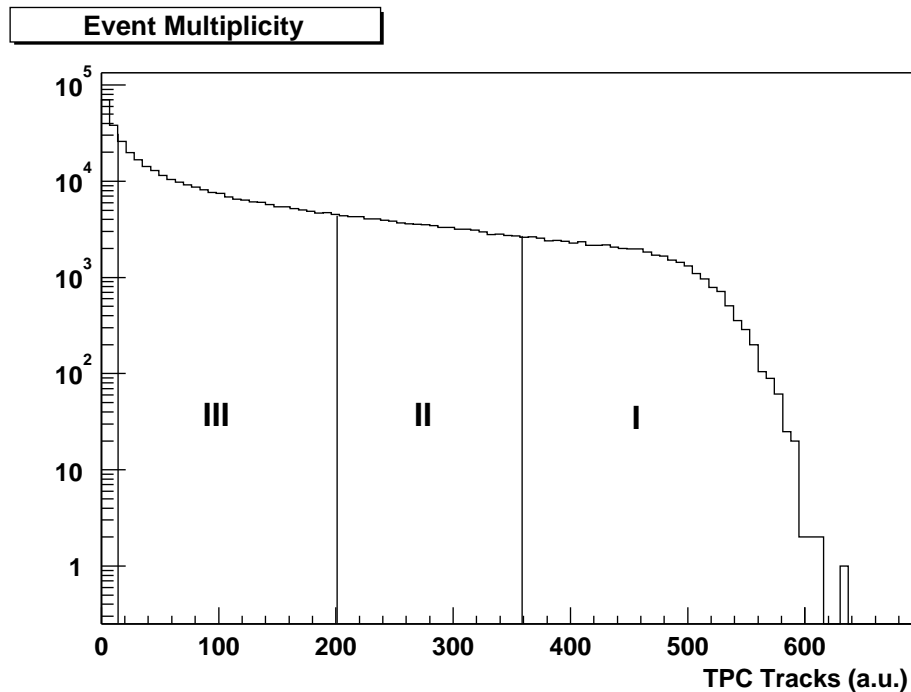


Figure 4.2: Centrality class definitions. The most central events are sampled from region I while the most peripheral events are taken from region III.

pool of events, while events for Bins II and III are taken from the minimum-bias trigger events.

#### 4.4 $\Xi$ Search

The primary decay channel  $\Xi^- \rightarrow \Lambda p$  has a 99.9% branching ratio. The daughter  $\Lambda$  further decays  $\Lambda \rightarrow p\pi^-$  with a 63.9% branching ratio. As the charged final state daughters from the original  $\Xi^-$  pass through the TPC they ionize the TPC gas (P10) and so leave a trail of electrons floating behind them. The electric field drifts the electrons to the anodes to produce hits, as

| Centrality Bins |                        |                           |                  |
|-----------------|------------------------|---------------------------|------------------|
| Centrality Bin  | Fraction of $\sigma_h$ | $\langle N_{h^-} \rangle$ | Number of Events |
| I               | 0% $\rightarrow$ 10%   | $270.6 \pm 6.5$           | 332,489          |
| II              | 10% $\rightarrow$ 25%  | $165.2 \pm 5.5$           | 44,988           |
| III             | 25% $\rightarrow$ 75%  | $45.0 \pm 3.6$            | 128,682          |

Table 4.1: Centrality bins used for this analysis.  $\langle N_{h^-} \rangle$  is the mean number of negative hadrons.

described in §3.4. Beyond reconstructing the tracks themselves,  $\Xi^-$ s are found by tracing the decay topology backwards. First, a neutral decay vertex is found by identifying crossing points of positive and negative particles' tracks. Kinematic information about the tracks are used to determine the trajectory of the parent neutral particle. This neutral particle is then intersected with other negative tracks to give candidate  $\Xi^-$  decay vertices. A schematic diagram of a  $\Xi^-$  decay is given in Figure 4.3.

Each high energy  $Au + Au$  event produces up to several thousand particles. Finite momentum resolution of the TPC causes primary tracks to not point back exactly to the primary vertex. As a result, these tracks may randomly cross with other primary tracks and form fake secondary vertices. Indeed, in the quagmire of particle tracks, it is quite easy for misidentification of vertices, leading to a large combinatoric background. To reduce this background without affecting individual analyses, basic cuts are applied during the event reconstruction chain.

To determine if two tracks originated from the same vertex, a cut is placed on their distance of closest approach (DCA). This cut reduces the ran-



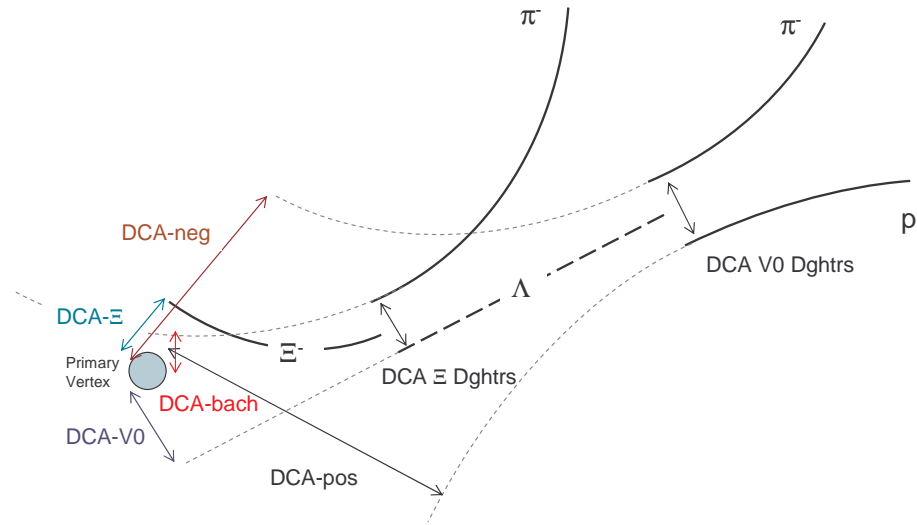


Figure 4.3: Schematic representation of a  $\Xi^-$  decay with distance of closest approach (DCA) parameters.

dom background by a large amount, but is not sufficient to guarantee good identification of the parent particle. Other cuts are necessary (see Table 4.2):

- Due to the high density of tracks near the primary vertex, it is quite easy to form many fake track crossings. This leads to a larger combinatoric background the closer one gets to the primary vertex. The decay distance distribution has an exponential fall-off from zero, so a cut on this distance for the candidate  $\Xi^-$  and daughter  $\Lambda$  greater than 2 cm and 5 cm, respectively, is used. The decay distances are measured from the primary vertex.
- The candidate parent  $\Xi^-$  points back to the primary vertex since heavier particles are produced near there.

| Basic Reconstruction Cuts   |                         |
|-----------------------------|-------------------------|
| Cut Type                    | Value                   |
| Decay Distance, $\Xi$       | $> 2$ cm                |
| Decay Distance, V0          | $> 5$ cm                |
| DCA $\Xi$ to Primary Vertex | $< 0.8$ cm              |
| DCA $\Xi$ Daughters         | $< 0.8$ cm              |
| DCA V0 Daughters            | $< 0.8$ cm              |
| V0 Mass                     | PDB $\pm 10$ MeV/ $c^2$ |

Table 4.2: Some basic reconstruction cuts. Here, V0 refers to the candidate (anti-)lambda and  $\Xi$  represents the candidate charged (anti-)cascade. Decay distances are measured from the primary vertex. The Particle Data Book [49] value for  $\Lambda$  mass is 1.116 GeV/ $c^2$ .

- The daughter tracks do not point back to the primary vertex to ensure they are not primary tracks.
- A cut on the calculated mass of the daughter neutral particle is done to increase the likelihood that the parent particle did indeed decay into a  $\Lambda$  ( $\bar{\Lambda}$ ) plus a charged track.

After the event reconstruction chain is complete, all the track and vertex data are stored in Data Summary Tapes (DSTs). These DST files are collections of C++ classes and are quite large, requiring a large amount of time to process in later stages. To reduce the processing time to something more manageable, so-called micro-DSTs are produced. Each physics working group has their own code to produce micro-DSTs, which store just the essential data for their analyses. The Strangeness Working Group's (SWG) micro-DSTs contain secondary vertices and the tracks linked to them. They also contain

| Filter Cuts                           |                                    |
|---------------------------------------|------------------------------------|
| Cut Type                              | Value                              |
| DCA $\Xi$ to Primary Vertex           | $< 0.6$ cm                         |
| DCA $\Xi$ Daughters                   | $< 0.7$ cm                         |
| DCA V0 Daughters                      | $< 0.7$ cm                         |
| V0 Mass                               | $\text{PDB} \pm 7 \text{ MeV}/c^2$ |
| TPC Hits, Final State Particles       | $> 9$                              |
| PID Efficiency, Final State Particles | $> 5\sigma$                        |

Table 4.3: Filter cuts applied in addition to the basic reconstruction cuts of Table 4.2. PID is discussed in §5.

some basic event conditions, such as each event’s primary vertex position and the number of global and primary tracks. This reduces the disk space usage by a factor of 10 or more and also significantly decreases the processing time for individual analyses. Also, to aid analyses, some often used quantities are calculated and stored in the micro-DSTs or have methods which can calculate them on the fly contained within the accessing software package.

The SWG’s micro-DSTs store information for several types of decay topologies including V0, kink, and  $\Xi$  decays. The V0 decay topology describes the decay of a neutral parent particle into two charged daughters, such as in the case of  $\Lambda \rightarrow p\pi^-$ . Kinks refer to processes such as  $K^+ \rightarrow \mu^+\nu_\mu$ , where the charged parent’s track in the TPC appears to bend sharply at the decay vertex since the neutral daughter does not leave a trail. Finally, the  $\Xi$  decay topology covers both  $\Xi^- \rightarrow \Lambda\pi^-$  and  $\Omega^- \rightarrow \Lambda K^-$  decays, such as that seen in Figure 4.3. A significant percentage of the final file size is due to storing the V0 and  $\Xi$  candidates. Further culling of the data can occur beyond the

micro-DST production stage. For the results presented here, the Strangeness Working Group's micro-DSTs are filtered into personal nano-DSTs using a slightly tighter selection of reconstruction cuts, listed in Table 4.3. The smaller file size of the nano-DSTs translates to less CPU time required to analyze the data. The analysis code then reads these nano-DSTs and applies the final analysis cuts, which are discussed in §5.

## Chapter 5

### Analysis

The primary goal of this analysis is to determine quantities which add to understanding the underlying  $\Xi^-$  production mechanisms as discussed in 2.6. Hence, the  $\bar{\Xi}^+/\Xi^-$ ,  $\Xi^-/\pi^-$ , and  $\Xi^-/h^-$  ratios are examined, as well as the average  $\Xi^-$  and  $\bar{\Xi}^+$  yields as functions of rapidity ( $y$ ), transverse momentum ( $p_\perp$ ) or mass ( $m_\perp$ ), and event centrality. These quantities offer useful information on the baryon stopping achieved in the collisions as well as the relative amount of strangeness production present.

Before STAR began taking data, the idea of reconstructing significant signals for multi-strange baryons seemed unlikely since reducing the combinatoric background enough to see a peak was expected to be a rather formidable hurdle to overcome. Within a short amount of time since the start of the data processing though, not only did strong  $\Xi^-$  and  $\bar{\Xi}^+$  peaks become visible (see §5.2), but  $\Omega^-$  and  $\bar{\Omega}^+$  became a distinct possibility from year 2000 physics data. In fact, the STAR analyses have matured to the stage of presenting multi-strange particle ratios and spectra to the public [9, 10].

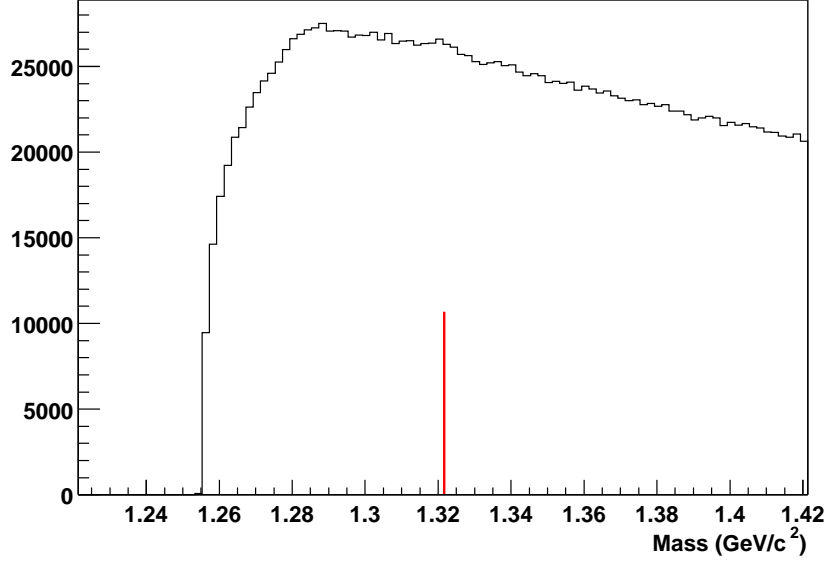


Figure 5.1: Combined  $\Xi^- + \bar{\Xi}^+$  invariant mass histogram from 83k central-trigger events using basic reconstruction cuts. The red line indicates the expected PDB mass.

## 5.1 $\Xi$ Identification

Obtaining the signals used to extract the quantities of interest is done by examining the  $\Xi^-$  and  $\bar{\Xi}^+$  invariant mass spectra. The invariant mass is obtained by applying conservation of energy and momentum in the decay process as given in Equation 5.1,

$$m_{parent}^2 = m_1^2 + m_2^2 + 2(E_1 E_2 - \vec{p}_1 \cdot \vec{p}_2) \quad (5.1)$$

where the energy is given by

$$E^2 = m^2 + \vec{p}^2 \quad (5.2)$$

in units  $c = 1$ . Equation 5.1 is used twice since there are two decays associated with the  $\Xi^-$  particle. The charge sign of the bachelor track determines the mass hypothesis invoked for the daughter particles. A negative sign implies the decay is from a  $\Xi^-$  whereas a positive sign implies the decay proceeded from a  $\Xi^+$ . This is important at the V0 parent reconstruction stage because the sign determines which mass hypothesis to apply to the positive (negative) daughter since it may be either a proton or a  $\pi^+$  ( $\pi^-$  or anti-proton). The mass hypothesis used affects the energy term when calculating the V0 parent mass. Once it is determined whether the V0 parent is a  $\Lambda$  or an  $\bar{\Lambda}$ , the energy and momentum is passed onto the next step.

The second application of the mass calculation requires the use of another mass hypothesis, this time on the bachelor. The  $\Omega^-$  has the highest strangeness content of any baryon and decays with the same topology as the  $\Xi^-$ . The higher mass of the  $\Omega^-$  allows for  $\Omega^- \rightarrow K^- \Lambda$  to be the dominant decay mode with a branching ratio of 67.8% [49]. As this analysis concentrates on  $\Xi^-$  and  $\Xi^+$  particles, the mass hypothesis applied to the bachelor track is that of a pion. Figure 5.1 shows the invariant mass distribution after the basic set of reconstruction cuts have been applied and before the final analysis cuts.

Figure 5.1 shows that the basic set of reconstruction cuts is insufficient for identifying good cascades. The cuts require tuning to obtain clean signals. One way to estimate cut values is by plotting one cut variable versus another, as in Figures 5.2 and 5.3. Good candidates are obtained by the criteria listed in Table 5.1 which are detailed below.

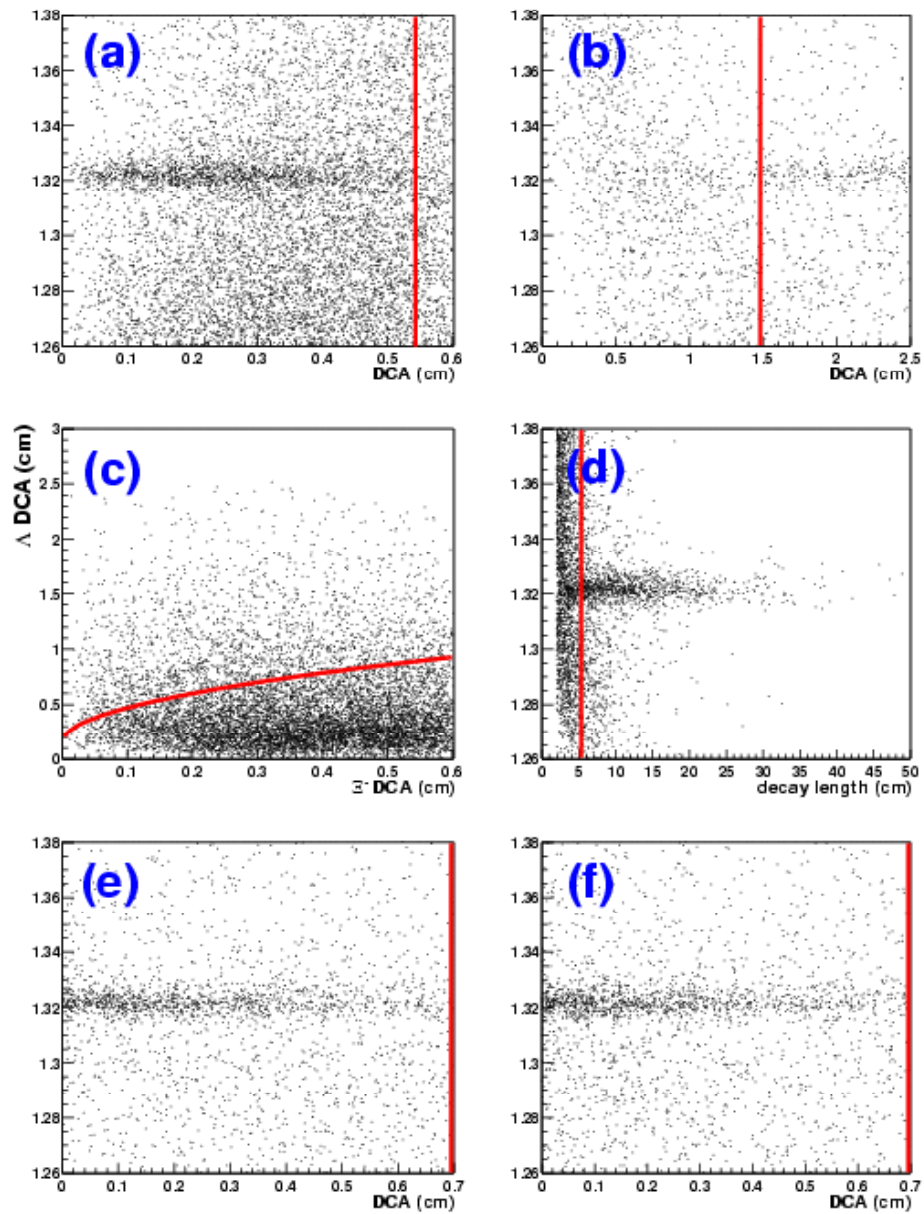


Figure 5.2: Variable versus variable cuts. The red lines represent the final cut values. The histograms are  $\Xi^-$  mass versus (a) DCA  $\Xi^-$  to the primary vertex, (PV) (b) DCA bachelor to the PV, (d)  $\Xi^-$  decay length (e) DCA between  $\Xi^-$  daughters, and (f) DCA between  $\Lambda$  daughters. Histogram (c) is DCA  $\Lambda$  to the PV versus DCA  $\Xi^-$  to the PV.



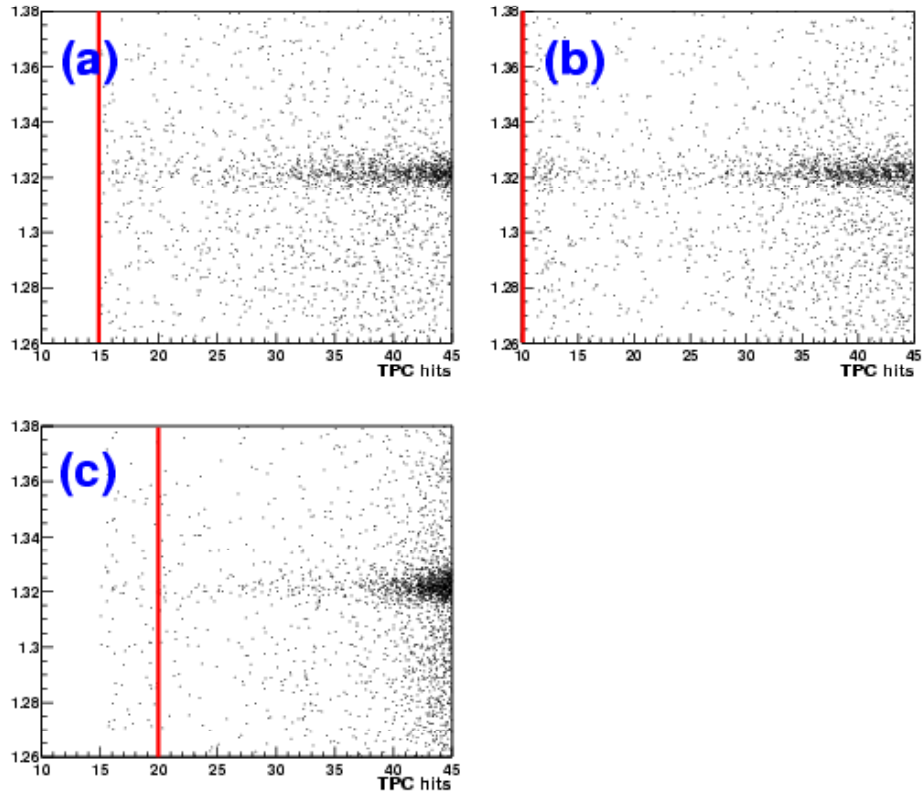


Figure 5.3: More variable versus variable cuts. The red lines represent the final cut values. The histograms are  $\Xi^-$  mass versus (a) number of bachelor TPC hits, (b) number of  $\Lambda$  meson daughter TPC hits, and (c) number of  $\Lambda$  baryon daughter TPC hits.

Reconstructed tracks are required to have at least 15 hits in the TPC to eliminate split track contributions. Split tracks are actually from one track that contains gaps in the spatial hit distribution. These gaps cause the software to incorrectly identify several tracks instead of the single track and so can lead to a larger background.

The variables used in the cuts are not necessarily independent of each

| Final Analysis Cuts |                                      |                               |
|---------------------|--------------------------------------|-------------------------------|
| Cut Variables       | Centrality Bin I                     | Centrality Bins II, III       |
| Decay Distance V0   | $> 5$ cm                             | same                          |
| Decay Length $\Xi$  | $> 5$ cm                             | $> 4$ cm                      |
| DCA $\Xi$ to PV     | $< 0.55$ cm                          | same                          |
| DCA V0, $\Xi$ to PV | $DCA_{V0} > \sqrt{DCA_{\Xi}} + 0.15$ | $DCA_{V0} > \sqrt{DCA_{\Xi}}$ |
| DCA $\Xi$ Daughters | $< 0.7$ cm                           | same                          |
| DCA V0 Daughters    | $< 0.7$ cm                           | same                          |
| DCA Bachelor to PV  | $> 1.5$ cm                           | $> 1.0$ cm                    |
| V0 Mass             | $PDB \pm 7$ MeV/c <sup>2</sup>       | same                          |
| Rapidity $\Xi$      | $ y  < 0.75$                         | same                          |
| $\Xi p_{\perp}$     | $0.5 < p_{\perp} < 3.5$ GeV/c        | same                          |
| TPC Hits, Bachelor  | $> 14$                               | same                          |
| TPC Hits, Meson     | $> 10$                               | same                          |
| TPC Hits, Baryon    | $> 20$                               | $> 14$                        |
| PID Efficiency      | $< 3\sigma$                          | same                          |

Table 5.1: Final analysis cuts for extracting useful invariant mass spectra for the centrality bins examined. Decay distance is measured from the primary vertex. Decay length is the linear distance from the point of origin ( $\Xi$  vertex in the case of the V0 parent track) and the decay vertex. The decay length is the same as the decay distance for the  $\Xi$  particles. PV = Primary Vertex.

other. Indeed, there are correlations between them such as with the DCA to the primary vertex for the candidate  $\Xi^-$  and daughter  $\Lambda$ . Two more variables exhibiting a strong correlation are the decay lengths of the  $\Xi^-$  and the  $\Lambda$ . The majority of the background is seen to lie in particular regions and so leads to corresponding cuts. The choice for this analysis is to utilize simple linear cuts.

Kinematic cuts are also required. Figure 5.4 displays the phase-space coverage, or acceptance, for  $\Xi^-$ . The rapidity cut of  $|y| < 0.75$  is applied to the candidate charged  $\Xi$ s to help remove acceptance effects and is sufficient to select the majority of the candidates. The transverse momentum cut of

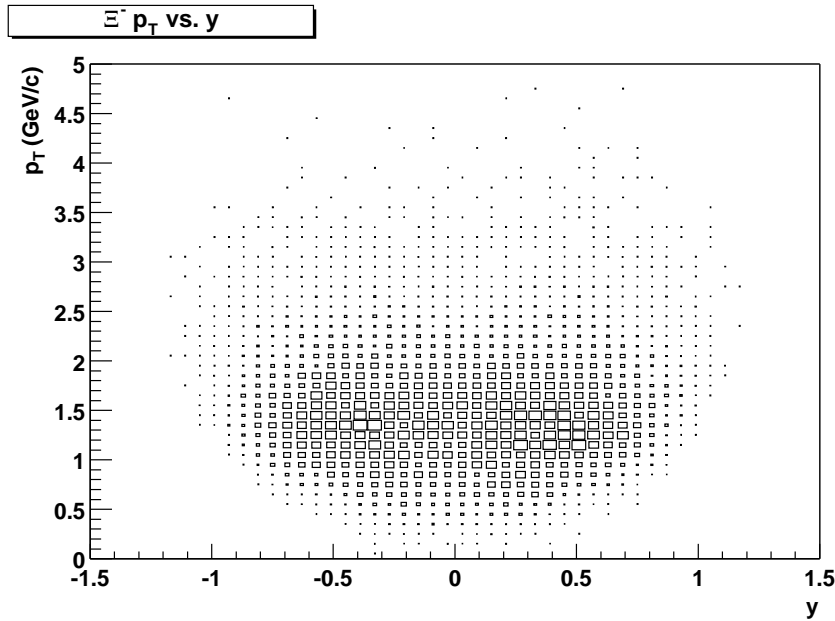


Figure 5.4: Phase-space coverage for reconstructed  $\Xi^-$  particles in terms of transverse momentum and rapidity. Larger boxes equate to more entries.

$0.5 < p_{\perp} < 3.5$  GeV/c is motivated by the amplitude of the signal seen when sliced into  $p_{\perp}$  bins. Below 0.5 GeV/c, the signal is found to be essentially nonexistent when compared to the background, the background being much larger at lower momenta than at higher values. Above 3.5 GeV/c, the signal is found to be on the order of a few counts which contributes a negligible amount to this analysis. Cutting at this upper value then reduces the number of calculations needed which means a reduction in the computation time with only a small loss in signal.

Particle identification is done by investigating the correlation between the ionization energy loss ( $dE/dx$ ) of charged particles passing in the TPC gas

and their measured momenta. The energy loss is given by the Bethe-Bloch formula

$$-\frac{dE}{dx} = 4\pi N_0 r_e^2 m_e c^2 \frac{Z}{A} \rho \frac{1}{\beta^2} z^2 \left[ \ln \left( \frac{2m_e c^2}{I} \beta^2 \gamma^2 \right) - \beta^2 - \frac{\delta}{2} \right] \quad (5.3)$$

where  $N_0$  is the Avogadro number,  $r_e (= \frac{e^2}{m_e})$  is the classical electron radius, and  $\rho$ ,  $Z$ , and  $A$  are the medium's density, atomic number, and mass number respectively.  $I$  is the ionization potential of the medium,  $z$  is the charge of the particle traversing the medium, and  $\delta$  parameterizes a "density effect" of the medium which describes the saturation of the energy loss at highly relativistic velocities [47, 57]. Also,  $\beta = v/c$  and  $\gamma = 1/(1 - \beta^2)$ . While Equation 5.3 does not explicitly depend on the mass of the particle traversing the medium, it can be shown that  $\beta\gamma = p/mc$  where  $p$  and  $m$  are the mass momentum and mass of the particle. This means that specific ionization energy losses of different mass particles are separated from each other when examined at the same momentum. Figure 5.5 shows the energy loss bands for various particles as functions of momentum.

To use specific ionization energy loss as a cut to reduce the background, it is necessary to determine the mean energy loss for a track as well as how far from the expected value the mean is. The energy deposited per unit length in the TPC, which is assumed to be equivalent to the energy lost per unit length, has a Landau distribution. In order to obtain a valid mean, the high energy tail of the distribution needs to be removed so that the rest of can be fit with a Gaussian. For this analysis, the largest 30% of the  $dE/dx$  values

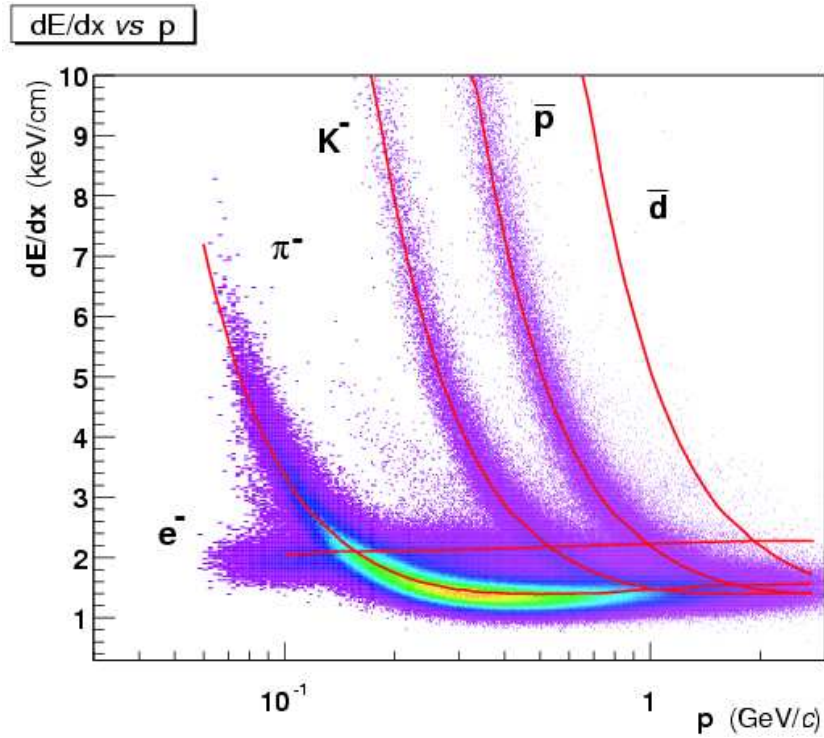


Figure 5.5:  $dE/dx$  versus momentum for reconstructed negative tracks in the TPC. The red curves are the expected energy loss curves for the given particle types.

for a track are cut to calculate the mean  $\langle dE/dx \rangle$ . Tracks within  $3\sigma$  of the expected Bethe-Bloch curve are kept. The cut is applied to the three charged final state particles of the  $\Xi^-$  decay process. This reduces the combinatoric background with little to no effect on the real signal.

All the above cuts conspire together to form invariant mass plots as in the next section. While the background is not completely eliminated, it is important to not tighten the cuts too far or else the analysis would become even more statistically limited than it already is. The  $\Xi^-$  with its high mass

is produced in small quantities, implying the need for as much statistics as reasonable to glean useful spectra.

## 5.2 Raw Particle Yields

Obtaining the raw particle yields is done by determining the number of counts in the mass peaks. This can be done by fitting the peak to some functional form and integrating or by simply summing the counts in the peak. However, as there are still background counts to contend with, a subtraction process must also be enacted. Several methods of identifying and removing the background shape under the mass peaks are explored including fitting the background to a polynomial and by summing entries outside of the peak.

### 5.2.1 Peak Fitting

The first functional form used to attempt to extract signals was a Breit-Wigner distribution on a polynomial background,

$$f(x) = A_p \frac{\Gamma/2\pi}{(x - \mu)^2 + (\Gamma/2)^2} + \textit{polynomial} \quad (5.4)$$

where the peak amplitude  $A_p$ , the full width at half maximum (FWHM)  $\Gamma$ , the peak mean  $\mu$ , and the coefficients of the polynomial were left as fit parameters. Polynomials from order one to order three were used to determine the best background parameterization. It was observed that this form tended to overestimate the peak amplitude and the peak tails. In the end, this method was not chosen for the final analysis. An example is given in Figure 5.6.

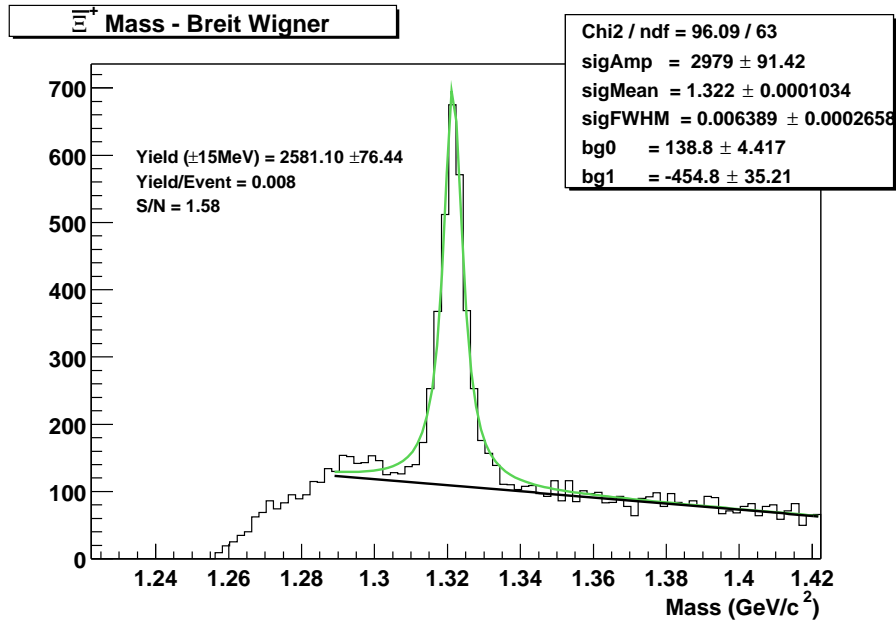


Figure 5.6: Signal extraction via a Breit-Wigner distribution. The background was parameterized by a straight line for the peak fits. Data is from 140,000 of the 10% most central events.

The width of the  $\Xi^-$  mass peak is dominated by experimental resolution effects which depend on factors such as the momentum of the three final state particles. Resolution effects from the TPC are Gaussian in nature and so the final  $\Xi^-$  mass distribution is most likely described by the convolution of many Gaussians. This led to the next fit choice of a Gaussian,

$$f(x) = Ae^{-(x-\mu)^2/2\sigma^2} + \text{polynomial}. \quad (5.5)$$

Here  $A$ ,  $\mu$ , the standard deviation  $\sigma$ , and the coefficients of the polynomial were left as fit parameters. While the peak tails were better described by a Gaussian, this method tended to underestimate the signal peak and so was likewise not chosen for the final analysis. An example is given in Figure 5.7.

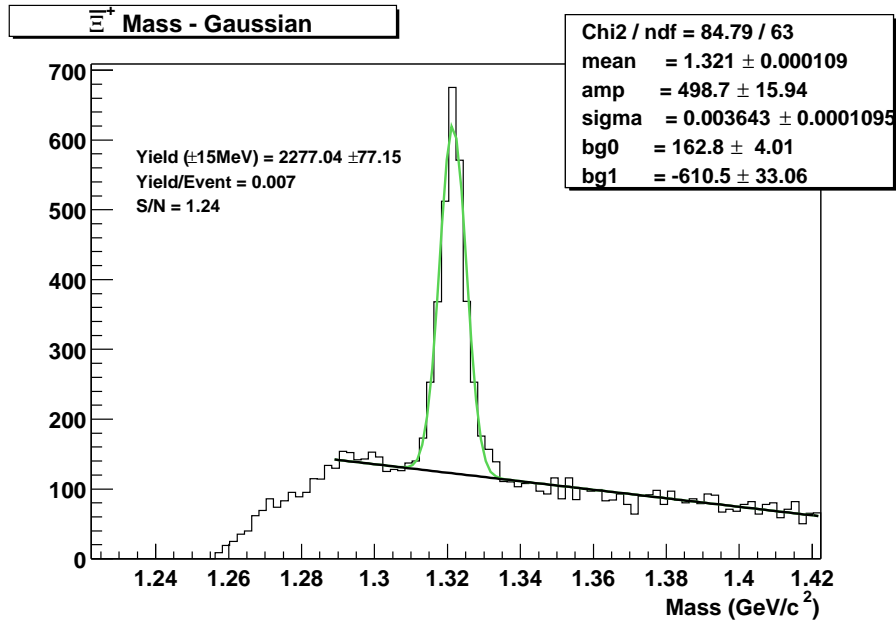


Figure 5.7: Signal extraction via a Gaussian distribution. The background was parameterized by a straight line for the peak fits. Data is from 140,000 of the 10% most central events.

To see if multiple Gaussians would better describe the data, an attempt was also undertaken to utilize a double-Gaussian form of the fit function,

$$f(x) = A_1 e^{-(x-\mu)^2/2\sigma_1^2} + A_2 e^{-(x-\mu)^2/2\sigma_2^2} + \text{polynomial} \quad (5.6)$$

where  $\mu$  is the common mean for each single Gaussian function. While this form did describe the data better than the single-Gaussian fit, it tended to fail for data bins  $(m_{\perp}, y)$  with few entries and so was also removed from consideration for extracting the signal. In fact, this was a problem for the other fit functions as well. An example of this method is seen in Figure 5.8.

As stated earlier, another way to obtain the signal is through simply



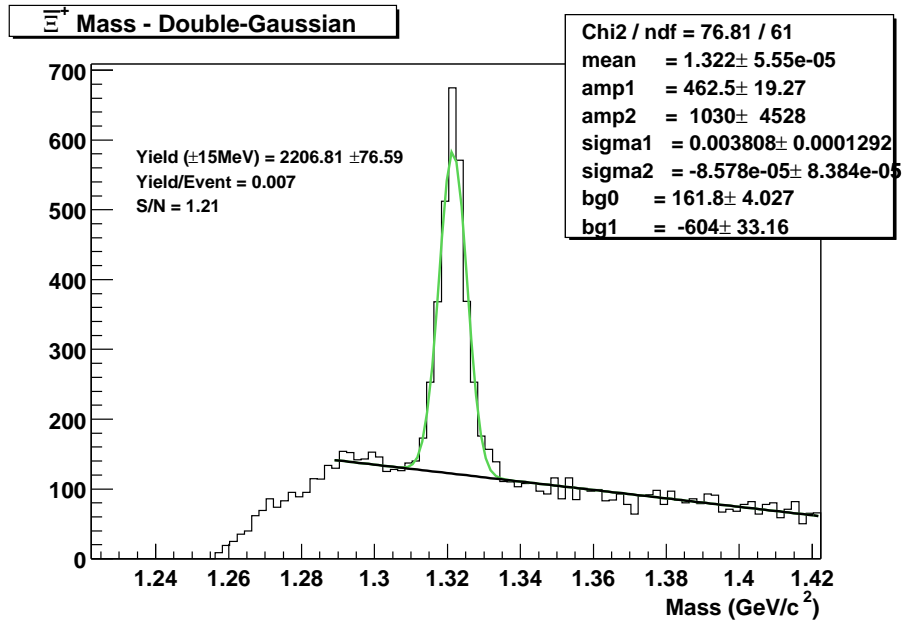


Figure 5.8: Signal extraction via a double-Gaussian distribution. The background was parameterized by a straight line for the peak fits. Data is from 140,000 of the 10% most central events.

summing the number of counts in the peak. However, the background counts under the signal is non-negligible and so must be eliminated. The two methods attempted are done by summing the peak and fitting the background, and by summing the peak as well as the background.

## 5.2.2 Background Fitting

Fitting to the background around the mass peak and simply summing peak entries provides a way to extract the signal without worrying about how the final distribution shape depends on resolution effects. Data points are taken from bins ranging outside of the mass peak and an interpolation is done

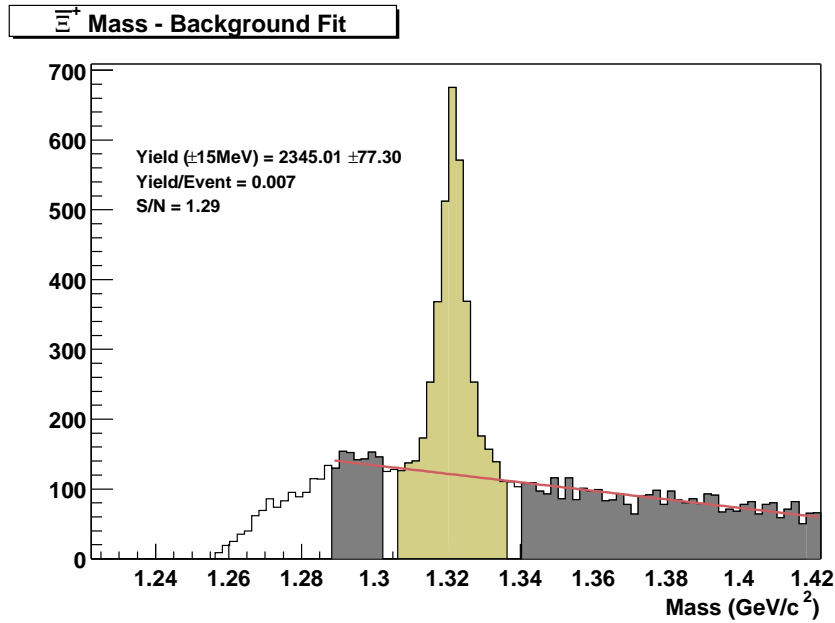


Figure 5.9: Signal extraction via a linear background fit. The background data points were taken from the gray shaded regions outside of the mass peak. An interpolation is done to acquire the background level underneath the mass peak. Data is from 140,000 of the 10% most central events.

to acquire the shape of the background underneath the peak. This is referred to as the Background Fit Method (BFM).

This method was utilized with a peak mass range of  $\pm 15 \text{ MeV}/c^2$  about the Particle Data Book  $\Xi^-$  mass [49]. Figure 5.9 shows an example. The shaded regions about the mass peak represents where the background data points were taken from. The signal was found by taking the area under the line within the mass peak range and subtracting that from the total number of entries (represented by the gold color).

### 5.2.3 Bin Counting

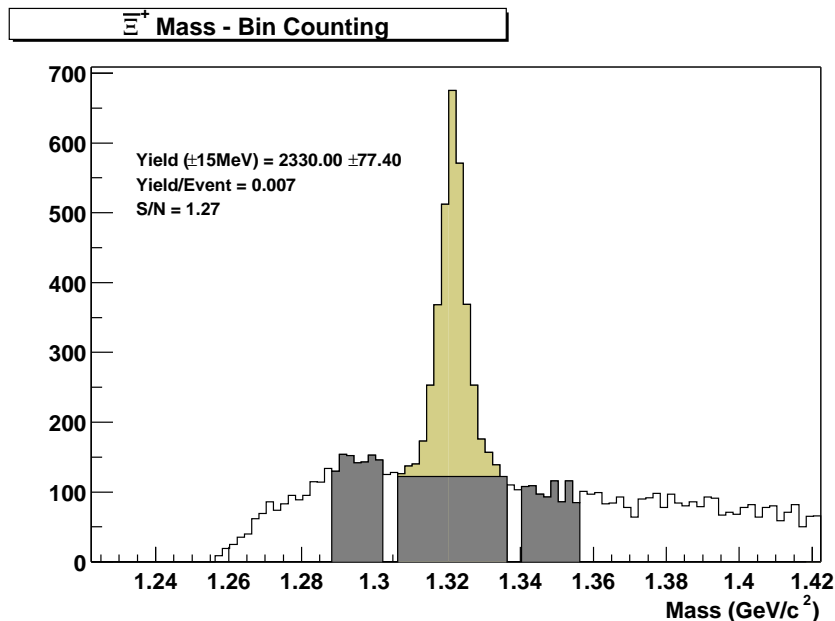


Figure 5.10: Signal extraction via a simple bin counting. The shaded regions on either side of the mass peak are the sources for the background seen below the signal peak. Data is from 140,000 of the 10% most central events.

The chosen signal extraction method for this analysis uses simple bin counting for both the peak and the background. As long as the background is linear, it can be determined by subtracting the background values from either side of the signal peak such that the range chosen for counting the peak entries is matched by the total range of the chosen background bins. The choice of cuts for producing the final invariant mass histograms are such that linear backgrounds exist under the peaks, making this method valid. This method, referred to as the Bin Counting Method (BCM) is not prone to failure when statistics are lacking in a data bin unlike the signal extraction methods

mentioned earlier.

The raw yield was extracted by summing entries within  $\pm 15 \text{ MeV}/c^2$  about the Particle Data Book mass. Using the data book value for the  $\Xi^-$  mass is valid as seen from the earlier peak fitting results, where the reconstructed mass peaks are centered around  $1.321 \text{ GeV}/c^2$ . Due to the use of  $2 \text{ MeV}/c^2$  bin sizes for the invariant mass histograms, the background counting was done by selecting a region on each side of the mass peak with nearly equal widths of  $14 \text{ MeV}/c^2$  and  $16 \text{ MeV}/c^2$ . Figure 5.10 provides an example of this method.

### 5.3 Embedding Process

The measured raw yields do not equal the total number of  $\Xi^-$  and  $\bar{\Xi}^+$  particles produced in the collisions due to acceptance and reconstruction effects which act to diminish the number of directly observable particles. Correction factors are required to determine the absolute yields from the raw data. These factors describe the efficiency of the analysis in identifying real  $\Xi^-$  ( $\bar{\Xi}^+$ ) particles and are found using simulations based on Monte Carlo techniques.

Monte Carlo particles for this analysis were first generated within a rapidity window of  $|y| < 1.2$  and a transverse momentum window of  $0.3 < p_{\perp} < 4.0 \text{ GeV}/c$ . The distribution of generated particles followed that of Equation 2.12 with a set inverse slope parameter  $T = 350 \text{ MeV}$ . The generated particles were then embedded into real events with a multiplicity of 6% of the raw data. The embedding multiplicity was chosen so that the overall event multiplicity did not change too greatly. Too large a difference in the event multiplicity

before and after embedding would affect the analysis by artificially altering the effect of the multiplicity-based centrality cut.

The generated particles are processed through a simulation of the detector using the GEANT [41] package. GEANT is a tool which allows the modelling of detector material and how particles interact with each other as well as with the material they are propagated through. For this analysis,  $\Xi^- \rightarrow \Lambda\pi^-$  and  $\Lambda \rightarrow p\pi^-$  are taken to occur 100% of the time. This allows for fewer Monte Carlo particles that need to be embedded, saving valuable CPU time, but at the cost of requiring a branching ratios correction factor when calculating the efficiency.

Once the GEANT software is done with the simulated particles, a detailed simulation of the TPC continues the flow of data. The TPC Response Simulator (TRS) [58] models physical processes such as the drift of ionization electrons in the TPC gas, the electron avalanche near the anode wires of the MWPC, the charge induction on the readout pads in time bins, and the digitization of the signal.

The next step is to do the embedding of simulated data into real events. The ADC counts from the simulation are added to the ADC counts from real events and the sum is processed through the reconstruction software chain. The Monte Carlo data is stored along with the reconstructed data in DSTs and is later used to calculate the acceptance and efficiency correction factors to the real data. For the correction factors to be considered valid, the simulation must be accurate so that the reconstruction of the simulated particles exhibit

the same properties as real particles. The TRS package is evaluated in [58] and seen to reproduce the data well. The simulation is also evaluated for this analysis, as detailed in §5.5.

## 5.4 Correction Factors

The total correction applicable to the real data is usually broken up into acceptance and reconstruction efficiency.

### 5.4.1 Acceptance

The acceptance is defined as the ratio of Monte Carlo particles which pass into the TPC to the number of generated particles,

$$\text{acceptance} = \frac{\#\text{accepted}}{\#\text{generated}}. \quad (5.7)$$

Accepted particles are those that might possibly be reconstructed, while those particles which fall outside of the acceptance have no chance of being reconstructed. In particular, accepted Monte Carlo  $\Xi^-$  particles used in this analysis are defined by the cuts listed in Table 5.2. These cuts are chosen based on the basic reconstruction cuts (Table 4.2) and loose cuts from an acceptance filter code, which runs during the embedding process.

The acceptance is dependent on the transverse momentum (mass) and rapidity of the particles, but not on the event multiplicity. This is because the factor is derived from Monte Carlo data only, where the identification of an accepted  $\Xi^-$  particle does not depend on the number of other particles

| Requirements for $\Xi^-$ Acceptance  |                               |
|--------------------------------------|-------------------------------|
| Cut Variable                         | Value                         |
| GEANT $\Xi$ Vertex Parent Track ID   | $\Xi^-$                       |
| $\Xi^-$ Transverse Momentum          | $0.5 < p_{\perp} < 3.5$ GeV/c |
| $\Xi^-$ Rapidity                     | $ y  < 0.75$                  |
| $\Xi^-$ GEANT Decay Mode             | $\rightarrow \Lambda\pi^-$    |
| GEANT Bachelor Track ID              | $\pi^-$                       |
| GEANT V0 Vertex Parent Track ID      | $\Lambda$                     |
| $\Lambda$ GEANT Decay Mode           | $\rightarrow p\pi^-$          |
| $\Lambda$ Positive Daughter Track ID | $p$                           |
| $\Lambda$ Negative Daughter Track ID | $\pi^-$                       |
| TPC Hits, Bachelor                   | $> 4$                         |
| TPC Hits, $\Lambda$ Daughters        | $> 10$                        |
| Decay Distance from PV, $\Xi^-$      | $> 2$ cm                      |
| Decay Distance from PV, V0           | $> 5$ cm                      |
| DCA V0 to PV                         | $< 2.5$ cm                    |
| DCA Negative Daughter to PV          | $> 2$ cm                      |
| DCA Positive Daughter to PV          | $> 0.4$ cm                    |

Table 5.2: Acceptance cuts for  $\Xi^-$ . PV is short for Primary Vertex.

in the sample. Figure 5.11 shows the acceptance correction as a function of  $(y, p_{\perp})$ . There is not much variation as a function of rapidity due to the analysis cut  $|y| < 0.75$ . The  $p_{\perp}$  dependence is quite pronounced within the range  $0.5 < p_{\perp} < 3.5$  GeV/c, as seen in Figure 5.12. The acceptance correction for  $\Xi^-$  and  $\Xi^+$  are the same, as expected due to the symmetry of the STAR detector.

#### 5.4.2 Reconstruction Efficiency

The reconstruction efficiency is defined as the ratio of successfully reconstructed Monte Carlo particles after the final analysis cuts (Table 5.1) are

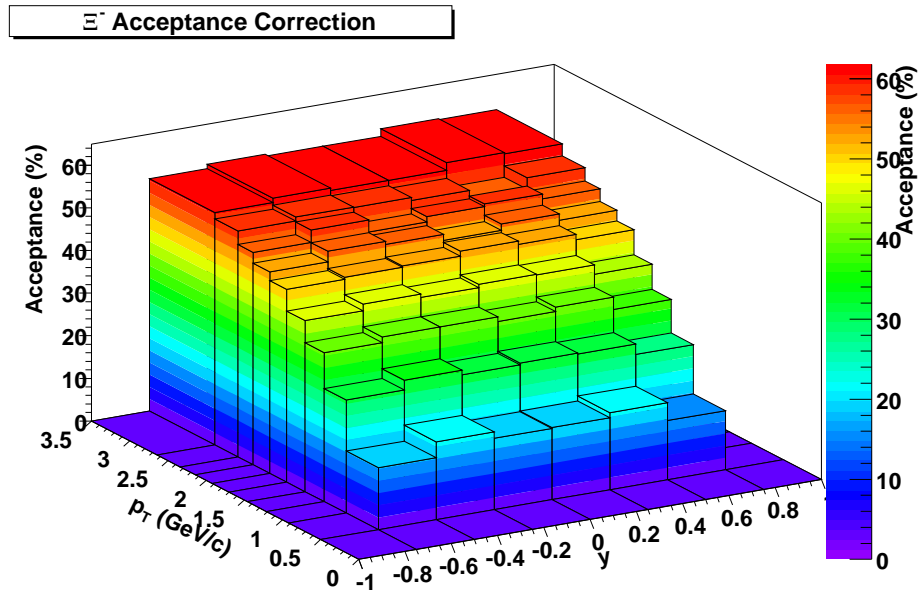


Figure 5.11: Acceptance correction as a function of  $(y, p_{\perp})$  for  $\Xi^{-}$ .

applied to the number of accepted Monte Carlo particles (Table 5.2),

$$\text{reconstruction efficiency} = \frac{\#\text{reconstructed}}{\#\text{accepted}}. \quad (5.8)$$

To calculate this ratio, knowledge of whether or not a Monte Carlo particle has been reconstructed is found through an association process between simulated and reconstructed hits and tracks. The first stage of association occurs by applying the condition that a reconstructed hit falls within 0.5 cm in the three spatial dimensions of a simulated hit. After the hit association is complete, track association is done with the requirement that a reconstructed track must share at least 3 associated hits with a simulated track. The last part involves ensuring the associated tracks originated from the same secondary vertex. This is sufficient for  $\Lambda$  association, but  $\Xi^{-}$  association is slightly more complicated.



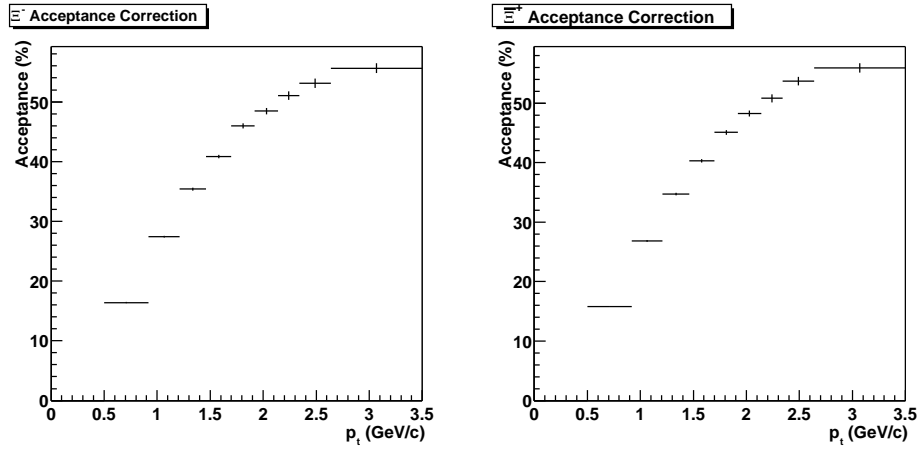


Figure 5.12: Acceptance correction as a function of  $p_{\perp}$  for  $\Xi^-$  (left) and  $\Xi^+$  (right).

The simulated bachelor track from a  $\Xi^-$  decay must also be associated to a reconstructed track. The associated bachelor track then has to be seen to originate from the same decay vertex as the associated  $\Lambda$ . If this is observed to be the case, then identification of an associated  $\Xi^-$  is nearly complete. The final step is to apply the final analysis cuts to the successfully associated  $\Xi^-$  particles. Table 5.3 lists the requirements for successful association of a simulated and reconstructed  $\Xi^-$  ( $\Xi^+$ ) particle.

Like the acceptance, the reconstruction efficiency depends on rapidity and transverse momentum (mass) in general. As is done in the acceptance calculation, the rapidity dependence is integrated out since it is essentially flat in the region this analysis examines. There is a difference though in that the reconstruction efficiency further depends on the centrality. Figure 5.13 shows the  $\Xi^-$  and  $\Xi^+$  reconstruction efficiencies as functions of  $p_{\perp}$  for the centrality

| Requirements for Association |  |
|------------------------------|--|
| Association Type             | Requirement  |
| Hits                         | $ \text{RC-MC} _{x,y,z} < 0.5 \text{ cm}$                                    |
| Tracks                       | number of common hits $> 3$  |
| V0                           | 2 oppositely charged particles (tracks)<br>matched to same vertex            |
| Xi                           | V0 parent and bachelor particles (tracks)<br>matched to same (non-V0) vertex |

*Include Table 5.1 here except for PID*

Table 5.3: Association requirements for  $\Xi^-$  ( $\Xi^+$ ). RC refers to reconstructed and MC to Monte Carlo. The PID efficiency cut from the final analysis cuts is not included (see §5.4.3).

bins studied here.

### 5.4.3 Total Correction

The total efficiency correction is the product of the acceptance and the reconstruction efficiency. It can also be calculated by taking the ratio of the number of reconstructed Monte Carlo particles to the number of generated Monte Carlo particles, as is easily seen from Equation 5.9,

$$\text{total efficiency correction} = \frac{\#\text{accepted}}{\#\text{generated}} \times \frac{\#\text{reconstructed}}{\#\text{accepted}}. \quad (5.9)$$

Figure 5.14 shows the total efficiencies of reconstruction for  $\Xi^-$  and  $\Xi^+$  as functions of  $p_{\perp}$  for differing centrality cuts.

There are actually several other corrections that must be applied to the real data. Corrections for the branching ratios of the  $\Xi^-$  and  $\Lambda$  particles are made because the simulation fixed the branching ratios of these particles

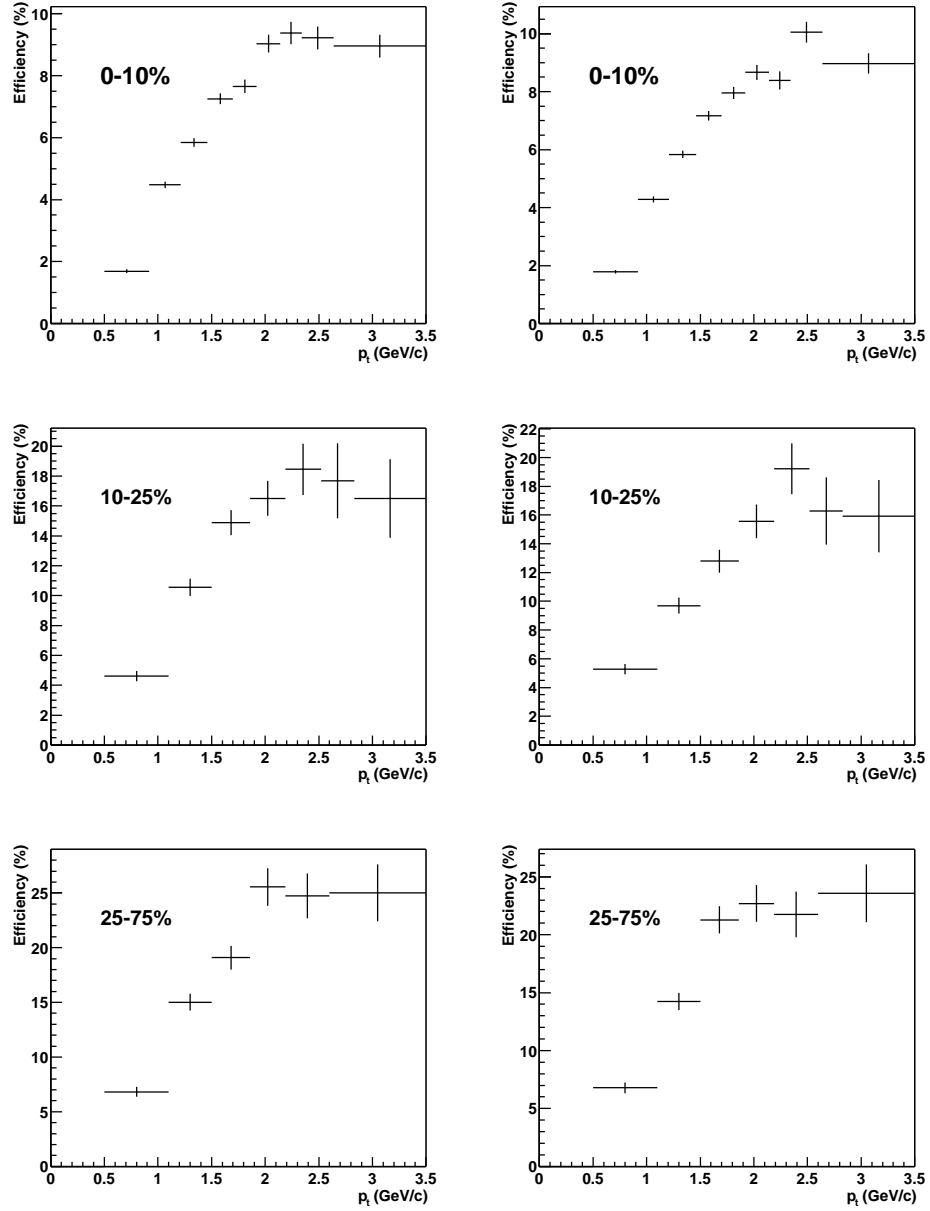


Figure 5.13: Reconstruction efficiencies for  $\Xi^-$  (left) and  $\Xi^+$  (right) as functions of  $p_{\perp}$  in the centrality bins under examination.

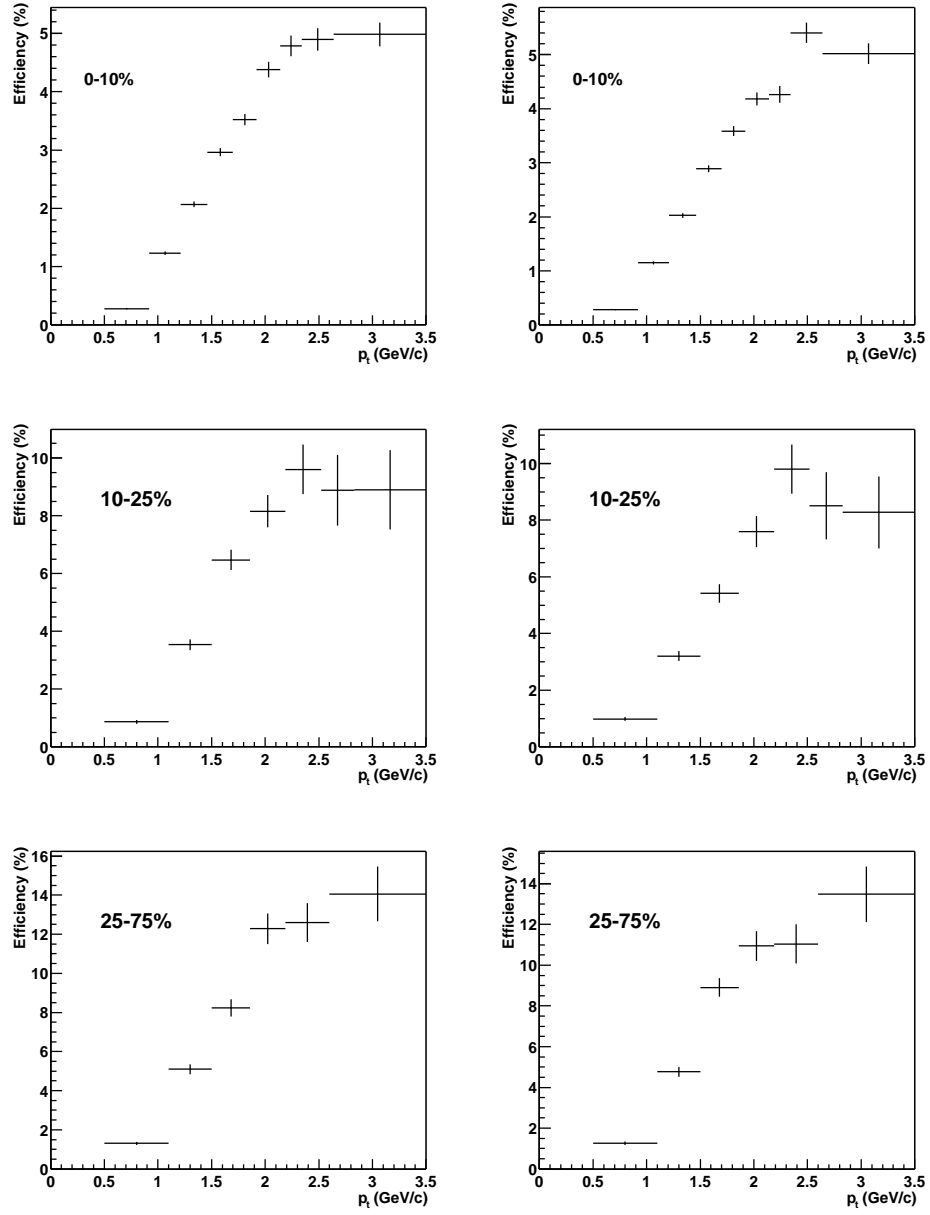


Figure 5.14: Total efficiency corrections as functions of  $p_{\perp}$  in different centrality bins for  $\Xi^-$  (left) and  $\Xi^+$  (right).

to be 100% for the most prominent mode of each particle. This introduces a branching ratio correction factor of 99.9% ( $\Xi^- \rightarrow \Lambda\pi^-$ )  $\times$  63.9% ( $\Lambda \rightarrow p\pi^-$ ) = 63.84%. Another correction factor comes from the use of particle identification via energy loss ( $dE/dx$ ) for analyzing real data, but not in the case of simulated data. As discussed in §5.1, a  $3\sigma$  cut was placed on each of the three final state charged particles of a  $\Xi^-$  ( $\bar{\Xi}^+$ ) decay. A  $3\sigma$  cut corresponds to approximately 99.73% of the total signal, so the use of this cut on three final state particles implies that  $99.73\% \times 99.73\% \times 99.73\% = 99.19\%$  of the total  $\Xi^-$  ( $\bar{\Xi}^+$ ) signal is actually measured. The third correction that must be applied is needed due to the finite mass window in which the signal is counted, which means signal counts in the tails of the peak can be cut off if the window is not large enough. This is referred to here as a tails efficiency, and is calculated by simply dividing the associated yield within the window by the associated yield before the mass cut.

Multiplying Equation 5.9 and these three correction factors produces the true total correction to be applied to the real data. Figure 5.15 shows the total efficiency, including these three corrections, as a function of  $m_{\perp}$ .

## 5.5 Simulation Quality Check

It is important to know that the quality of the simulations is sufficient to utilize the correction factors obtained from them. This can be done by ensuring the simulated data faithfully reproduces the real data distributions through comparison of various geometric and kinematic variables. The validity

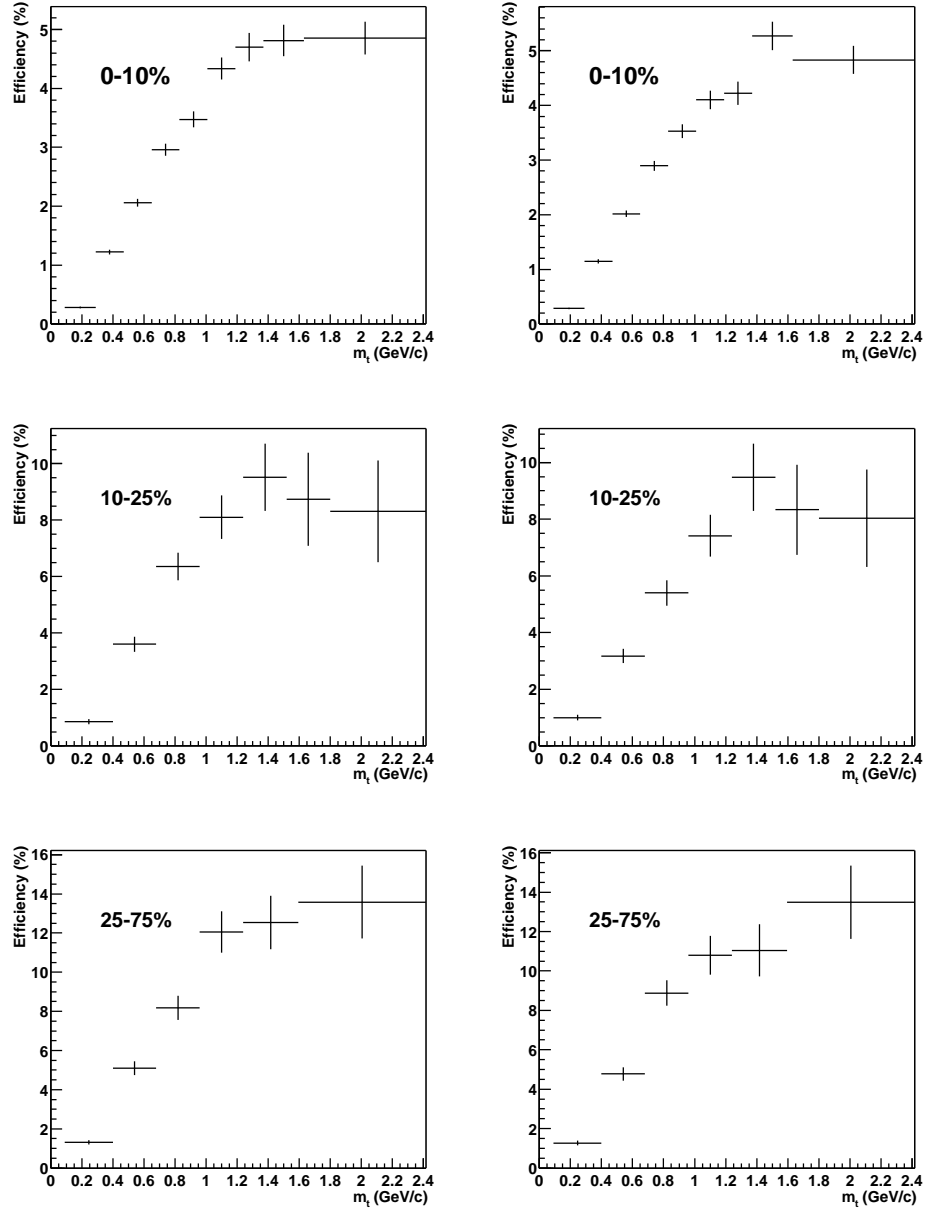


Figure 5.15: Total efficiency corrections as functions of  $m_{\perp}$  for  $\Xi^-$  (left) and  $\Xi^+$  (right).

of the corrections themselves can be obtained by reproducing known physical characteristics of the particles in question. For example, the lifetime of the  $\Xi^-$  ( $\bar{\Xi}^+$ ) can be calculated for the real data after application of the corrections and compared to the expected value.

### 5.5.1 Distribution Comparisons

This analysis is able to obtain the  $\Xi^-$  signal for any particular bin of any variable or combination of variables using the calculated invariant mass distribution for said bin. This is done by the signal extraction method outlined in §5.2.3. However, this method does not allow for the unique identification of a real  $\Xi^-$  particle, so a comparison between the distributions of any particular variable for real and simulated  $\Xi^-$ s requires a small amount of work. A comparison can be made by borrowing from the Bin Counting Method. Since the invariant mass ranges for the signal and the two background regions are known, it is possible to create a distribution from both the peak and the background. The process is simple: fill a histogram for a particular variable from entries within the mass peak range and subtract a histogram created from the entries in the two background regions about the peak.

Figures 5.16-5.20 show the results of the comparison for 330k of the 10% most central events. The histograms on the left show the total distributions in the mass peak range in black. Also shown are the background contributions in green and the background subtracted distributions in blue. The histograms on the right show the background subtracted distributions again in blue and the

reconstructed Monte Carlo distributions in red. As can be seen, the simulated data describes the real data well. This supports the claim that the simulated data describes the real data and so is useful for calculating correction factors.

### 5.5.2 Lifetime Check

Another test of the validity of the simulations is done by calculating the lifetime of the  $\Xi^-$  ( $\Xi^+$ ) particles from the data. This test requires the use of the correction factors described in §5.4. The lifetime of a particle can be written as

$$c\tau = m \times \frac{d}{p} \quad (5.10)$$

where  $m$  is the mass of the particle,  $d$  is the distance the particle travels before decaying, and  $p$  is the total momentum [cite]. The lifetime is commonly quoted as  $c\tau_0$  and for the  $\Xi^-$  ( $\Xi^+$ ) it is 4.91 cm [49].

Given the characteristic lifetime  $c\tau_0$  of a particle, the number of surviving particles at a particular time  $\tau$  is

$$N(c\tau) = N_0 \times e^{-c\tau/c\tau_0} \quad (5.11)$$

where  $N_0$  is the number of particles produced from the collision. The real data distribution must be corrected before the characteristic lifetime can be calculated. The natural variables to bin the data in are  $c\tau$  and  $p$ . However, the embedding for  $\Xi^-$  and  $\Xi^+$  were done as functions of the transverse momentum, so for this analysis, the data is binned and corrected in terms of  $c\tau$  and  $p_\perp$ . Figure 5.21 displays the real data and total efficiency distributions for  $\Xi^-$  as functions of  $c\tau$  and  $p_\perp$  for 330k of the 10% most central events.



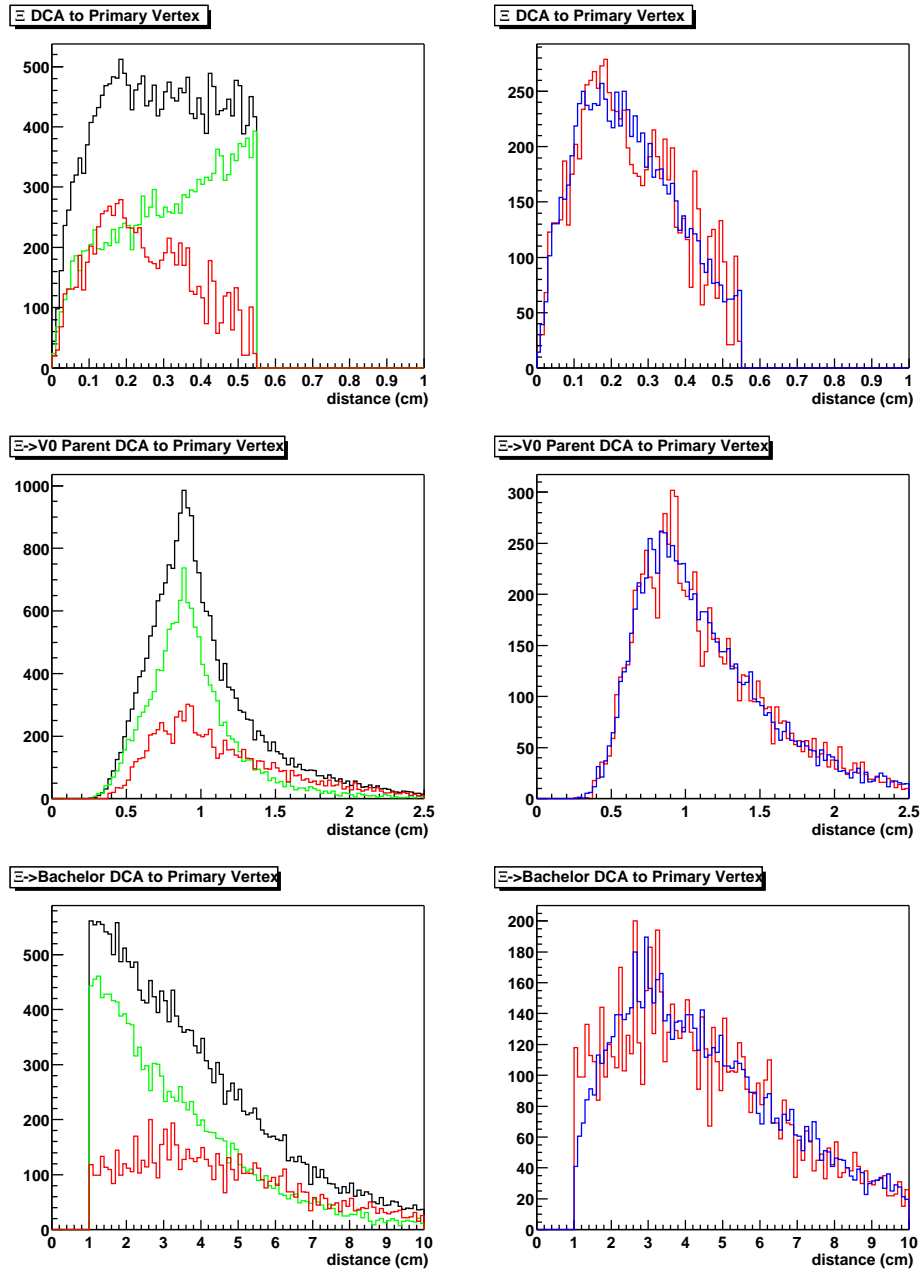


Figure 5.16: Distribution comparisons between simulated and real data. Histograms on the left contain total peak distributions (black), background distributions (green), and signal distributions (red). Histograms on the right contain signal distributions (red) and simulated distributions (blue).

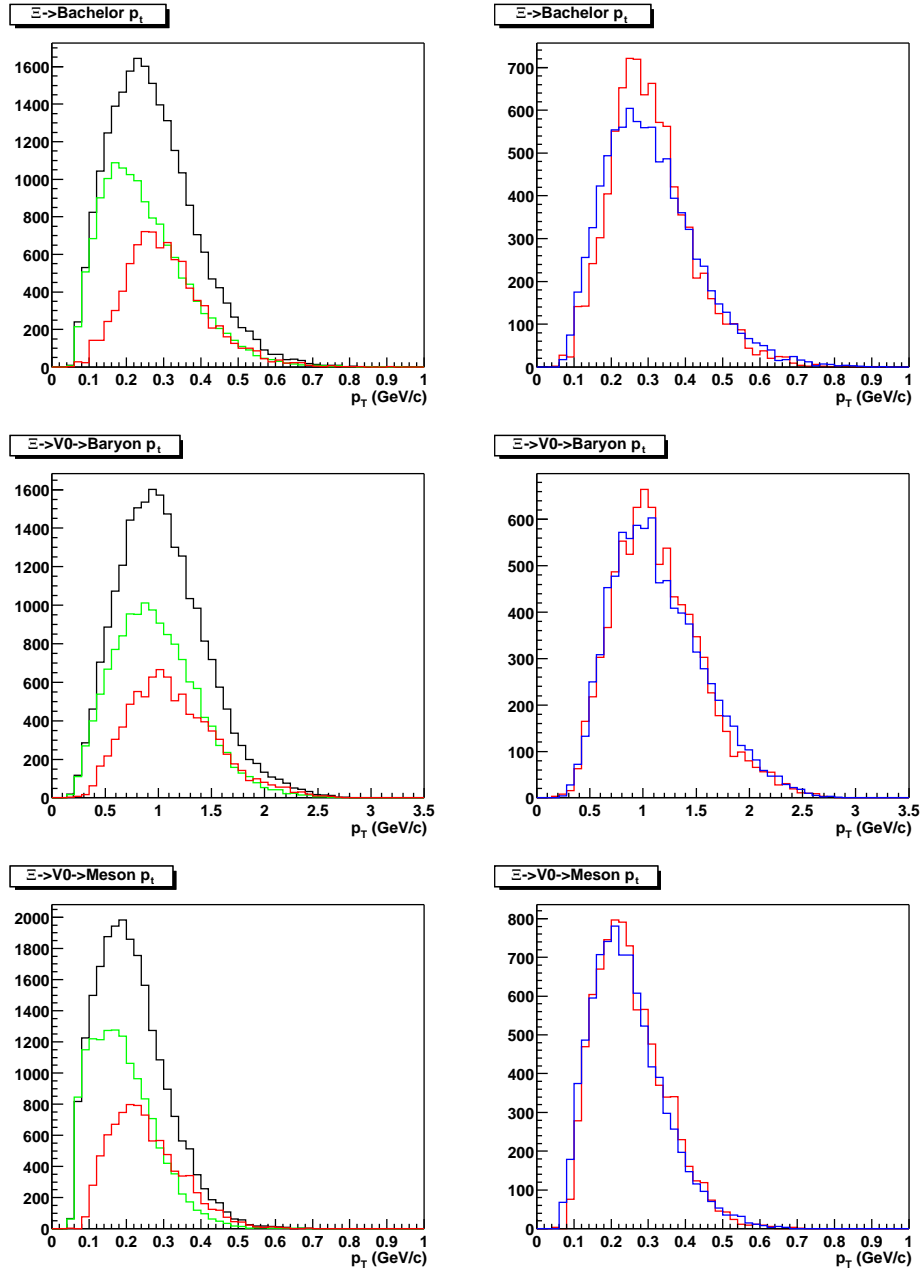


Figure 5.17: Distribution comparisons between simulated and real data continued. See Figure 5.16 for description of colors.

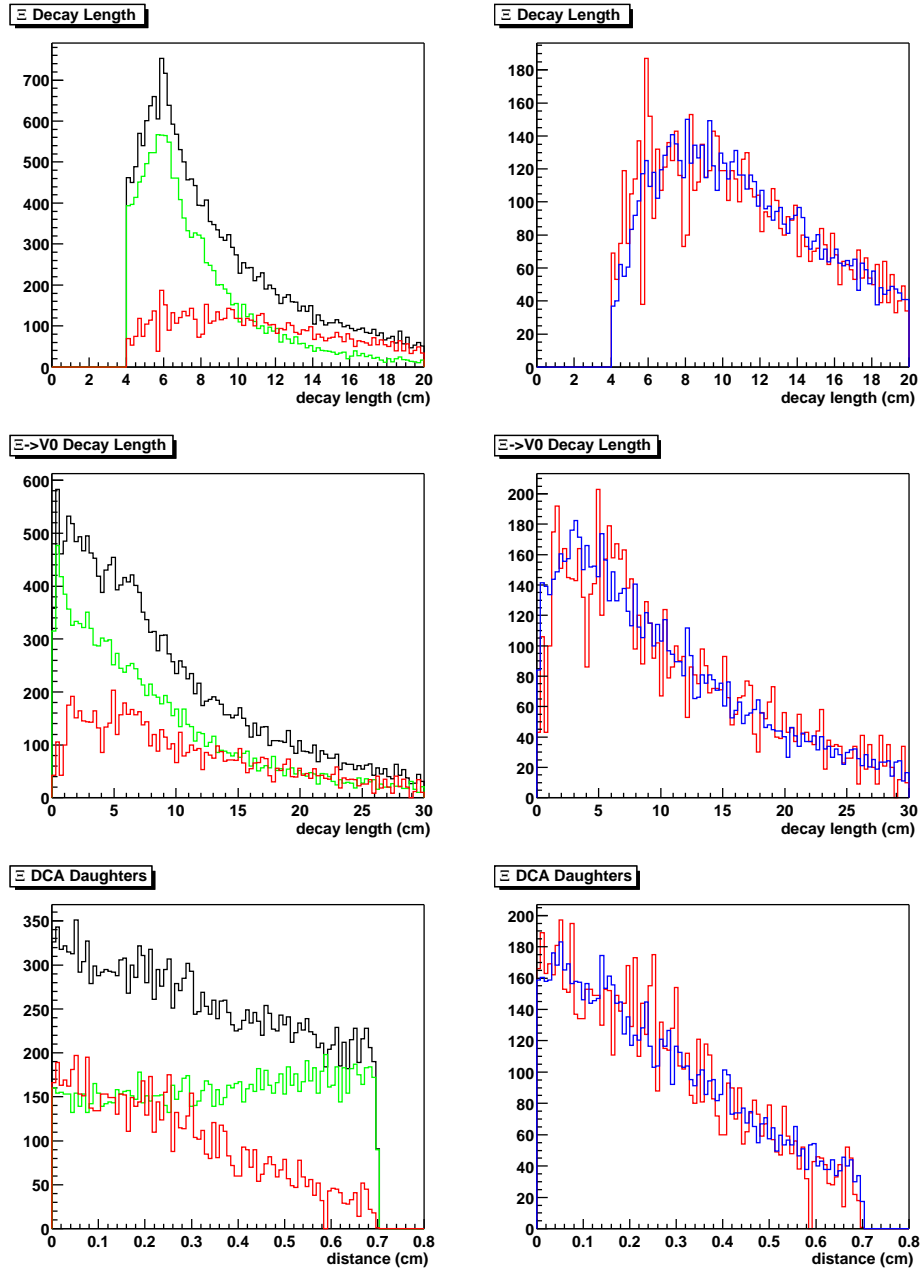


Figure 5.18: Distribution comparisons between simulated and real data continued. See Figure 5.16 for description of colors.

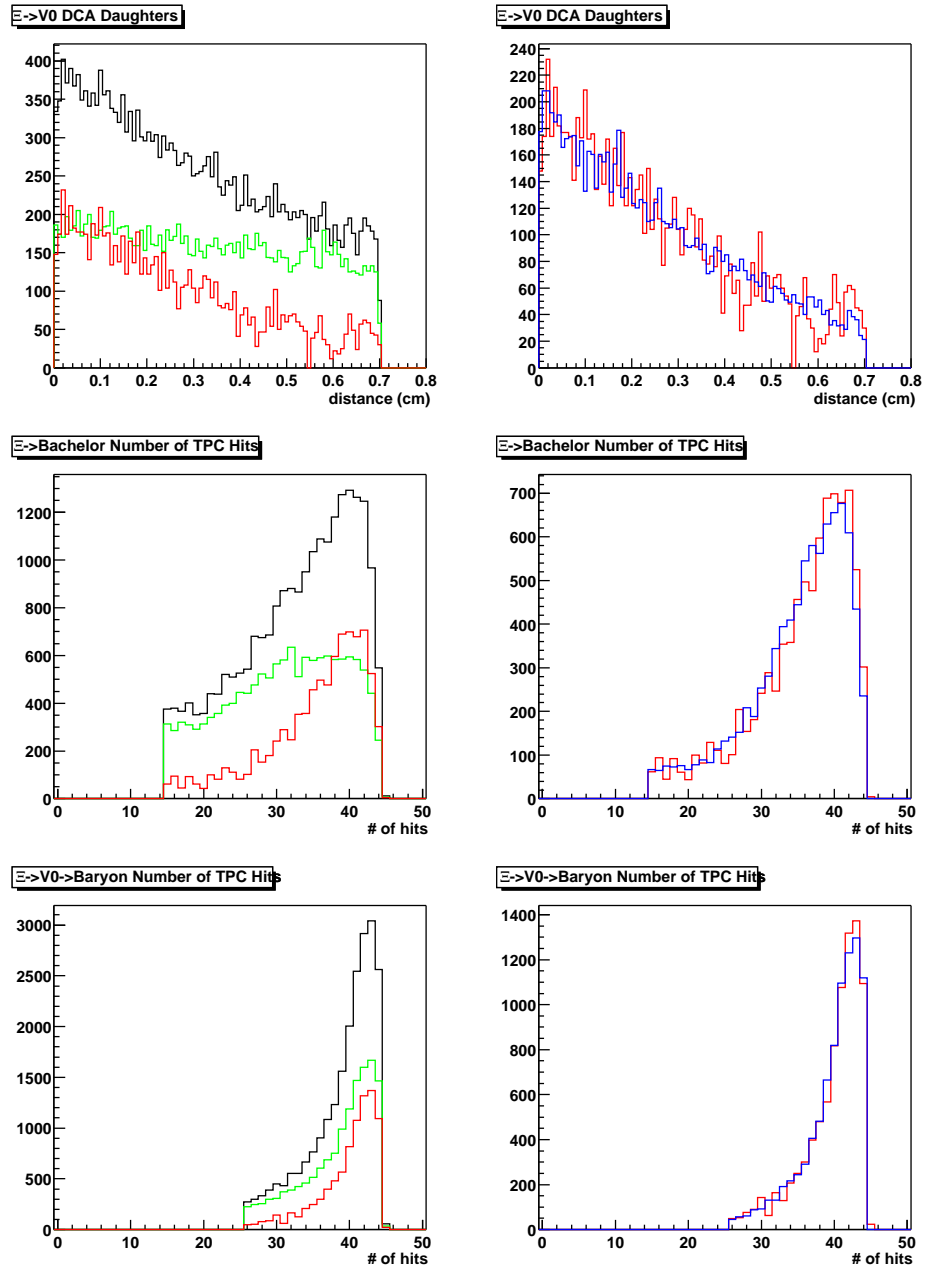


Figure 5.19: Distribution comparisons between simulated and real data continued. See Figure 5.16 for description of colors.

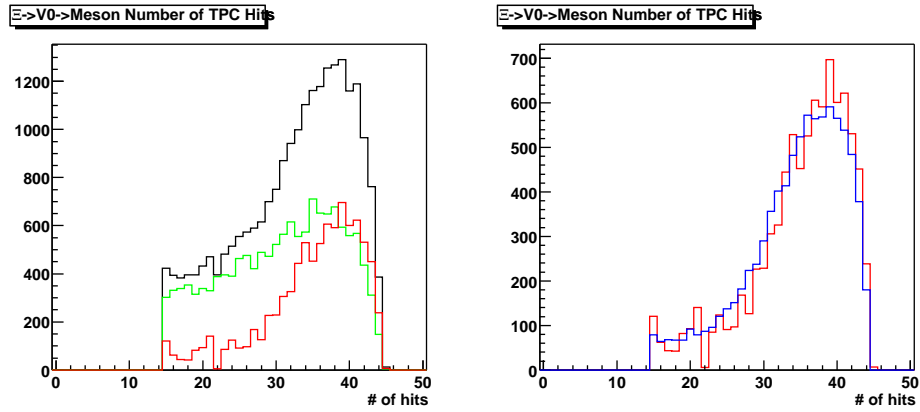


Figure 5.20: Distribution comparisons between simulated and real data continued. See Figure 5.16 for description of colors.

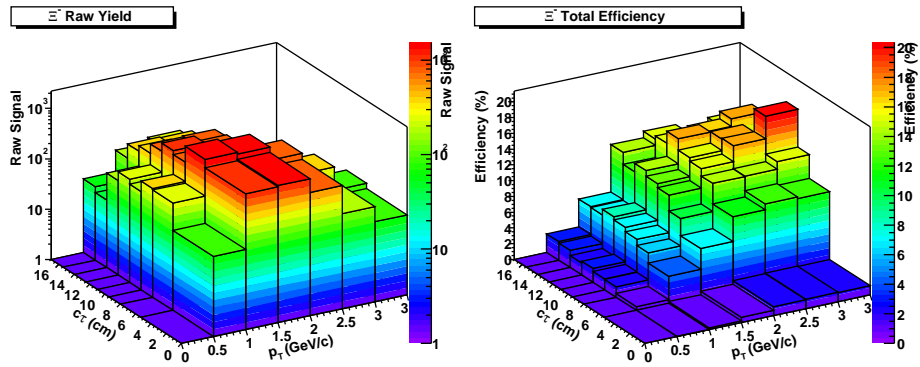


Figure 5.21:  $\Xi^-$  raw yield (left) and total efficiency (right) in bins of  $(c\tau, p_{\perp})$ .

Once the corrected distribution is obtained, a projection to the  $c\tau$  axis is done for various transverse momentum ranges. Caution must be taken prior to projecting the data, though. The cuts on transverse momentum and decay length (see Table 5.1) imply that there exists regions where the efficiency of finding real  $\Xi^-$  particles is zero and so these regions must not be included in the lifetime calculation. This implies a minimum value for the lifetime given a minimum value for transverse momentum. Rearranging the terms in Equation

5.10 gives

$$m \times d = c\tau \times p. \quad (5.12)$$

For this analysis, the minimum value for  $p_{\perp}$  is 0.5 GeV/c. Since  $p_{\perp}$  is always less than or equal to the total momentum,  $p$  must also be at least 0.5 GeV/c. The known  $\Xi^{-}$  mass and the minimum decay length value implies that

$$m_{\Xi^{-}} \times d > 7.93 \Rightarrow c\tau \times p > 7.93 \quad (5.13)$$

where  $m_{\Xi^{-}} = 1.321$  and  $d > 6$ . Here, the decay length cut is considered to be 6 cm instead of a linear relationship with the decay length of the  $\Lambda$  daughter to ease calculations. While this assumption reduces the number of valid  $\Xi^{-}$  particles in the sample, there are still enough to check the corrected lifetime.

Based on Equation 5.13, the limit on a valid  $c\tau$  range can be found for a particular limit on transverse momentum. If candidates with  $p_{\perp} > 1.0$  are projected onto the  $c\tau$ -axis, then  $c\tau > 7.93$  represents the valid lifetimes. Likewise,  $p_{\perp} > 1.5$  implies  $c\tau > 5.29$ . To minimize any bias that might be introduced due to using  $p_{\perp}$  instead of  $p$ , several  $c\tau$  fit ranges are chosen to determine the lifetime of the real data  $\Xi^{-}$  particles.

The corrected  $\Xi^{-}$  and  $\Xi^{+}$  yields were summed due to limited statistics. The corrected yield in bins of  $(c\tau, p_{\perp})$  along with an example of the projected data and lifetime fit is shown in Figure 5.22. Table 5.4 displays the results from various fit ranges. The measured values of the lifetime match the expected value of 4.91 cm well and so further proves the validity of the simulations.

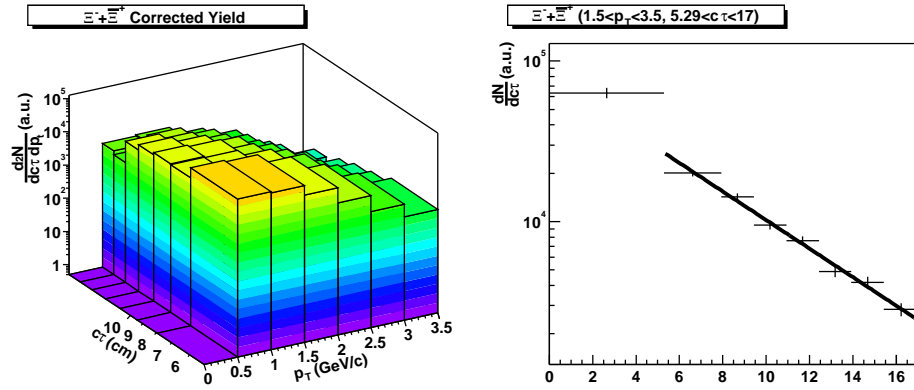


Figure 5.22: Corrected  $\Xi^- + \Xi^+$  yield in  $(p_{\perp}, c\tau)$  bins (left) and projected data as a function of  $c\tau$  (right). The line represents an exponential fit to the projected data, the results of which are listed in Table 5.4. Statistical errors only.

Again, the results reported are from 330k of the 10% most central events.

Only statistical errors are reported.

| $\Xi^- + \Xi^+$ Lifetime |                     |                           |
|--------------------------|---------------------|---------------------------|
| Projection (GeV/c)       | Fit Range (cm)      | Calculated $c\tau_0$ (cm) |
| $1.0 < p_{\perp} < 3.5$  | $7.93 < c\tau < 17$ | $4.78 \pm 0.22$           |
|                          | $9.43 < c\tau < 17$ | $4.46 \pm 0.27$           |
| $1.5 < p_{\perp} < 3.5$  | $5.29 < c\tau < 17$ | $4.88 \pm 0.19$           |
|                          | $7.93 < c\tau < 17$ | $4.74 \pm 0.26$           |
|                          | $9.43 < c\tau < 17$ | $4.99 \pm 0.38$           |

Table 5.4: Calculated  $\Xi^- + \Xi^+$  lifetimes for various  $p_{\perp}$  and  $c\tau$  ranges. Errors are statistical.

# Chapter 6

## Results and Discussion

### 6.1 Experimental Results

The data presented here are for collisions with a primary vertex  $z$ -position cut of  $|z| < 75$  cm and reconstruction cuts of Table 5.1. Also, data is binned in centrality according to Table 4.1.

#### 6.1.1 $\bar{\Xi}^+$ to $\Xi^-$ Ratio

The dependence of the  $\Xi^-$  and  $\bar{\Xi}^+$  yields on such variables as transverse momentum (mass), rapidity, and centrality requires knowledge of efficiency corrections. However, as the STAR detector response is assumed to be symmetric with respect to  $\Xi^-$  and  $\bar{\Xi}^+$  reconstruction, the raw yields are sufficient information to produce  $\bar{\Xi}^+/\Xi^-$  and to examine said ratio as a function of these variables. Effects due to absorption of anti-particles, especially anti-protons, in the detector material and feed-down  $\Omega^-$  and  $\bar{\Omega}^+$  can potentially affect the  $\bar{\Xi}^+/\Xi^-$  ratio. The absorption of  $\bar{\Xi}^+$ ,  $\bar{\Lambda}$ , and  $\bar{p}$  as a function of  $p_\perp$  has been examined and affects the integrated ratio by only 0.2%. Figure 6.1 shows the absorption rate for  $\bar{\Xi}^+$  particles up to 2 GeV/c in transverse momentum given an input distribution flat in  $p_\perp$ . By  $p_\perp = 1$  GeV/c, the absorption rate has fallen to near zero. The overall effect is to increase the number of  $\bar{\Xi}^+$  by only



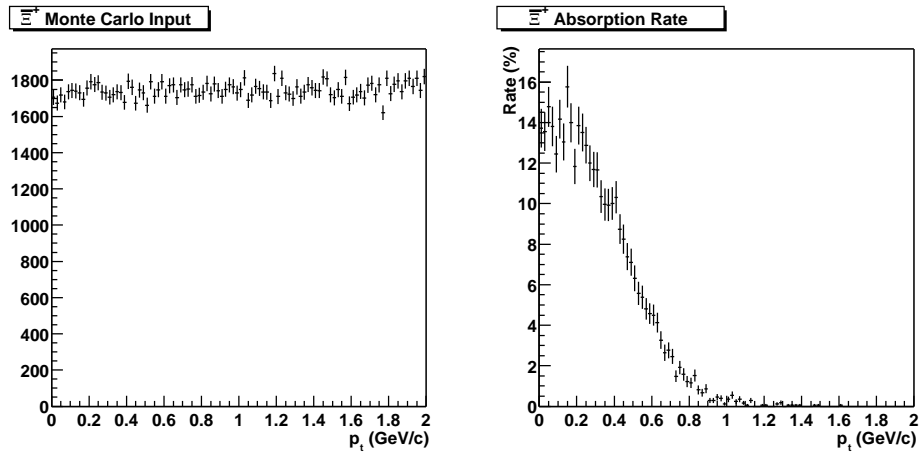


Figure 6.1:  $\Xi^+$  absorption rate, including  $\bar{\Lambda}$  and  $\bar{p}$ , due to detector material. The left figure displays the Monte Carlo input and the right figure shows the absorption rate. The rate falls rapidly to near-zero by 1 GeV/c.

| Uncorrected Signal |                           |                |                 |                |                 |
|--------------------|---------------------------|----------------|-----------------|----------------|-----------------|
| Centrality Bin     | $\langle N_{h^-} \rangle$ | $N_{\Xi^-}$    | $N_{\Xi^-}/evt$ | $N_{\Xi^+}$    | $N_{\Xi^+}/evt$ |
| I                  | $270.6 \pm 6.5$           | $8485 \pm 198$ | 0.026           | $7233 \pm 177$ | 0.022           |
| II                 | $165.2 \pm 5.5$           | $1217 \pm 67$  | 0.027           | $932 \pm 60$   | 0.021           |
| III                | $45.0 \pm 3.6$            | $1003 \pm 42$  | 0.008           | $869 \pm 37$   | 0.007           |

Table 6.1: Uncorrected signal reconstructed in the 3 centrality bins.

a handful of counts and so is neglected in this analysis. The feed-down contribution comes from the  $\Omega^- \rightarrow \Xi^- \pi^0$  channel which has a 8.6% branching ratio [49] and has also been neglected here.

Table 6.1 displays the number of raw reconstructed  $\Xi^-$  and  $\Xi^+$  particles for the three centrality bins examined. Figure 6.2 shows that  $\Xi^+/\Xi^-$  is flat with respect to the event centrality. The centrality is shown in terms of the negative hadron ( $h^-$ ) density at mid-rapidity,  $dN_{h^-}/d\eta$ . The negative hadron multiplicity is taken as a function of pseudo-rapidity, which is defined

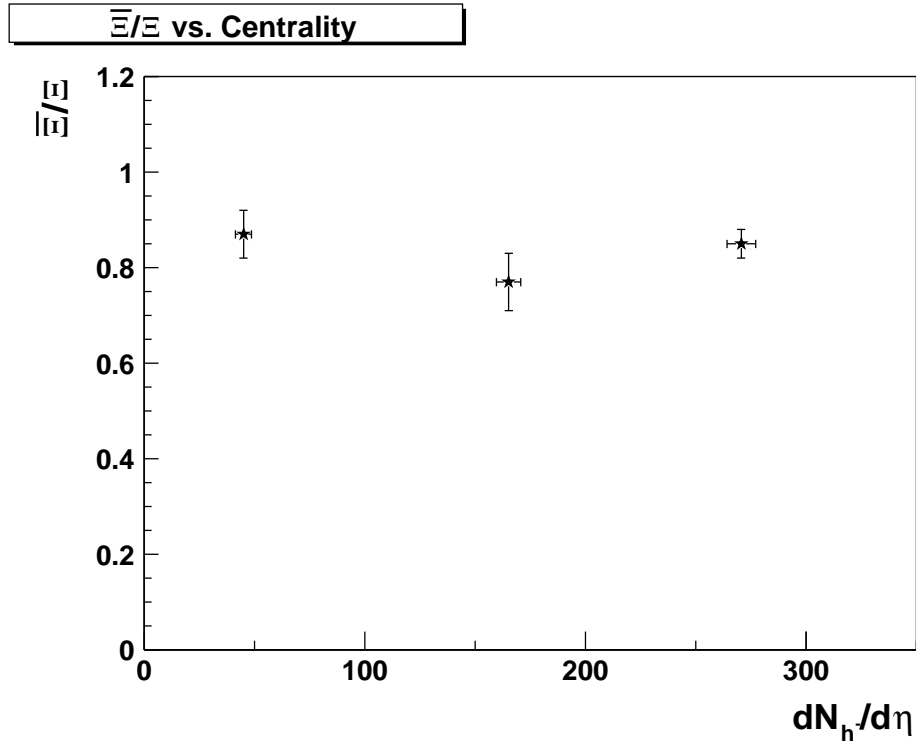


Figure 6.2:  $\bar{\Xi}^+/\Xi^-$  versus centrality. Statistical errors are shown.

in Appendix 1, instead of rapidity because only the charge and momentum are known for those particles. In other words, there is not enough information to know the energy of a particle, which is needed to calculate the rapidity.

Seen as a function of rapidity in Figure 6.3, the  $\bar{\Xi}^+/\Xi^-$  ratio again does not deviate significantly from a constant. The flatness of  $\bar{\Xi}^+/\Xi^-$  seems to indicate that the production mechanisms for  $\Xi^-$  and  $\bar{\Xi}^+$  are similar in the rapidity range examined. This is also an indication that the incident baryons are mostly removed from the mid-rapidity region. The BRAHMS collaboration verified this by measuring the  $\bar{p}/p$  ratio as a function of rapidity. They found

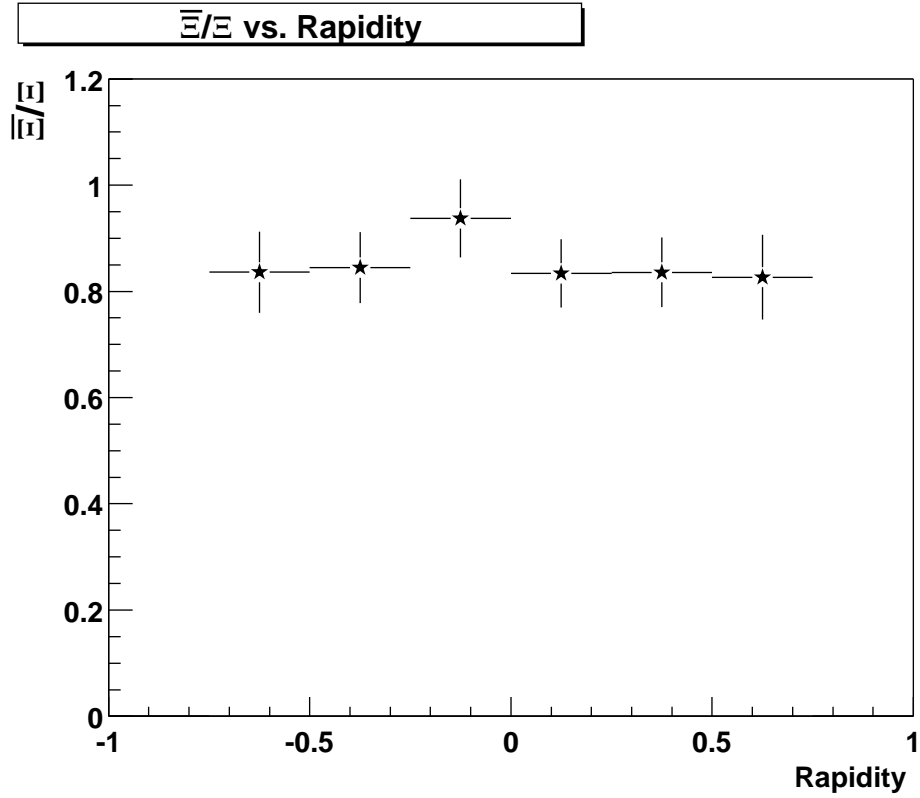


Figure 6.3:  $\bar{\Xi}^+/\Xi^-$  versus rapidity for the 10% most central events. Statistical errors are shown.

a ratio of  $0.66 \pm 0.04 \pm 0.06$  at mid-rapidity and a ratio of  $0.41 \pm 0.04 \pm 0.06$  at 2 units of rapidity [32]. This supports the argument that there is a significant degree of collision transparency, even if the mid-rapidity region is not completely net-baryon free. For  $\Xi^-$  and  $\bar{\Xi}^+$  though, this dependence is even weaker since the majority of the valence quarks are from  $s\bar{s}$  production rather than from the incident baryons.

The  $\bar{\Xi}^+/\Xi^-$  ratio as a function of transverse momentum is also flat within statistical error bars as seen in Figure 6.4, again indicating that the

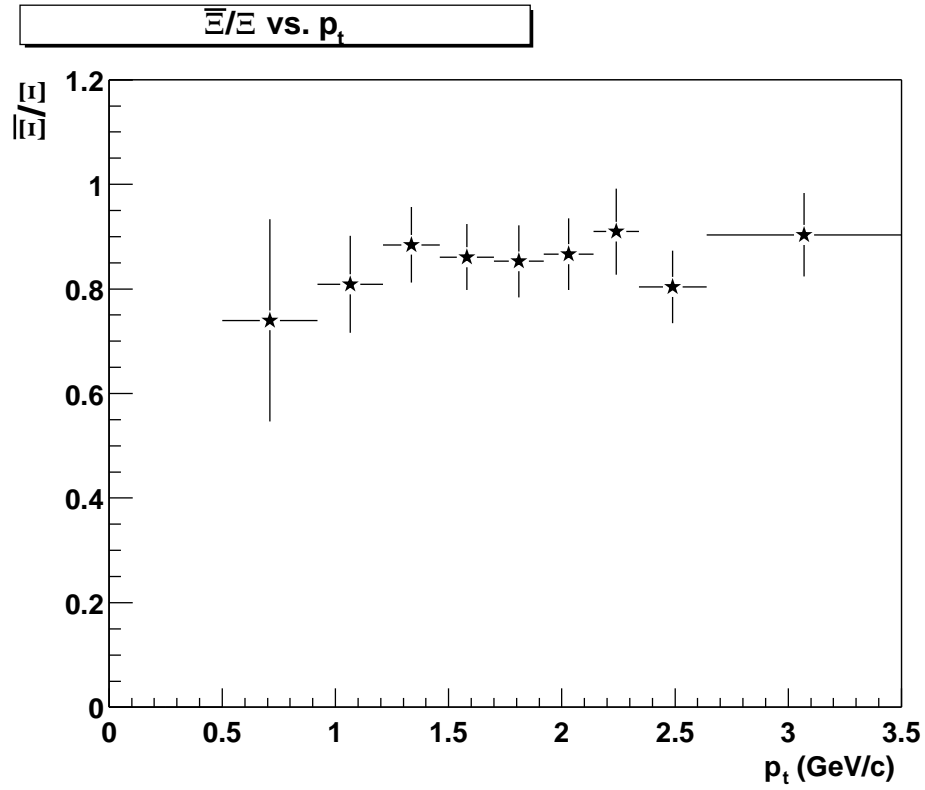


Figure 6.4:  $\bar{\Xi}^+/\Xi^-$  versus  $p_{\perp}$  for the 10% most central events. Statistical errors are shown.

production mechanisms between  $\Xi^-$  and  $\bar{\Xi}^+$  are not significantly different. The data points indicate the ratio for events from the top 10% of total hadronic cross-section.

An integrated ratio of  $\bar{\Xi}^+/\Xi^- = 0.85 \pm 0.03(stat.) \pm 0.05(sys.)$  was measured in the phase space volume defined by  $|y| < 0.75$  and  $0.5 < p_{\perp} < 3.5$  GeV/c for the top 10% most central events. The systematic error was estimated by varying the final analysis cuts.

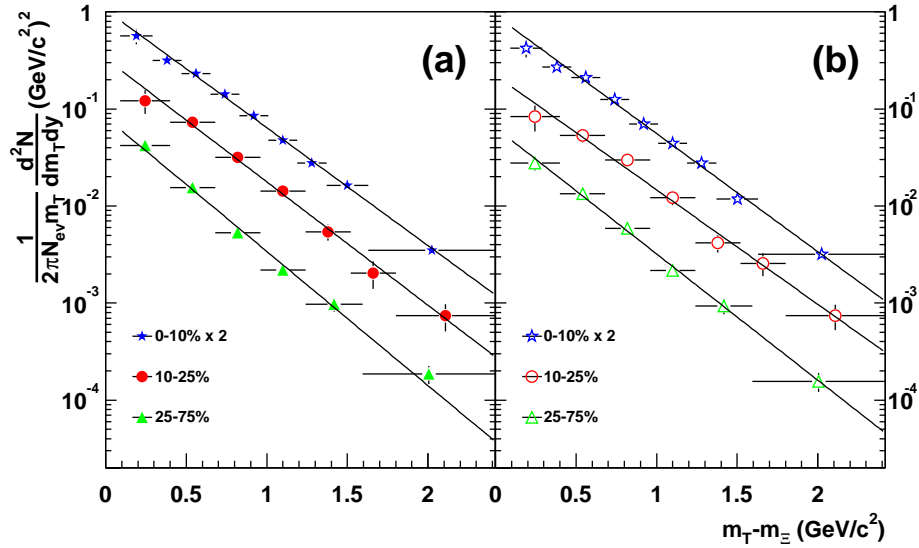


Figure 6.5: Fits to the  $m_{\perp}$  distributions for (a)  $\Xi^{-}$  and (b)  $\Xi^{+}$ .

### 6.1.2 Transverse Mass Distributions

The corrections, as discussed in §5.4, allow the determination of the absolute  $\Xi^{-}$  and  $\Xi^{+}$  yields as functions of transverse mass, rapidity, and centrality. Recall that the multiplicity distribution of a particle species originating from a thermally equilibrated source [50] can be written as

$$\frac{1}{2\pi m_{\perp}} \frac{d^2N}{dm_{\perp} dy} = \frac{dN/dy}{2\pi T(m_0 + T)} e^{-(m_{\perp} - m_0)/T} \quad (6.1)$$

where  $T$  is the temperature of the particle,  $dN/dy$  is yield per unit rapidity,  $m_0$  is the rest mass, and  $m_{\perp}$  is the transverse mass. This equation is useful since it gives both the temperature and yield per unit of rapidity. It also allows for a direct comparison to other particle types since this equation is used often in the literature.

| Transverse Mass Fit Results |                |                          |                            |                             |
|-----------------------------|----------------|--------------------------|----------------------------|-----------------------------|
|                             | Centrality Bin | I (0% $\rightarrow$ 10%) | II (10% $\rightarrow$ 25%) | III (25% $\rightarrow$ 75%) |
| $\Xi^-$                     | $dN/dy$        | $1.98 \pm 0.08$          | $1.18 \pm 0.11$            | $0.26 \pm 0.02$             |
|                             | $T$ (MeV)      | $358 \pm 7$              | $342 \pm 16$               | $315 \pm 14$                |
|                             | $\chi^2/dof$   | 6.983/7                  | 2.919/5                    | 4.667/4                     |
| $\Xi^+$                     | $dN/dy$        | $1.73 \pm 0.07$          | $0.87 \pm 0.09$            | $0.22 \pm 0.02$             |
|                             | $T$ (MeV)      | $357 \pm 7$              | $368 \pm 19$               | $334 \pm 13$                |
|                             | $\chi^2/dof$   | 13.94/7                  | 5.461/5                    | 1.566/4                     |

Table 6.2: Transverse mass distribution fit results where yield per unit rapidity centered about mid-rapidity and the inverse slope (temperature) are the fit parameters. An exponential fit function is used to produce these results.

Figure 6.5 displays the  $m_{\perp} - m_0$  distribution for  $\Xi^-$  and  $\Xi^+$  in the three centrality bins considered here. The  $\Xi^-$  and  $\Xi^+$  particle yields in the measured  $m_{\perp}$  region corresponds to approximately 75% of the total yield per event, which is estimated by taking the ratio of the integral of the fit function in the measured  $m_{\perp}$  range to the integral of the fit function over all  $m_{\perp}$ . The lines represent the fits to the data as per Equation 6.1, where the free parameters are the temperature, also known as the inverse slope,  $T$ , and the rapidity density,  $dN/dy$ . The results of the fits are listed in Table 6.2.

The corrected anti-particle to particle ratio is seen to be  $\Xi^+/\Xi^- = 0.87 \pm 0.05$ , which compares favorably with the uncorrected ratio of the previous section.

The inverse slope parameters for  $\Xi^-$  and  $\Xi^+$  are comparable within each centrality class. This agrees with the previous observation that the  $\Xi^+/\Xi^-$  ratio appears to be independent of the transverse momentum (mass) within

the cut space examined. In other words, a large enough difference in the production mechanisms for  $\Xi^-$  and  $\bar{\Xi}^+$  particles could slew the transverse mass distribution for one particle compared to the other, resulting in a statistically significant difference in temperatures. Similarity in spectra between particle and anti-particle is also seen in the  $\Lambda$  and  $\bar{\Lambda}$  spectra [56].

The production rate measurements of Table 6.2 are not for only primary  $\Xi^-$  and  $\bar{\Xi}^+$  particles. Included also are contributions from the strong or electromagnetic decays of heavier resonances such as the  $\Xi(1530)$  as well as from the weak decays of  $\Omega^-$  and  $\bar{\Omega}^+$ . The resonances decay within the observed primary  $Au + Au$  interaction region, which means secondary  $\Xi^-$  and  $\bar{\Xi}^+$  particles are indistinguishable from primary ones in this analysis. As for the feed-down contribution from  $\Omega^-$  to  $\Xi^-$ , the branching ratio for decay channel  $\Omega^- \rightarrow \Xi^- \pi^0$  is only 8.6%, as mentioned earlier. STAR has measured the yield per unit rapidity for  $\Omega^- + \bar{\Omega}^+$  to be  $dN/dy = 0.64 \pm 0.14$  for the 14% most central events [51]. Knowledge of the branching ratio and the measured yield implies that the contamination from the decays of  $\Omega^-$  and  $\bar{\Omega}^+$  particles is less than 2%. The feed-down correction is considered negligible compared to the statistical errors involved in the  $\Xi^-$  and  $\bar{\Xi}^+$  measurements and so is neglected in this analysis.

Systematic effects on the fit results are estimated by varying the analysis cuts as well as the histogram bin sizes and fit ranges. A systematic error of  $\sim 20\%$  is estimated on the reported measurements.

## 6.2 Discussion

The previous results from this analysis are next compared to those from the SPS  $Pb + Pb$  data taken at  $\sqrt{s_{NN}} = 17.3$  GeV.

### 6.2.1 $\bar{\Xi}^+$ to $\Xi^-$ Ratio

A thermal analysis based on RHIC anti-baryon/baryon ( $\bar{B}/B$ ) ratios gives a baryo-chemical potential  $\mu_B = 46 \pm 5$  MeV and a chemical freeze-out temperature  $T_{ch} = 174 \pm 7$  MeV [39]. This result is in agreement with a separate thermal analysis which finds  $\mu_B = 41 \pm 5$  MeV and  $T_{ch} = 165 \pm 7$  MeV [48]. The chemical freeze-out temperature at RHIC does not differ much from  $T_{ch} = 168 \pm 2.4$  MeV which was inferred from the SPS central  $Pb+Pb$  collisions at  $\sqrt{s_{NN}} = 17.3$  GeV [38]. The baryo-chemical potential, however, dropped from  $\mu_B = 266 \pm 5$  MeV, indicating the production of a low net baryon density medium at mid-rapidity with higher energy collisions.

STAR  $\bar{B}/B$  ratio is plotted in Figure 6.6 for several hyperons [51, 56]. The ratio is seen to increase with increasing strangeness content, which may be explained by a quark coalescence model [33, 74]. This model predicts that the ratios are proportional to the number of produced quarks of a given flavor from the fireball. The number of produced quarks increases within baryons of increasing strangeness, hence the observed trend. The data points have not been corrected for feed-down from weak decays and include statistical errors only. Also included are data points from the SPS experiment WA97 [21], where the same trend is seen.



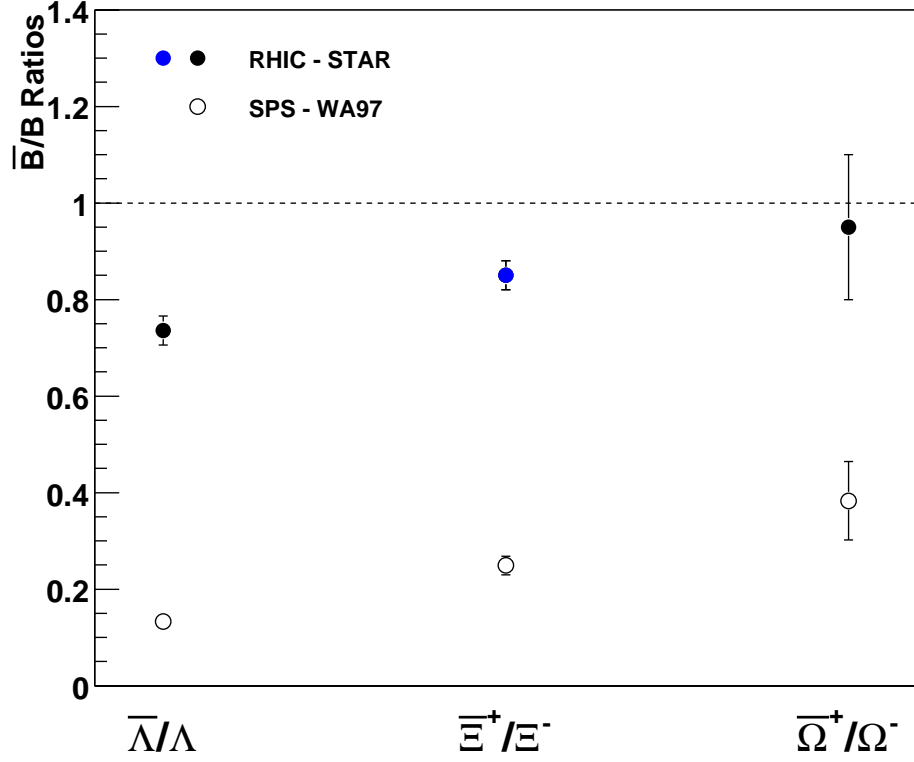


Figure 6.6:  $\bar{B}/B$  ratios as a function of  $|S|$  for RHIC  $Au + Au$  collisions at  $\sqrt{s_{NN}} = 130$  GeV and SPS  $Pb + Pb$  collisions at  $\sqrt{s_{NN}} = 17.3$  GeV. The solid circle for  $\bar{\Xi}^+/\Xi^-$  is the result from this thesis.

The observed trend with increasing  $|S|$  can be expressed within the framework of the coalescence model by linking the various ratios to a parameter  $D = q\bar{s}/\bar{q}s$  as in Equation 6.2.

$$D = \frac{K^+(u\bar{s})}{K^-(\bar{u}s)} = \frac{\Lambda(uds)}{\bar{\Lambda}(\bar{u}\bar{d}\bar{s})} \times \frac{\bar{\Xi}^+(\bar{d}\bar{s}\bar{s})}{\Xi^-(dss)} = \frac{\Xi^-(dss)}{\bar{\Xi}^+(\bar{d}\bar{s}\bar{s})} \times \frac{\bar{\Omega}^+(\bar{s}\bar{s}\bar{s})}{\Omega^-(sss)} \quad (6.2)$$

This allows for the calculation of the parameter  $D$ , which is in fact the  $K^+/K^-$  ratio, from other anti-hyperon to hyperon ratios. Alternatively, anti-hyperon to hyperon ratios can be predicted based on knowledge of  $D$ . Recent model

predictions for RHIC data give  $K^+/K^- = 1.13$  [35]. This combined with knowledge of the  $\bar{\Lambda}/\Lambda$  ratio offers a prediction of the  $\bar{\Xi}^+/\Xi^-$  ratio via Equation 6.3.

$$\frac{\bar{\Xi}^+(\bar{d}s\bar{s})}{\Xi^-(dss)} = \frac{K^+(u\bar{s})}{K^-(\bar{u}s)} \times \frac{\bar{\Lambda}(\bar{u}\bar{d}\bar{s})}{\Lambda(uds)} \quad (6.3)$$

STAR has measured  $\bar{\Lambda}/\Lambda = 0.736 \pm 0.008$  [56], which combines with the model prediction of the charged kaon ratio to give  $\bar{\Xi}^+/\Xi^- \simeq 0.83$ . This predicted value is close to the measured ratio from this analysis. It is important to note that this model does not assume an equilibrated system. It also does not assume how the quark matter prior to hadronization is formed, i.e., it does not assume the presence of a quark-gluon plasma.

Contrary to the quark coalescence model, a statistical thermal model approach assumes that an equilibrated system has formed [39]. In the framework of this model, the particle ratios only depend on the temperature,  $T$ , and the baryo-chemical potential,  $\mu_B$ . The multiplicative factor from the quark coalescence model can then be calculated by the quark fugacities as in Equation 6.4.

$$D = \frac{u\bar{s}}{\bar{u}s} = \frac{\lambda_u \times 1/\lambda_s}{1/\lambda_u \times \lambda_s} = \lambda_u^2 \times \lambda_s^{-2} = e^{(2\mu_B - 6\mu_s)/3T} \quad (6.4)$$

Under the assumption of local strangeness conservation where one can allow  $\mu_s = 0$ ,  $D$  can be calculated using the previously stated values of  $\mu_B$  and  $T_{ch}$  [39]. This results in  $D \simeq 1.19$ , which in turn predicts a ratio  $\bar{\Xi}^+/\Xi^- \simeq 0.88$ .

The measured ratios are reasonably predicted by both the quark coalescence model and the statistical thermal model and so cannot be used to

distinguish between the two particle production mechanisms.

### 6.2.2 Corrected Spectra

While using anti-baryon to baryon ratios is relatively simple because of the symmetry involved in the STAR experiment, the previous section shows that these ratios lack the necessary resolution to make a statement as to which model is correct. Further insight into the question of strangeness production can be gathered from unlike particle ratios, such as  $\bar{\Xi}^+/\bar{\Lambda}$  or  $\bar{\Xi}^+/\pi^+$ . There are predictions for unlike particle ratios in both the quark coalescence model and the statistical thermal model, meaning these ratios may lend more discriminating power to determining which is correct, or alternatively, which is wrong. Examining unlike particle ratios implies corrected spectra must be used for a meaningful comparison, since particles of greatly different masses or chemical compositions would not necessarily have similar production properties.

Going from  $Pb + Pb$  reactions at the SPS to  $Au + Au$  reactions at RHIC involves an order of magnitude more energy at the center of mass. It is expected that more violent collisions are more likely to exhibit new particle production mechanisms, which might be made apparent from the evolution of the production rates of particles with the energy of the collision. The production rate per unit rapidity is augmented by roughly 30% for  $\Xi^-$  and by more than a factor of 5 for  $\bar{\Xi}^+$  when compared with NA49 results from the SPS [13].

Figure 6.7 shows the ratios of  $\Xi^-$  and  $\bar{\Xi}^+$  to the negative hadrons and to

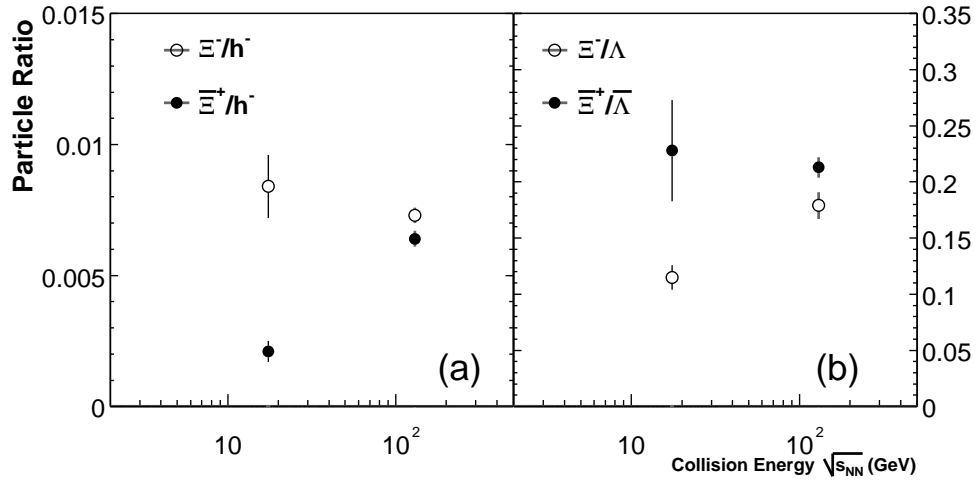


Figure 6.7: Non-identical particle ratios as a function of collision energy. Data points are from WA97 [22] ( $\sqrt{s_{NN}} = 17.3$  GeV), other STAR [3, 56] analyses, and this analysis. Feed-down contributions from  $\Xi^-$  and  $\Xi^+$  have been corrected for in the  $\Lambda$  and  $\bar{\Lambda}$  yields.

$\Lambda$  and  $\bar{\Lambda}$  for both the SPS [22] and RHIC [3, 56] energies. The data presented are from the 10% most central events. Corrections for feed-down of heavier baryons has been applied to the  $\Lambda$  and  $\bar{\Lambda}$  results. The WA97 collaboration estimated feed-down corrections of 5% and 10% for  $\Lambda$  and  $\bar{\Lambda}$ , respectively [23]. Feed-down for STAR data is approximately  $27 \pm 6\%$  [5] for  $\Lambda$  and  $\bar{\Lambda}$ . Statistical errors are presented in the figure. The  $\Xi^+/h^-$  ratio increases from the SPS to RHIC collisions due to more energy being available for multi-strange baryon production. However, this enhancement in the production of multi-strange baryons is almost exactly balanced by the drop in the net baryon content in the case of the essentially constant  $\Xi^-/h^-$  ratio. It is also observed that the  $\Xi^+/\bar{\Lambda}$  ratio at RHIC equals that of the SPS, which indicates strangeness production per particle has apparently already reached saturation at the lower

energy.

The  $\bar{\Xi}^+/\bar{\Lambda}$  ( $\bar{s}/\bar{u}$ ) ratio can be seen as an approximation of the Wroblewski factor, defined by [72]

$$\lambda \equiv \frac{2\langle s\bar{s} \rangle}{\langle u\bar{u} \rangle + \langle d\bar{d} \rangle} \quad (6.5)$$

where the averages refer to the number of  $q\bar{q}$  pairs produced by the system. The ratio is thus a measurement of the relative strangeness production rate. Within a thermal model framework [40], the Wroblewski factor is expected to decrease to a certain limit when going from the SPS energy to that of RHIC. This is interpreted as a result of the coupling between the decreasing net baryon density and the relatively minor increase in the freeze-out temperature when going to the higher collision energy.

The  $\Xi^-/\pi^-$  and  $\bar{\Xi}^+/\pi^+$  ratios are also examined as indicators of relative strangeness production so that a better comparison to models may be achieved.

The thermal analysis of the RHIC results done by Braun-Munzinger predicts various non-identical particle ratios, including  $\bar{\Xi}^+/\pi^+$ . For  $Au + Au$  collisions at  $\sqrt{s_{NN}} = 130$  GeV,  $\bar{\Xi}^+/\pi^+ = 6.51 \times 10^{-3}$  is expected when the model parameters are fixed to be  $T = 174$  MeV and  $\mu_B = 46$  MeV [39]. Knowledge of the production rate of  $\pi^-$  particles at mid-rapidity at STAR [46] combined with the one-to-one ratio of charged pions found at RHIC [29, 52] leads to a result for this analysis of  $\bar{\Xi}^+/\pi^+ = (6.63 \pm 0.31) \times 10^{-3}$  in the 10% most central events.

The quark coalescence model of [35] predicts a ratio of  $\Xi^-/\pi^- = 0.015$ . This compares to a ratio of  $\Xi^-/\pi^- = (7.59 \pm 0.35) \times 10^{-3}$  found from this analysis. The coalescence model overestimates the  $\Xi^-/\pi^-$  ratio by nearly a factor of 2. However, including an  $\sim 20\%$  systematic error to the ratio means that the model prediction is within  $2\sigma$  of the measurement.

Fits to the preliminary RHIC data are performed by Rafelski and Letessier in [63] where chemical equilibrium is not imposed. This is contrary to the thermal model treatment of [39]. The authors of [63] actually perform three fits of the data with different conditions. They look at complete chemical nonequilibrium, nonequilibrium except for strangeness conservation, or total equilibrium, the latter case being the same as the previously mentioned thermal model. Based on preliminary RHIC results, the removal of the constraint of chemical equilibrium is necessary to find agreement between the model calculations and the data. The non-equilibrium fit gives  $\Xi^-/\Lambda = 0.176$  and  $\bar{\Xi}^+/\bar{\Lambda} = 0.200$ . These numbers are similar to the measured values of  $\Xi^-/\Lambda = 0.179 \pm 0.012$  and  $\bar{\Xi}^+/\bar{\Lambda} = 0.213 \pm 0.009$  from this analysis. The model fit produces a chemical freeze-out temperature of  $T = 158$ , which is compatible with the scenario of sudden hadronization of the rapidly expanding fireball.

Table 6.3 lists the results from this analysis as well as a selection of the model predictions discussed above. This is illustrated in Figure 6.8. Also included are the predictions from the Dual Parton Model (DPM) [42], whose results are examined below. The  $\Xi^-/\Lambda$  ratios in Figure 6.8 are corrected for

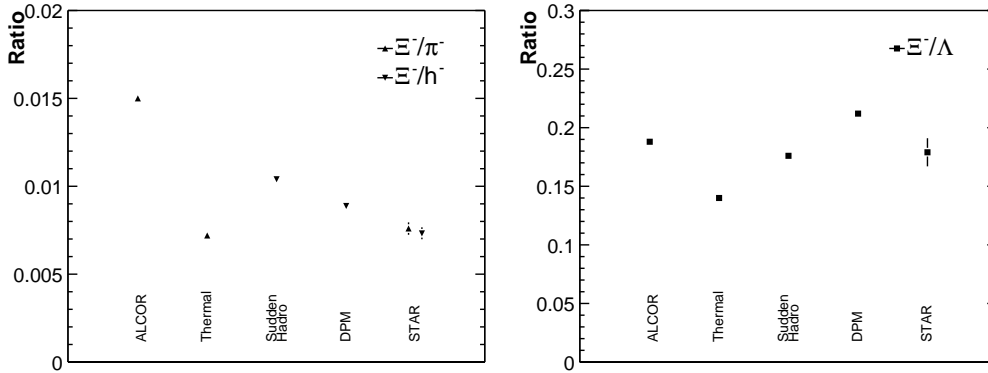


Figure 6.8: Measured non-identical particle ratios for  $\Xi^-/h^-$ ,  $\Xi^-/\pi^-$ , and  $\Xi^-/\Lambda$  compared to predictions from the quark coalescence model (ALCOR) [35], the statistical thermal model [39], the sudden hadronization model [63], and a purely hadronic model (DPM) [42].

feed-down from the weak decays of heavier baryons. Some models include feed-down from heavier baryons in their reported ratios, meaning a recalculation is necessary for a proper comparison to the measured results. This is taken into account for the figure, while the originally reported ratios are listed in the table.

| Ratios: Measured and Predicted |                      |                 |                     |                       |             |
|--------------------------------|----------------------|-----------------|---------------------|-----------------------|-------------|
| Ratio                          | Measured             | Thermal<br>[39] | Coalescence<br>[35] | Sudden<br>Hadro. [63] | DPM<br>[42] |
| $\Xi^-/h^-$                    | $0.00732 \pm 0.0034$ |                 |                     | 0.00104               | 0.0089      |
| $\Xi^-/\pi^-$                  | $0.00759 \pm 0.0035$ | 0.0072          | 0.015               |                       |             |
| $\Xi^+/\pi^+$                  | $0.00663 \pm 0.0031$ | 0.00651         |                     |                       |             |
| $\Xi^-/\Lambda$                | $0.179 \pm 0.012$    | 0.123           | 0.188               | 0.176                 | 0.154       |
| $\Xi^+/\Lambda$                | $0.213 \pm 0.009$    | 0.145           |                     | 0.200                 |             |

Table 6.3: A selection of non-identical particle ratios from model predictions and experimental results. Measured values are from the 10% most central events.

### 6.2.3 Centrality Dependence of $\Xi^-$ and $\bar{\Xi}^+$ Production

The results of the preceding section only dealt with the 10% most central events from this analysis. However, it is important to also examine the dependence of the results on the centrality of the collision, since any abrupt changes in the distribution might be an indication that the production mechanisms for  $\Xi^-$  and  $\bar{\Xi}^+$  particles change to something new.

Figure 6.9 shows the rapidity densities of  $\Xi^-$  and  $\bar{\Xi}^+$  as a function of the pseudo-rapidity density of negative hadrons. The trend supports a linear evolution of  $dN/dy$  with  $dN/dh^-$  as is evidenced by the lines, which represent linear fits to the data. The results of the linear fits are given by Equations 6.6 and 6.7.

$$dN_{\Xi^-}/dy = 0.0076 \pm 0.0004 \times dN_{h^-}/d\eta - 0.083 \pm 0.045 \quad (6.6)$$

$$dN_{\bar{\Xi}^+}/dy = 0.0065 \pm 0.0004 \times dN_{h^-}/d\eta - 0.079 \pm 0.041 \quad (6.7)$$

Also shown is the result of the Dual Parton Model predictions [42]. This model describes hadron interactions through the formation of intermediate states, or resonances. The model takes into account final state interactions,

$$\pi + N \rightleftharpoons K + \Lambda, \quad \pi + \Lambda \rightleftharpoons K + \Xi, \quad \pi + \Xi \rightleftharpoons K + \Omega, \quad (6.8)$$

where the densities of particles to the left of the arrows are greater than the densities of particles on the right. This leads to a gain of strange particle yields when these final state interactions are taken into account by the model. Also, since the net baryon density is greater than zero, the gain in the yield



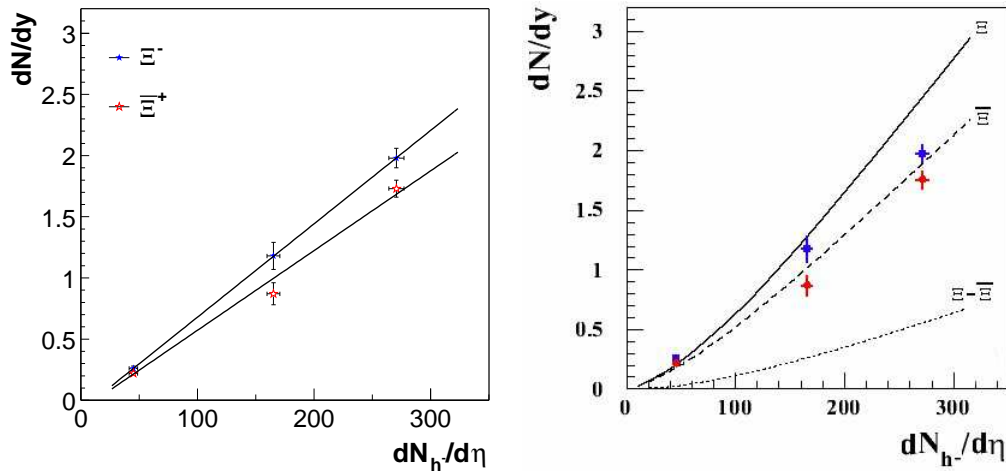


Figure 6.9:  $dN/dy$  vs.  $dN_{h^-}/d\eta$  for the centrality classes of this analysis. The left figure shows the data with linear fits while the right figure shows the data with the Dual Parton Model predictions (curves) [42].

of strange baryons is expected to be larger for baryons than for anti-baryons. The concave shape of the curves is distinctive of the Dual Parton Model.

While the measured rapidity densities do not appear to match the predicted values from the Dual Parton Model, the inclusion of systematic errors would make the disagreement less certain. A more detailed centrality scan of  $\Xi^-$  and  $\Xi^+$  production characteristics is necessary before the precision of the data will be sufficient to remark on the model one way or the other.

#### 6.2.4 Collective Behavior

Assuming a thermal source from which the particles are produced, the transverse mass spectra can be fit with a function of the form given by Equation 6.1. The measured inverse slope parameter of  $\Xi^-$  ( $\Xi^+$ ) particles is actually

composed of the particles' thermal freeze-out temperature and a component describing collective behavior, namely transverse flow, which is proportional to the particle mass, as was shown in Equation 2.13.

The inverse slope parameters for  $\Xi^-$  and  $\Xi^+$  are plotted as functions of event centrality in Figure 6.10 with statistical error bars. Within each centrality bin,  $\Xi^-$  and  $\Xi^+$  appear to have similar inverse slopes. On the other hand, there appears to be a dependence with centrality, especially in the case of  $\Xi^-$ . However, it is difficult to state that a trend really exists due to the overlap of the errors. Folding in systematic errors would make the overlap more obvious and so make any observed trend less tenable.

While the measured temperatures do in fact increase with more central events for  $\Lambda$  [56] and for  $\bar{p}$  [4], as measured by the STAR collaboration, much greater statistics than was taken in the year 2000 physics run is necessary to make a claim concerning the dependence of the inverse slope with centrality for  $\Xi^-$  ( $\Xi^+$ ). If the parameter is indeed constant, then this might indicate that neither the freeze-out temperature nor the transverse flow changes significantly over the range of examined centralities for multi-strange baryons.

The inverse slope parameters are plotted in Figure 6.11 for particles measured by STAR [5–8, 46, 51] as a function of mass. Also shown are values from SPS experiments at  $\sqrt{s_{NN}} = 17.3$  GeV [12, 24, 31]. The trend appears to be the same at the two energies, with STAR values being systematically higher. Also of interest is that the inverse slopes of the lower mass particles appear to follow a linear relationship with mass. This is indicative of strong, collective

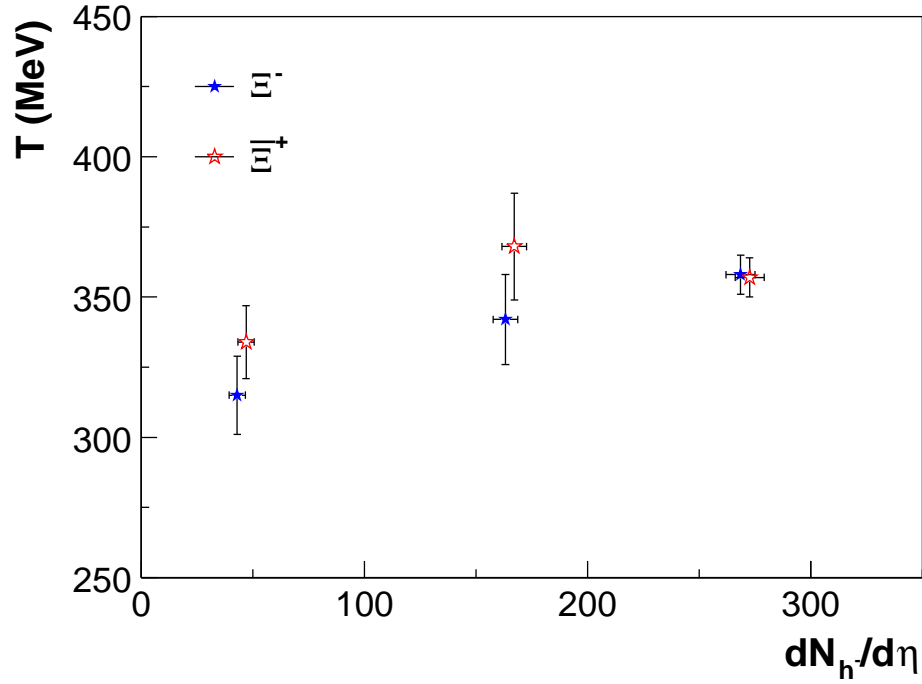


Figure 6.10:  $T$  vs.  $dN_{h-}/d\eta$  for the centrality classes of this analysis. Statistical errors are shown.

transverse flow [31, 73]. However, the higher mass strange particles, particularly the multi-strange baryons which interact weakly with the surrounding particle bath, show significant departure from the linear trend. The implication is that multi-strange baryons decouple from the system earlier than lighter particles [68, 73]. This discredits the idea of simultaneous hadronization of the various particle species at a single thermal freeze-out temperature. Furthermore, the flatness of multi-strange baryon inverse slopes as a function of mass might indicate that transverse flow develops at a later stage of the collision.

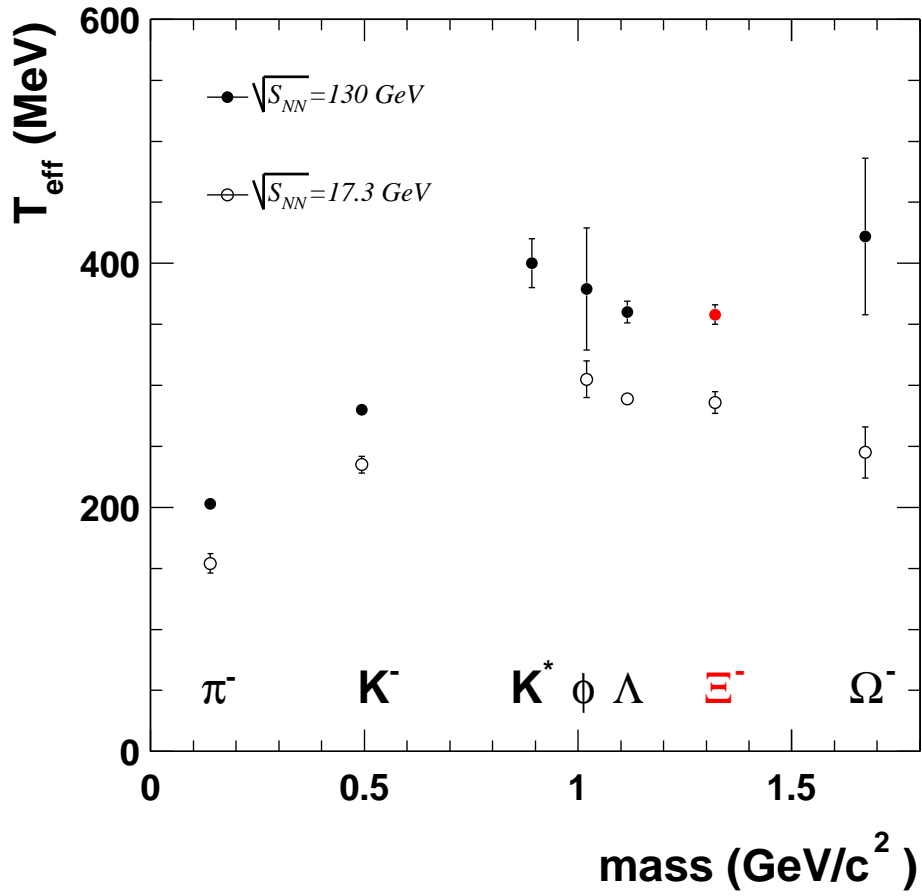


Figure 6.11: Inverse slope parameters as a function of mass at both the SPS and RHIC energies. Statistical errors are shown.

# Chapter 7

## Conclusion

The production properties of  $\Xi^-$  and  $\bar{\Xi}^+$  particles have been investigated through particle ratios and yields measured by the STAR detector from RHIC  $Au + Au$  collisions at  $\sqrt{s_{NN}} = 130$  GeV. The  $\bar{\Xi}^+/\Xi^-$  ratio is enhanced over the previous  $\sqrt{s_{NN}} = 17.3$  GeV  $Pb + Pb$  SPS results, indicating the approach to zero net baryon density at mid-rapidity for higher energy collisions. Fits to the data using thermal equilibrium models [39, 48] are able to determine a chemical freeze-out temperature,  $T_{ch} \sim 174$  MeV, and a baryon chemical potential,  $\mu_B \sim 46$  MeV for RHIC collisions. The temperature is reasonably close to the theoretical critical transition temperature between the QGP and the hadronic gas phases. This is suggestive of a deconfined medium being produced in RHIC collisions.

While  $\bar{B}/B$  measurements are certainly useful, they alone are unable to determine which particle production models are correct, or alternatively, fail to reproduce the data. Measurements of  $\Xi^-/h^-$ ,  $\Xi^-/\pi^-$ ,  $\Xi^-/\Lambda$  have been performed, along with their anti-particle counterparts, to facilitate further the comparison to models as well as to previous SPS results.

Figures 6.8 and 6.9 lead to various conclusions regarding model predic-

tions. While the quark coalescence model of [35] appears to be in agreement with  $\bar{B}/B$  results from STAR, it does not seem to agree as well when examining  $\Xi^-/\pi^-$ . The equilibrium statistical thermal model of [39] shows agreement with  $\bar{\Xi}^+/\pi^+$ , but not as good agreement with  $\Xi^-/\Lambda$ . On the other hand, the nonequilibrium thermal model of [63] apparently agrees with the measured  $\Xi^-/\Lambda$ . The measured  $\Xi^-$  and  $\bar{\Xi}^+$  yields as functions of  $dN_{h^-}/d\eta$  support linear trends; however, the measurements do not necessarily rule out the Dual Parton Model predicted values of [42] when the systematic error of  $\sim 20\%$  is included. Clearly, more studies are needed to determine the accuracy of these statements.

Comparison to previous SPS results allows for some qualitative remarks to be made about RHIC collisions. The evolution of  $\Xi^-/h^-$  and  $\bar{\Xi}^+/h^-$  from the SPS to RHIC (Figure 6.7) is the result of two mechanisms: the increase in strangeness production due to there being more available energy at RHIC, observed through the  $\bar{\Xi}^+/h^-$  trend, and its balance with the reduction in net baryon content, seen via  $\Xi^-/h^-$ . It is also observed that the  $\bar{\Xi}^+/\bar{\Lambda}$  ratio remains the same at RHIC and the SPS, indicating that strangeness production per particle is apparently already saturated at the lower energy.

The inverse slope parameters for particles measured at the SPS and at RHIC show similar behavior when plotted as a function of particle mass. The RHIC inverse slopes are consistently higher than those found at the SPS though, which could indicate that transverse flow is stronger at the higher energy assuming a constant freeze-out temperature, as indicated by thermal

analyses [38, 39]. However, for the heavier strange baryons a clear deviation is seen. This deviation is contrary to a picture of simultaneous freeze-out of all the particles. Instead this points to strange, and especially multi-strange, baryons freezing out earlier than the lighter quark particles. The flatness of the multi-strange baryon inverse slope parameters might indicate that transverse flow develops at a time after freeze-out.

The main limitation of the results presented in this document is the lack of statistics. This hopefully will not be the case for future analyses after more collisions are produced by RHIC. Since the summer of 2000 physics run, RHIC has collided  $Au$  ions at the top design energy of  $\sqrt{s_{NN}} = 200$  GeV. In the year 2001, STAR recorded approximately 4 million central event and 5 million minimum bias events. STAR also added more detectors, such as the Silicon Vertex Tracker (SVT) closer to the interaction region, as well as the Forward TPCs in the higher rapidity areas, seen in Figure 3.5. These and other installed or planned detectors will aid in reconstructing a more complete picture of particle production under extreme conditions.

With additional detectors and much greater statistics, measurements of exotic charmed particles such as the  $D$  and  $J/\Psi$  mesons can be obtained. Furthermore, more precise measurements of the production rates for multi-strange baryons will be possible. For example, correlations between  $\Xi^-$  and other particles may offer insight into the source of  $\Xi^-$  emission. Also, the search for previously unseen, exotic particles such as dibaryons may also be continued with the availability of more events at such high collision energies.

In the future, the Large Hadron Collider (LHC) will provide heavy ion collisions at  $\sqrt{s_{\text{NN}}} \sim 6$  TeV, more than an order of magnitude greater than the energy achievable at RHIC [60]. Such high energies might allow for the deconfined fireball to last for a longer time and with higher initial temperatures. The thermal production of  $c\bar{c}$  quarks might be possible then, analogous to the thermal production of  $s\bar{s}$  at the lower RHIC energies. A great amount of effort is still needed to explain the question of what happens when matter is introduced to extreme conditions of temperature and pressure, but piece by piece, it is being answered.



## Appendix

# Appendix 1

## Observables and Spectra

Typically, the momentum for any particle can be resolved into transverse ( $p_T$ ) and longitudinal ( $p_L$ ) components. In many cases, the mass ( $m$ ) of the particle can also be determined. The longitudinal momentum can be conveniently expressed in terms of the rapidity variable ( $y$ )

$$y \equiv \frac{1}{2} \ln \frac{E + p_L}{E - p_L} = \ln \frac{E + p_L}{m_T} \quad (1.1)$$

$$\cosh y = \frac{E}{m_T}, \quad \sinh y = \frac{p_L}{m_T} \quad (1.2)$$

where

$$m_T = \sqrt{m^2 + p_T^2} \quad \text{and} \quad E = \sqrt{p_L^2 + m_T^2}. \quad (1.3)$$

In the limit  $m \ll E$ , the rapidity reduces to the pseudorapidity ( $\eta$ )

$$\eta = -\ln \tan \frac{\theta}{2} \quad (1.4)$$

$$\cosh \eta = \csc \theta, \quad \sinh \eta = \cot \theta \quad (1.5)$$

where  $\theta$  is the polar angle of emission relative to the beam direction.

The rapidity variable transforms linearly under a Lorentz transformation so that the invariant differential single particle inclusive cross section

becomes

$$E \frac{d^3\sigma}{dp^3} = E \frac{d^2\sigma}{2\pi p_T dp_T dp_L} = \text{const.} \frac{1}{2\pi p_T} \frac{d^2N}{p_T dp_T dy} \quad (1.6)$$

where  $dy = dp_L/E$ . Using a thermal  $p_T$  distribution, it has been shown [50] that

$$\frac{1}{2\pi p_T} \frac{d^2N}{dp_T dy} = \text{const.} m_T \sum_{n=1}^{\infty} (\mp)^{n+1} K_1\left(n \frac{m_T}{T}\right) \quad (1.7)$$

where  $K_1$  is a modified Bessel function,  $T$  is the temperature of a particle type, and  $m_T$  is the transverse mass. A frequently used approximation is

$$\frac{1}{2\pi p_T} \frac{d^2N}{dp_T dy} = \frac{1}{2\pi m_T} \frac{d^2N}{dm_T dy} = A e^{-m_T/T} \quad (1.8)$$

where  $p_T dp_T = m_T dm_T$  and  $A$  is some constant. Integration over  $m_T$  determines the constant factor  $A$  exactly in terms of  $dN/dy$ , extrapolated over all values of  $m_T$ , such that

$$\frac{1}{2\pi m_T} \frac{d^2N}{dm_T dy} = \frac{dN/dy}{2\pi T(m_0 + T)} e^{-(m_T - m_0)/T} \quad (1.9)$$

where  $m_0$  is the rest mass of the particle. This form of the multiplicity distribution allows the determination of both the yield and the inverse slope parameter for a particle type by fitting with just this one function. Since the data are plotted versus  $(m_T - m_0)$  instead of  $m_T$ , which doesn't affect the shape of the spectra, particles of different masses can be examined on the same histogram using a single horizontal scale. Thus, differences in slope parameters between particle types can be quickly examined visually.

## Bibliography

- [1] T. Abbott et al. *Phys. Rev. Lett.*, 64:847, 1990.
- [2] K.H. Ackermann et al. *Nucl. Phys.*, A661:681c, 1999.
- [3] C. Adler et al. *Phys. Rev. Lett.*, 87:112303, 2001.
- [4] C. Adler et al. *Phys. Rev. Lett.*, 87:262302, 2001.
- [5] C. Adler et al. *Phys. Rev. Lett.*, 89:092301, 2002.
- [6] C. Adler et al. *Phys. Rev.*, C65:041901, 2002.
- [7] C. Adler et al.  $K^*(892)^0$  Production in Relativistic Heavy Ion Collisions at  $\sqrt{s_{NN}} = 130$  GeV. *nucl-ex/0205015*, 2002.
- [8] C. Adler et al. Kaon Production and Kaon to Pion Ratio in Au+Au Collisions at  $\sqrt{s_{NN}} = 130$  GeV. *nucl-ex/0206008*, 2002.
- [9] C. Adler et al. Multi-Strange Baryon Production in Au+Au Collisions at  $\sqrt{s_{NN}} = 130$  GeV. to be submitted to *Phys. Rev. Lett.*, 2002.
- [10] C. Adler et al. Strange Anti-particle to Particle Ratios at Mid-Rapidity in  $\sqrt{s_{NN}} = 130$  GeV Au+Au Collisions. to be submitted to *Phys. Rev. Lett.*, 2002.

- [11] C. Adler et al. The STAR Level-3 Trigger System. Preprint submitted to Elsevier Science, March 2002.
- [12] S.V. Afanasiev et al. *Phys. Lett.*, B491:59, 2000.
- [13] S.V. Afanasiev et al. *Phys. Lett.*, B538:275, 2002.
- [14] L. Ahle et al. *Phys. Rev.*, C58:3523, 1998.
- [15] L. Ahle et al. *Phys. Rev.*, C60:044904, 1999.
- [16] S. Ahmad et al. *Phys. Lett.*, B382:35, 1996.
- [17] T. Alber et al. *Z. Phys.*, C64:195, 1994.
- [18] E. Andersen et al. *Phys. Lett.*, B449:401, 1999.
- [19] F. Antinori et al. *Phys. Lett.*, B447:178, 1999.
- [20] F. Antinori et al. *Nucl. Phys.*, A661:357c, 1999.
- [21] F. Antinori et al. *J. Phys.*, G25:171, 1999.
- [22] F. Antinori et al. *Nucl. Phys.*, A661:130c, 1999.
- [23] F. Antinori et al. *Eur. Phys. J.*, C14:633, 2000.
- [24] F. Antinori et al. *J. Phys.*, G27:375, 2001.
- [25] F. Antinori et al. Results on  $\Lambda$  and  $\Xi$  production in Pb-Pb collisions at 160 GeV/c per nucleon from the NA57 experiment. *hep-ex/0207047*, 2002.

- [26] H. Appelshäuser et al. *Phys. Lett.*, B444:523, 1998.
- [27] J. Ashman et al. *Phys. Lett.*, B206:364, 1988.
- [28] I. Schmidt B.-Q. Ma and J.-J. Yang. *Eur. Phys. J.*, A12:353, 2001.
- [29] B. B. Back et al. *Phys. Rev. Lett.*, 87:102301, 2001.
- [30] I.G. Bearden et al. *Nucl. Phys.*, A610:175, 1996.
- [31] I.G. Bearden et al. *Phys. Rev. Lett.*, 78:2080, 1997.
- [32] I.G. Bearden et al. *Phys. Rev. Lett.*, 87:112305, 2001.
- [33] A. Bialas. *Phys. Lett.*, B442:449, 1998.
- [34] F.S. Bieser et al. The STAR Trigger. Preprint submitted to Elsevier Science, April 2002.
- [35] T.S. Biró et al. *J. Phys.*, G28:1561, 2002.
- [36] W. Blum and L. Rolandi. *Particle Detection With Drift Chambers*. Springer, 2nd edition, 1994.
- [37] C. Bormann et al. *J. Phys.*, G23:1817, 1997.
- [38] P. Braun-Munzinger et al. *Phys. Lett.*, B465:15, 1999.
- [39] P. Braun-Munzinger et al. *Phys. Lett.*, B518:41, 2001.
- [40] P. Braun-Munzinger et al. *Nucl. Phys.*, A697:902, 2002.

- [41] R. Brun et al. GEANT user guide. CERN Report DD/EE/84-1, 1987.
- [42] A. Capella et al. Strange particle production at RHIC in the Dual Parton Model. *nucl-th/0205014*, 2002.
- [43] I. Chemakin et al. Semi-Inclusive  $\Lambda$  and  $K_S$  Production in p-Au Collisions at 17.5 GeV/c. *nucl-ex/0003010*, 2000.
- [44] The STAR Collaboration. Conceptual Design Report for the Solenoidal Tracker at RHIC. Technical Report PUB-5347, LBL, June 1992.
- [45] L.P. Csernai. *Introduction to Relativistic Heavy Ion Collisions*. John Wiley & Sons, 1994.
- [46] M. C. de la Barca Sánchez. *Charged Hadron Spectra in Au+Au Collisions at  $\sqrt{s_{NN}} = 130$  GeV*. PhD thesis, Yale University, 2001.
- [47] E. Fermi. *Phys. Rev.*, 57, 1940.
- [48] W. Florkowski et al. Thermal Analysis of Particle Ratios and  $p_{\perp}$  Spectra at RHIC. *nucl-th/0106009*, 2001.
- [49] D.E. Groom et al., editors. *Review of Particle Physics*, volume C15 of *The European Physical Journal*. Springer, 2000.
- [50] R. Hagedorn. *Riv. Nuovo Cimento*, 6(10), 1983.
- [51] B. Hippolyte. *Etude de la production d'étrangeté dans les collisions d'ions lourds ultra-relativistes à  $\sqrt{s_{NN}} = 130$  GeV de l'expérience STAR au RHIC*. PhD thesis, Université Louis Pasteur de Strasbourg, 2002.

- [52] M. Horsley. *A Measurement of Charged Particle Ratios at High Transverse Momentum in an Ultra-Relativistic Heavy Ion Collision*. PhD thesis, Yale University, 2002.
- [53] F. Karsch. *Nucl. Phys.*, A698:199, 2002.
- [54] S.R. Klein et al. *IEEE Trans. on Nucl. Sci.*, 43:1768, 1996.
- [55] P. Koch, B. Müller, and J. Rafelski. *Phys. Rep.*, 142:167, 1986.
- [56] M. Lamont. *Neutral Strange Particle Production in Ultra-Relativistic Heavy Ion Collisions at  $\sqrt{s_{NN}}=130$  GeV*. PhD thesis, University of Birmingham, 2002.
- [57] B. Lasiuk. Particle Identification at STAR. STAR Note 312, 1997.
- [58] H. Long. *Mid-rapidity  $\Lambda$  and  $\bar{\Lambda}$  Production in Au+Au Collisions at the Relativistic Heavy Ion Collider*. PhD thesis, University of California, Los Angeles, 2002.
- [59] S. Margetis et al. *J. Phys.*, G25:189, 1999.
- [60] A. Morsch and H.H. Gutbrod for the ALICE Collaboration. *Prog. Part. Nucl. Phys.*, 42:345, 1999.
- [61] D.H. Perkins. *Introduction to High Energy Physics*. Addison Wesley, 3rd edition, 1987.
- [62] RHIC Project. *RHIC Design Manual*. BNL, <http://www.agsrhichome.bnl.gov/NT-share/rhicdm/>, October 2000.



- [63] J. Rafelski and J. Letessier. *Nucl. Phys.*, A702:304, 2002.
- [64] J. Rafelski and B. Müller. *Phys. Rev. Lett.*, 48(16):1066, 1982.
- [65] B. Stringfellow. *TPC Operations Manual*. [http://www.star.bnl.gov/STAR/html/tpc\\_1/oper/tpc\\_operation.html](http://www.star.bnl.gov/STAR/html/tpc_1/oper/tpc_operation.html), March 2000.
- [66] M. Tanaka. FEB/SBE: Commissioning with Au Beam and Run for the FY1996 AtR Transfer Line Commissioning. Technical Report 453, BNL, November 1997.
- [67] J. Thomas. *STAR TPC Drift-Defining Hardware: E-Fields and Gas*. [http://www.star.bnl.gov/STAR/html/tpc\\_1/hard/tpcrings/index.html](http://www.star.bnl.gov/STAR/html/tpc_1/hard/tpcrings/index.html), August 1999.
- [68] H. van Hecke et al. *Phys. Rev. Lett.*, 81:5764, 1998.
- [69] F. Wilczek. QCD In Extreme Conditions. *hep-ph/0003183*, 2000.
- [70] K.G. Wilson. *Phys. Rev.*, D10:2445, 1974.
- [71] C. Wong. *Introduction to High-Energy Heavy-Ion Collisions*. World Scientific, 1994.
- [72] A. Wroblewski. *Acta Phys. Pol.*, B16:379, 1985.
- [73] N. Xu. *J. Phys.*, G28:2121, 2002.
- [74] J. Zimányi et al. *Phys. Lett.*, B472:243, 2000.

# Vita

Curtis Patrick Leon Lansdell was born on October 7, 1974. Curtis attended the University of Texas at Austin from 1992 to 1996 and graduated with a B.S. in Physics. Curtis continued his studies in physics, enrolling in the Graduate School of the University of Texas at Austin in 1997.

Permanent address: PO Box 327  
Schertz, Texas 78154

This dissertation was typeset with L<sup>A</sup>T<sub>E</sub>X<sup>†</sup> by the author.

---

<sup>†</sup>L<sup>A</sup>T<sub>E</sub>X is a document preparation system developed by Leslie Lamport as a special version of Donald Knuth's T<sub>E</sub>X Program.